Boron in the Primary and Secondary Coordination Spheres of Iron and Nickel

by

Samantha Nicole MacMillan

A.B., Vassar College (2007)

Submitted to the Department of Chemistry
in partial fulfillment of the requirements for the degree of

Doctor of Philosophy

at the

MASSACHUSETTS INSTITUTE OF TECHNOLOGY

September 2013

Author .....
Department of Chemistry
July 2, 2013

Certified by ..
Jonas C. Peters
Bren Professor of Chemistry, California Institute of Technology
Thesis Supervisor

Accepted by .....
Robert W. Field
Haslam and Dewey Professor of Chemistry
Chairman, Departmental Committee on Graduate Studies

This doctoral thesis has been examined by a Committee of the Department of Chemistry as follows:

.....

Stephen J. Lippard
Arthur Amos Noyes Professor of Chemistry
Committee Chairman

.....

Jonas C. Peters
Bren Professor of Chemistry, California Institute of Technology
Thesis Supervisor

.....

Christopher C. Cummins
Professor of Chemistry
Department of Chemistry

One thing in my defense, not that it matters: I know something Carter never knew, or Helene, or maybe you. I know what "nothing" means, and keep on playing.

Why, BZ would say.

Why not, I say.

- Joan Didion, Play It As It Lays

For my parents, the most incredible people I know.

Acknowledgments

I have a confession: acknowledgments make me uncomfortable. I find being privy to the names, nicknames, inside jokes and other such features of the acknowledgments of people I know (and some I don't) to be oddly voyeuristic. Writing acknowledgments? Even worse. The number of people that make any student's time in graduate school more enjoyable is immense and in my case, having divided my time between MIT and Caltech, it is staggering. While I would love to mention everyone by name, I simply cannot and so I will say the following: I have had the pleasure of overlapping with very talented and intelligent students, staff and faculty at both institutions and have had, with very few exceptions, positive and rewarding experiences with them all. I have learned a lot from everyone I have interacted with and have always felt very fortunate to have such a large support group for both my professional and personal endeavors.

There are, of course, certain people that have had a profound impact and I would like to mention them individually. First, I would like to thank my thesis advisor, Prof. Jonas Peters. Jonas gave me a lot of freedom during my graduate career to pursue projects that I was truly interested in. While many of those projects did not result in publishable papers, I have learned a lot during my time in the group and appreciate his standing by me while I explored and eventually lit upon the science that constitutes the bulk of this thesis.

I would also like to thank my thesis committee, Prof. Steve Lippard and Prof. Kit Cummins, as well as Prof. Dick Schrock and Prof. Dan Nocera, for their insight and suggestions over the years. Kit has always treated me as one of his own students and I appreciate his honesty and generosity with his time for all things science. Kit and Dan's administrative assistant, Allison Kelsey, is phenomenal. She has been a fantastic friend over the years and always ensures that my visits to Boston are a blast.

In terms of instrumentation, I would like to thank David VanderVelde and Larry Henling from Caltech for their assistance with NMR and X-ray, respectively. Dave was instrumental in helping me assess the best experiments to describe the nickel systems featured in Chapter 3. A big, big thank you to Dr. Peter Müller at MIT for his guidance and support about X-ray crystallography; I am grateful that I was able to interact with and learn from the best in

the business.

One of my biggest support systems came in the form of my classmates in the Peters group: Daniel Suess, Ayumi Takaoka and Charlene Tsay. They have been great friends and fellow scientists and I am very excited to see what things are in store for them. Dan and I have been both desk and hood neighbors our entire time in graduate school; it has been fun and it has certainly been silly. The entire Peters lab has been a good group of people to work with. I am especially indebted to Hill Harman for being a great desk neighbor, music recommender and science collaborator. Many thanks to Joe Rheinhardt, who has become a very good friend and partner in crime. Thank you to Jeff Warren, Ian Tonks, Gretchen Keller and Oliver Shafaat for being a great group of friends and immediately taking me in after my arrival at Caltech.

At MIT, I was very close to a small group of people from the Cummins group: Glen Alliger, Chris Clough, Brandi Cossairt and Jared Silvia. They are an incredible mix of brains, wit and fun; I had not seen a group of such great thinkers, scientists and friends before and I am positive that I will be hard pressed to find another group like them. Glen was an enormous part of my life for a number of years and while circumstances forced us apart, I still consider him to be one of my best friends and wish him every happiness.

Outside of MIT and Caltech, there are a few very important people to thank. First, thank you to my undergrad advisor Prof. Joe Tanski, who initially sparked my interest in chemistry and who continued to be a fantastic mentor even after I left his group. Thank you to Prof. Rory Waterman for also being a great mentor and for involving me in some ridiculous hijinks. I also have to thank my future advisor, Prof. Kyle Lancaster, for taking a chance on me at the San Diego ACS and offering me a position in his labs at Cornell. An enormous thank you is in order to my best friend Matt Morse, who has never failed at making me laugh so hard that I cried and who has always taken time from his busy, real-person schedule to hang out. And finally, my biggest and most important thank you goes to my parents, Tom and Cindy MacMillan. Their unwavering support and love has kept me going, even through the toughest spots. I love them both very much and when I grow up, I want to be just like them.

Boron in the Primary and Secondary Coordination Spheres of Iron and Nickel

by

Samantha Nicole MacMillan

Submitted to the Department of Chemistry on July 2, 2013, in partial fulfillment of the requirements for the degree of Doctor of Philosophy

Abstract

Motivated by the reported electronic versatility of anionic tris(phosphine)borate and tris(phosphine)silyl ligands, a new, neutral tris(phosphine)borane scaffold was prepared. The synthesis, spectroscopy and solid-state structures of iron complexes ligated by both π-acidic and π-basic moieties are presented. The cationic imido complex, [[TPB^{Ph}]FeNAd][BAr^F_4] ([TPB^{Ph}] = $(2\text{-}Ph_2PC_6H_4)_3B$, [$BAr^F_4$] = tetrakis[3,5-bis(trifluoromethyl)phenyl]borate), was generated and the EPR spectroscopic and solid-state structural features described. This complex is unique among the iron tris(phosphine)borane complexes prepared by the Peters group in that there is no interaction between the iron and boron centers.

The potential for bifunctional catalysis employing the nickel bis(phosphine)borane complex [$^{Mes}DPB^{Ph}$]Ni was explored ([$^{Mes}DPB^{Ph}$] = $(2\text{-}Ph_2PC_6H_4)_2B(1,3,5\text{-}Me_3C_6H_2)$). This species activates E–H bonds (E = Si, Ge, S) and traditionally unstable borohydrido-E nickel complexes were isolated. The solid-state structures of these complexes are described. The catalytic hydrosilylation of *para*-substituted benzaldehydes was studied and a mechanism for the transformation proposed. An intermediate nickel borohydridosiloxyalkyl species was identified and characterized by NMR spectroscopy. A series of nickel borohydridothiolate complexes was prepared and a rare, nickel(I) borohydridothiolate species was isolated and structurally characterized.

The reactivity of the iron(II) alkyl complex [$PhBP^{Ph}_3$]FeMe towards H_2 is presented ([$PhBP^{Ph}_3$] = $PhB(CH_2PPh_2)^-_3$). Exposure of a C_6H_6 solution of [$PhBP^{Ph}_3$]FeMe to an excess of H_2 results in the formation of a previously described iron η^5-cyclohexadienyl complex. Repeating the reaction in THF solution with one equivalent of PMe_2Ph yields the dihydrogen hydride complex [$PhBP^{Ph}_3$]Fe(H_2)(H)(PMe_2Ph), as determined by ^1H and $^{31}P\{^1H\}$ NMR spectroscopies and a short T_1 spin-lattice relaxation measurement. This species is a slow but competent olefin hydrogenation catalyst. In an effort to access a more reactive precatalyst, the iron chemistry of the bis(phosphine)borate ligands [$Ph_2BP^{Ph}_2$] and [$Ph_2BP^{tBu}_2$] ([$Ph_2BP^R_2$] = $Ph_2B(CH_2PR_2)^-_2$, R = Ph and ^{t}Bu) was explored. Iron(II) halide, aryloxide, anilido and alkyl complexes were isolated and characterized.

Thesis Supervisor: Jonas C. Peters
Title: Bren Professor of Chemistry, California Institute of Technology

Contents

List of Figures

List of Schemes

List of Tables

List of Abbreviations

α	angle α
a	axis *a*
Å	angstrom
Ad	adamantyl
anal.	analysis (Anal. in combustion analysis presentations)
Ar	aryl
atm	atmosphere
ASN	5-azoniaspiro[4.4]nonane
β	angle β
b	axis *b*
Bn	benzyl
br	broad or broadened
Bu	butyl
C	Celcius
c	axis *c*
C	symmetry group
^{13}C	carbon nuclear magnetic resonance
ca.	circa, about
cal	calorie
calcd	calculated
CCD	charge-coupled device
cod	1,5-cyclooctadiene
Cp	cyclopentadienyl
Cp*	pentamethylcyclopentadienyl
δ	NMR chemical shift in parts per million
Δ	change
d	day, deuteron, doublet (spectra)

2D ..... two-dimensional
deg ..... degree (°)
DFT ..... density functional theory
ε ..... molar absorptivity
E ..... energy
E^o ..... standard electrode potential
$E_{1/2}$ ..... half-wave potential
e.g. ..... for example
ed. ..... edition, edited
Ed. ..... editor
Eds. ..... editors
ENDOR ..... electron-nuclear double resonance
EPR ..... electron paramagnetic resonance
equiv ..... equivalent
ESR ..... electron spin resonance
Et ..... ethyl
eu ..... entropy unit
EXSY ..... exchange spectroscopy
F ..... crystallographic structure factor
^{19}F ..... fluorine nuclear magnetic resonance
Fc ..... ferrocene
FLP ..... frustrated Lewis pair
fw ..... formula weight
γ ..... angle γ
g ..... gram
g ..... splitting factor (ESR and NMR spectroscopy)
G ..... gauss, giga (10^9)
GC ..... gas chromatography
GHz ..... gigahertz
GoF ..... goodness of fit
h ..... hour
h ..... crystallographic index (*hkl*)
H ..... enthalpy
^{1}H ..... proton nuclear magnetic resonance
hkl ..... crystallographic index
HOMO ..... highest occupied molecular orbital
HSQC ..... heteronuclear single quantum coherence spectroscopy
i.e ..... that is
i ..... iso (as in ^{i}Pr)
IR ..... infrared
J ..... coupling constant (NMR and ESR spectroscopy)

k ..... kilo (10^3)
k ..... crystallographic index (*hkl*), rate constant
K ..... kelvin
K ..... equilibrium constant
λ ..... wavelength
λ_{max} ..... wavelength of maximum absorption
l ..... crystallographic index (*hkl*)
L ..... ligand, liter
LAH ..... lithium aluminum hydride
LMCT ..... ligand-to-metal charge transfer
LUMO ..... lowest unoccupied molecular orbital
μ ..... micro (10^{-6})
μ_B ..... Bohr magneton
μ_{eff} ..... effective magnetic moment
m ..... meter, milli (10^{-3}), multiplet (spectra)
M ..... metal, molar (mol L^{-1}), mega (10^6)
Me ..... methyl
Mes ..... mesityl (2,4,6-trimethylphenyl)
MHz ..... megahertz
min ..... minute
MO ..... molecular orbital
mol ..... mole
mol % ..... mole percent
n ..... nano (10^{-9})
n ..... normal (as in ^{n}Bu)
naph ..... napthalenide
nm ..... nanometer
NMR ..... nuclear magnetic resonance
o ..... ortho
obsd ..... observed
OEC ..... oxygen evolving complex
% ..... percent
π ..... type of orbital, electron
p ..... para
^{31}P ..... phosphorus nuclear magnetic resonance
Ph ..... phenyl
ppm ..... parts per million
Pr ..... propyl
PSII ..... photosystem II
q ..... quartet (spectra)
R ..... generic organic group, residual value (crystallography)

ref ..... reference
σ ..... type of orbital, electron
Σ ..... summation
s ..... second, singlet (spectra)
S ..... entropy, electronic spin
^{29}Si ..... silicon nuclear magnetic resonance
SOF ..... site occupancy factor
SOMO ..... singly occupied molecular orbital
t ..... triplet
t ..... tertiary (as in ^{t}Bu), time
$t_{1/2}$ ..... half-life
T ..... tesla
T ..... temperature (in kelvins)
^{205}Tl ..... thallium nuclear magnetic resonance
THF ..... tetrahydrofuran
tol ..... tolyl (4-methylphenyl)
Ts ..... tosyl (4-toluenesulfonyl)
UV ..... ultraviolet
UV-vis ..... ultraviolet-visible
v ..... scan rate
V ..... unit cell volume, volt
vis ..... visible
vs ..... versus
wR ..... weighted R-factor
wt ..... weight
X ..... generic anionic ligand
XAS ..... X-ray absorption spectroscopy
Z ..... number of molecules in unit cell

1 Introduction

Contents

1.1 Motivation

A persistent challenge facing organometallic chemists is the development of new chemical transformations that employ abundant and inexpensive reagents (N_2, H_2, CO_2, CO, olefins, etc.) for the preparation of value-added chemical products.[1] One attractive approach to the functionalization of such small molecules is the activation of an E−H bond (E = main group element) by a transition-metal complex, followed by group transfer to the unsaturated substrate of interest. Based on an E−H addition process rather than substitution, these reactions provide an atom economic route for the construction of new σ-bonds, as demonstrated in Scheme 1.1. The development of catalytic methods that use E−H substrates to break and forge σ-bonds is therefore an important goal to address.

The reactivity patterns of organometallic complexes are intimately associated with the identities of the transition-metal centers and the number and type of ligands bound directly to the metal centers.[2,3] To illustrate these principles, two simplified mechanistic pathways for the metal-mediated addition of an E−H substrate to an olefin are outlined

Preparation by substitution:

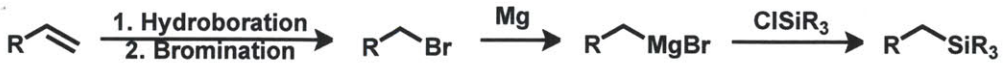

Preparation by E–H bond addition:

Scheme 1.1 Organosilanes prepared by (*top*) nucleophilic displacement of halogen from a halosilane by the appropriate organometallic reagent (i.e., substitution) and (*bottom*) addition of silane to the alkene double bond (i.e., hydrosilylation).

in Scheme 1.2. For an electron-rich transition-metal complex, the catalytic cycle often involves oxidative addition of the E−H bond, coordination of the olefin, insertion into either the M−E or M−H bond, and reductive elimination of the product molecule (Scheme 1.2, left).[4,5] In such a cycle, both the oxidation state and the coordination number of the metal center are increased by two upon oxidative addition of the E−H bond. This step is typically promoted by coordinatively unsaturated complexes ligated by strong σ-donors, such as alkylphosphine and N-heterocyclic carbene (NHC) ligands. Rational modification of the steric profile of these ancillary ligands can help facilitate reductive elimination of the product and regeneration of the starting metal complex.[6,7] For an electrophilic metal center, the catalytic cycle may consist of olefin coordination, nucleophilic attack by the E−H substrate and then protonolysis to release the product molecule (Scheme 1.2, right).[8,9] For this pathway, a more Lewis acidic metal center will render the coordinated olefin more electrophilic and thereby more susceptible to nucleophilic attack by the E−H substrate. Both mechanistic pathways can be significantly impacted by changes in the surrounding ligands; thus, the development of new ligand scaffolds that are able to fine tune the steric and electronic properties of an organometallic complex, particularly with respect to promoting novel reactivity, constitutes a large and ongoing area of research in the inorganic community.

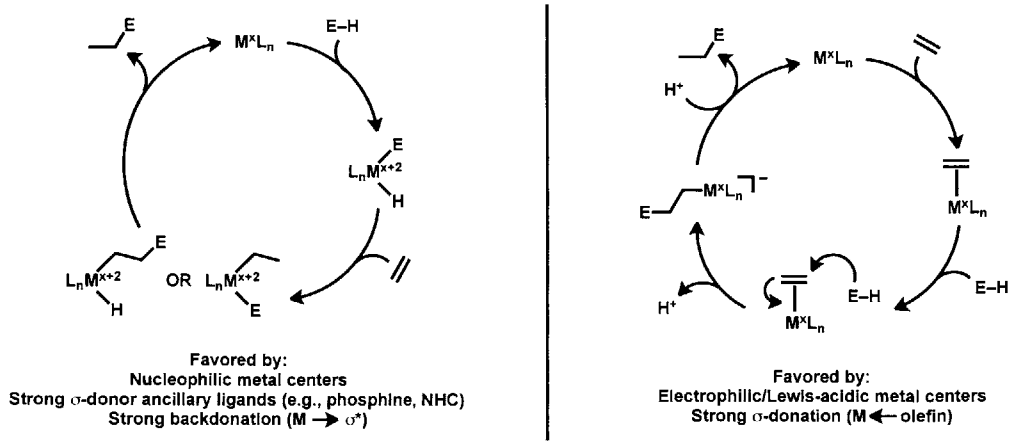

Scheme 1.2 Simplified mechanisms for the addition of an E–H substrate to an olefin. Electron-rich metal centers typically follow an oxidative addition pathway (*left*), while electrophilic metal centers promote nucleophilic attack of the olefin by the E–H substrate (*right*).

In addition to the parameters discussed above, the interaction of a metal center or incoming substrate with the secondary coordination sphere can also play a role in the reactivity of the complex. An elegant example of this concept is the work of Borovik in which both hydrogen-bond donor and acceptor ligand scaffolds have been explored to stabilize several unusual species (Figure 1.1). For example, a high-spin, trigonal bipyramidal iron(III) oxo complex has been isolated using the trianionic ligand $[H_3buea]^{3-}$ ($[H_3buea]^{3-}$ = tris[(N'-tertbutylureaylato)-N-ethyl]aminato, Figure 1.1, left).[10,11] The solid-state structure of this complex shows that the three urea NH groups are directed toward the oxo oxygen atom, suggesting the presence of intramolecular hydrogen bonding. The $O_{oxo}\cdots N_{urea}$ distances observed in the structure (2.69 – 2.73 Å), as well as solid-state IR spectroscopic measurements ($\nu_{(N-H)}$ = 3130 cm^{-1}) and DFT calculations, support the formulation of the species as an iron(III) oxo complex surrounded by a hydrogen bonding cavity. Employing the hydrogen-bond acceptor ligand $[MST]^{3-}$ ($[MST]^{3-}$ = N,N',N"-[2,2',2"-nitrilotris(ethane-2,1-diyl)]tris-(2,4,6-trimethylbenzenesulfonamido)), a cobalt(II)–(μ-OH_2)–calcium(II) bimetallic complex can be generated (Figure 1.1, right).[12] In this complex, the aquo ligand forms two intramolecular hydrogen bonds to two of the three sulfonamido groups of $[MST]^{3-}$, as determined by X-ray crystallographic analysis.

Chapter 5 describes the iron chemistry of tris(phosphine)borate and bis(phosphine)bor-

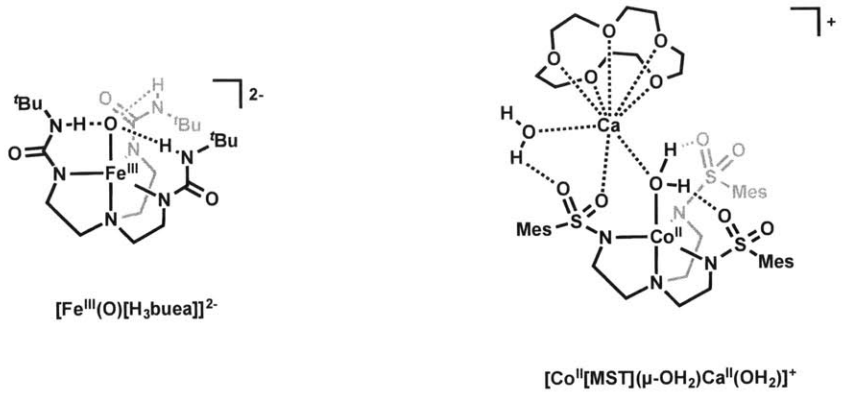

Figure 1.1 Metal complexes supported by hydrogen-bond donor (*left*) and acceptor (*right*) ligands reported by Borovik.

ate ligands within the context of olefin hydrogenation. These complexes contain a borate anion in their secondary coordination spheres that are rigidly held apart from the metal center by incorporation into the ligand backbone. The borate moiety, while non-coordinating, is electronically important, rendering the ligands either anionic, five-electron L_2X-type (tris(phosphine)borate) or anionic, three-electron LX-type (bis(phosphine)borate) species (Figure 1.2). Structurally similar to other LX-type and L_2X-type ligands, such as the bis(pyrazolyl)borate,[13] bis(carbene)borate,[14,15] tris(pyrazolyl)borate,[13] tris(thioether)borate,[16] tris(carbene)borate[17,18] and cyclopentadienyl ligand families,[3] the tris(phosphine)-borate and bis(phosphine)borate ligands are more electron-rich than many of the ligands listed above by virtue of their electron-releasing phosphine donors.[19,20]

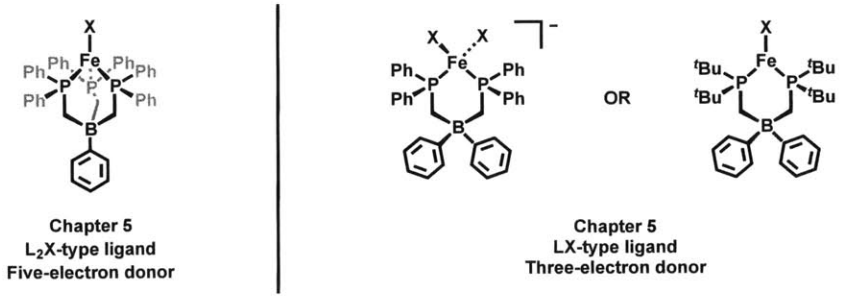

Figure 1.2 General forms of the iron tris(phosphine)borate (*left*) and bis(phosphine)borate (*right*) complexes discussed in Chapter 5.

1.2 Aspects of Transition-Metal Complexes Featuring Z-Type Ligands

The role of metal-borane interactions and their ability to mediate E–H bond activation processes are central to this dissertation. Described in Chapters 2, 3 and 4 are complexes of neutral tris(phosphine)borane and bis(phosphine)borane ligands (Figure 1.3, left).[21–24] These ligands feature two or three π-accepting phosphine ligands and a σ-accepting borane ligand. In contrast to the well-known L-type (two-electron donor) and X-type (one-electron donor) ligands, the coordination chemistry of such Z-type (zero-electron donor) ligands is far less developed (Figure 1.3, right). Following Hill's report of a Ru–B bond in $[B(mim^{Me})_3]Ru(CO)(PPh_3)$ (mim^{Me} = 2-mercapto-1-methylimidazolyl),[25] the number and type of transition-metal borane complexes has increased dramatically, including those of mid to late first-row transition metals.[24,26–38]

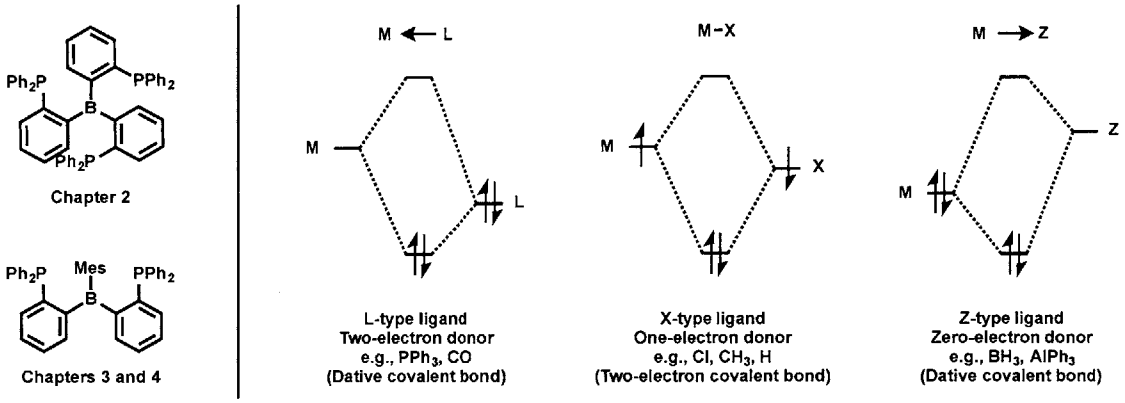

Figure 1.3 (*left*) Bis(phosphine)borane and tris(phosphine)borane ligands employed in this dissertation. (*right*) Molecular orbital representations of metal-ligand interactions with L-, X- and Z-type ligands.[39]

$M–BR_3$ interactions are straightforward. When bound to a transition metal, the otherwise trigonal borane boron atom is pyramidalized to some extent. Because free boranes have no lone pairs, the electrons in the M–B bond originate exclusively from the metal center, resulting in a σ-acceptor interaction. However, the formalisms associated with assignment of the d-electron count and metal oxidation state can complicate the description of such interactions. Parkin[40] and Hill[41] have proposed two bonding scenarios for complexes

featuring BR_3 ligands (Figure 1.4). The first situation fragments the M−BR_3 complex such that the metal is oxidized by two electrons (d^{n-2}) with a dianionic BR_3^{2-} ligand (Figure 1.4, left). The second situation retains the original d^n configuration of the metal center with a neutral BR_3 ligand (Figure 1.4, right). The two proposals are the limiting bonding situations and are related by the extent of electron transfer from the metal to the boron center; however, both descriptions are problematic. Parkin's proposal (Figure 1.4, left) relies on the M−BR_3 bond being polarized such that the electrons are assigned to the borane. In practice, this feature depends on a number of factors including, but not limited to, the identities of the metal center and the R groups bound to boron. Exclusive assignment of the electrons to the borane can therefore be ambiguous and incorrect. Hill's model treats the metal and borane as one unit and assigns a single electron count (e.g., $(Fe-B)^7$); this notation is similar to the Enemark-Feltham description of metal nitrosyl complexes.[41] Although this method recognizes the potential ambiguity in rigorously assigning electrons to the metal or the borane, it cannot describe the extent of M−B bonding in the complex.

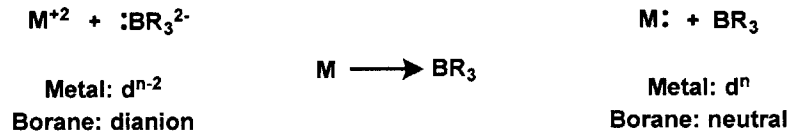

Figure 1.4 Limiting descriptions of M−B interactions proposed by (*left*) Parkin and (*right*) Hill.

For the purposes of the following discussion, only C_3-symmetric borane ligands bound to first-row transition metals will be considered. Structurally characterized complexes of the S-donor ligands $[B(Pn^R)_3]$ ($[B(Pn^R)_3]$ = tris(mercapto-R-pyridazinyl)borate; R = ^{t}Bu or Me) and $[B(mim^{tBu})_3]$ (mim^{tBu} = 2-mercapto-1-tert-butylimidazolyl) feature short M−B distances (1.98 − 2.13 Å) and highly pyramidalized boron centers (Σ(N−B−N) = 326 − 335°).[30,32–35,37] These features indicate that there is a significant interaction between the metal and boron centers and that Parkin's model is an appropriate description of the M−B bonding in these complexes. In contrast, complexes of the P-donor ligand $[TPB^{iPr}]$ ($[TPB^{iPr}] = [(2\text{-}^iPr_2PC_6H_4)_3B]$) have much more variable M−B distances (2.17 − 2.61 Å) and degrees of pyramidalization at boron (Σ(C−B−C) = 330 − 355°).[26,28,28,31,36,42] Figure 1.5 shows a graph correlating the M−B distance with the pyramidalization at boron for

structurally characterized first-row transition-metal complexes ligated by S- and P-donor borane ligands (center). This plot highlights an important aspect of the [TPB^{iPr}] ligand: the M−B interaction is highly flexible and can adjust according to the electronic requirements of the metal center (e.g., overall charge, identity of the metal, identity of the ancillary ligands, etc). Given the variability of the M−B interaction and, as a consequence, the extent of the electron donation from the metal to the boron center and the covalency of this interaction, it is clear that the concept of oxidation states is ill-equipped to describe the bonding in complexes ligated by [TPB^{iPr}].

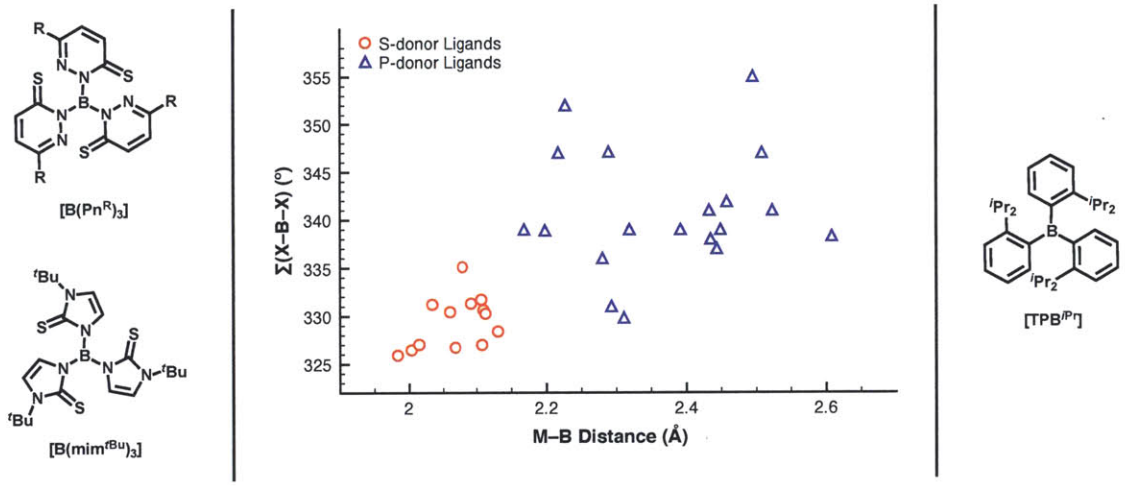

Figure 1.5 C_3-symmetric (*left*) S-donor and (*right*) P-donor borane ligands. (*center*) Plot correlating M−B distance and the pyramidalization of the boron center for first-row transition metal complexes.[43]

In the future, boron K-edge XAS could prove to be a powerful probe of the strength of a M−B interaction, however it is not yet a routine or widely accessible technique due to the technical difficulties associated with low-energy data collection. To assess the extent of a M−B interaction, there are only a few techniques in the synthetic chemists' toolbox. For diamagnetic complexes, the $^{11}B\{^1H\}$ NMR shift is a convenient and reliable measure of the electron density at boron, with more upfield shifted resonances corresponding to an increase in electron density and the formation of an adduct.[44,45] For $S = 1/2$ species, EPR is a valuable technique; in order to determine the amount of boron character in the M−B unit, the unpaired spin must reside in the M−B orbital such that the hyperfine coupling to boron can be resolved. Chapter 2 explores the iron chemistry of an aryl-substituted [TPB] ligand

in an effort to modify the donor-acceptor relationship between the iron and boron centers and probe the lower limits of their interaction. A number of paramagnetic complexes are described for which information about the M−B interaction cannot be readily acquired via NMR or EPR spectroscopy. Thus, we rely on X-ray crystallography, which is the most general method for evaluating the M−B interactions of both diamagnetic and paramagnetic species, albeit with some limitations (vide infra).

Strong M−B bonding should result in a number of physical observables: an upfield shifted $^{11}B\{^{1}H\}$ NMR spectrum (for a diamagnetic species), a short M−B distance and a pyramidalized boron center. The structural parameters for the [TPB^{iPr}] complexes illustrated in Figure 1.5 (center) indicate weaker M−B interactions in comparison to those of S-donor borane ligands. The correlation of the metrical parameters obtained by X-ray crystallographic analyses can be ambiguous if the distance or pyramidalization are intermediate in value (i.e., a long M−B distance coupled with a highly pyramidalized boron center or a short M−B distance coupled with a nearly planar boron center, vide supra). An example of the flexibility of the M−B interaction and correlation with the pyramidalization of boron as a function of the Lewis basicity of the metal center is shown in Figure 1.6.[36] As expected, the Cu−B distance of [TPB^{iPr}]Cu decreases upon reduction to the anionic complex [[TPB^{iPr}]Cu][Na] (2.289 Å vs 2.198 Å). Oxidation of [TPB^{iPr}]Cu to the cationic species [[TPB^{iPr}]Cu][BAr$^{F}_{4}$] results in an increase of the Cu−B distance from 2.289 Å to 2.495 Å. The pyramidalization at boron decreases with each one-electron oxidation, resulting in a nearly planar boron center in the cationic species. This lack of pyramidalization indicates that there is little to no Cu−B interaction. Of the reported structurally characterized [TPB^{iPr}] complexes, the imidoiron species [TPB^{iPr}]FeN(*p*-(OMe)C$_6$H$_4$) has the longest M−B distance at 2.608 Å.[28] Based on the copper series discussed above, one would assume that long M−B distances equate to near-zero interaction and that there is no interaction between the iron and boron centers of the imidoiron complex. However, the pyramidalization at boron is significant (338°), indicating that there is some degree of Fe−B interaction, despite the long distance. This ambiguity will arise again in Chapter 2. In addition, the preparation of a [TPB]Fe complex in which the Fe−B interaction is unequivocally absent will be presented.

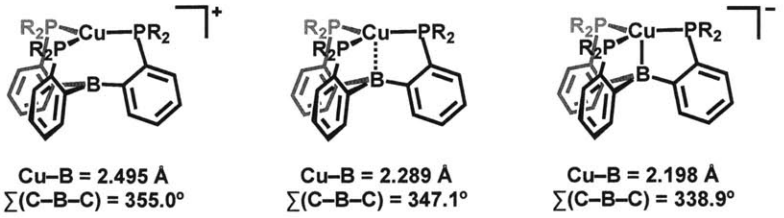

Figure 1.6 A family of copper metallaboratranes related by formal redox processes (R = ^{i}Pr).

1.3 Bifunctional Catalysis

The Lewis acidic functionality of Z-type borane ligands can accommodate lower transition-metal oxidation states by direct interaction with the metal center; in principle, the borane can also operate in tandem with the metal center to activate small-molecule substrates[24,30,33,46–50] As an extension this bifunctional concept, the interaction of a transition-metal center with a Lewis acidic borane can be considered a minimal heterobimetallic system in which the borane mimics a second metal center. These complexes have a distinct advantage over traditional heterobimetallic species in that the second "metal" is pre-installed in the ligand framework.[48] This strategy could help circumvent the deleterious one-electron processes typically associated with first-row transition-metal complexes in favor of concerted two-electron transformations such as those observed for hydrogenation and hydrosilylation processes.

The Peters group recently reported the reversible H_2 addition across a nickel bis(phosphine)borane species, as shown in Figure 1.7 (left).[24] Heterolysis of H_2 by [^{Mes}DPB^{Ph}]Ni results in the nickel borohydridohydride species [^{Mes}DPB^{Ph}](H)Ni(H) (^{Mes}DPB^{Ph} = (2-$Ph_2PC_6H_4)_2B(1,3,5\text{-}Me_3C_6H_2)$). This reaction is conceptually related to H_2 activation by frustrated Lewis pairs (FLPs).[51] However, the polarity of this transformation is inverted relative to typical H_2 heterolysis reactions, in which the metal center acts as the Lewis acid and accepts H^- while an internal or exogeneous base accepts H^+.[52] For [^{Mes}DPB^{Ph}]Ni, the nickel center acts as the Lewis acid and accepts H^+ and the Lewis acidic borane accepts H^- (Figure 1.7, right). The few reported examples of transition metal/FLP systems also display this reactivity.[53,54] An important feature of the [^{Mes}DPB^{Ph}]Ni system is that

the activated metal hydride/borohydride pair can be intercepted by olefins to achieve catalytic olefin hydrogenation. Inspired by these results, Chapters 3 and 4 explore Si−H and S−H bond activation by [^{Mes}DPB^{Ph}]Ni, in an effort to effect catalytic functionalization of small molecules, a major goal set out at the beginning of this introduction. Chapter 3 describes the catalytic hydrosilylation of substituted benzaldehydes and outlines a mechanistic proposal for this transformation based on detailed NMR experiments. In Chapter 4, the S−H bond activation of substituted thiophenols is discussed. While catalytic processes incorporating this bond activation process have not yet been realized with [^{Mes}DPB^{Ph}]Ni, a rare nickel(I) borohydridothiolate complex has been isolated and its solid-state structure is described. Taken together, Chapters 3 and 4 demonstrate not only the capacity of the [^{Mes}DPB^{Ph}] ligand scaffold to stabilize unusual and reactive species, but also its flexibility and ability to support first-row transition-metal catalysts that can mediate productive two-electron processes typically carried out by noble-metal catalysts.

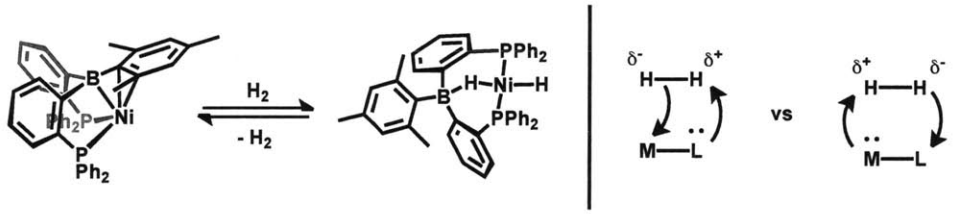

Figure 1.7 (*left*) The nickel bis(phosphine)borane species [^{Mes}DPB^{Ph}]Ni heterolytically cleaves H_2 to generate the nickel borohydridohydride species [^{Mes}DPB^{Ph}](H)Ni(H). (*right*) Typical and polarity-inverted heterolysis of H_2 at a transition metal-ligand species.

1.4 Bibliography

[1] Tolman, W. B. *Activation of Small Molecules*; Wiley-VCH: Weinheim, Germany, 2006.

[2] Hartwig, J. F. *Organotransition Metal Chemistry: From Bonding to Catalysis*; University Science Books: Sausalito, CA, 2010.

[3] Crabtree, R. H. *The Organometallic Chemistry of the Transition Metals*; John Wiley & Sons: New York, 2001.

[4] Colby, D. A.; Bergman, R. G.; Ellman, J. A. *Chem. Rev.* **2010**, *110*, 624–655.

[5] Chalk, A. J.; Harrod, J. F. *J. Am. Chem. Soc.* **1965**, *87*, 16–21.

[6] Furuya, T.; Benitez, D.; Tkatchouk, E.; Strom, A. E.; Tang, P.; Goddard, W. A., III; Ritter, T. *J. Am. Chem. Soc.* **2010**, *132*, 3793–3807.

[7] Culkin, D. A.; Hartwig, J. F. *Organometallics* **2004**, *23*, 3398–3416.

[8] Johns, A. M.; Utsunomiya, M.; Incarvito, C. D.; Hartwig, J. F. *J. Am. Chem. Soc.* **2006**, *128*, 1828–1839.

[9] Takaya, J.; Hartwig, J. F. *J. Am. Chem. Soc.* **2005**, *127*, 5756–5757.

[10] Borovik, A. S. *Acc. Chem. Res.* **2005**, *38*, 54–61.

[11] MacBeth, C. E.; Golombek, A. P.; Young, V. G., Jr; Yang, C.; Kuczera, K.; Hendrich, M. P.; Borovik, A. S. *Science* **2000**, *289*, 938–941.

[12] Lacy, D. C.; Park, Y. J.; Ziller, J. W.; Yano, J.; Borovik, A. S. *J. Am. Chem. Soc.* **2012**, *134*, 17526–17535.

[13] Trofimenko, S. *Scorpionates: The Coordination Chemistry of Polypyrazolylborate Ligands*; Imperial College Press: London, 1999.

[14] Nieto, I.; Bontchev, R. P.; Smith, J. M. *Eur. J. Inorg. Chem.* **2008**, *2008*, 2476–2480.

[15] Fränkel, R.; Kniczek, J.; Ponikwar, W.; Nöth, H.; Polborn, K.; Fehlhammer, W. P. *Inorg. Chim. Acta* **2001**, *312*, 23–39.

[16] Ge, P.; Haggerty, B. S.; Rheingold, A. L.; Riordan, C. G. *J. Am. Chem. Soc.* **1994**, *116*, 8406–8407.

[17] Nieto, I.; Cervantes-Lee, F.; Smith, J. M. *Chem. Commun.* **2005**, 3811–3813.

[18] Kernbach, U.; Ramm, M.; Luger, P.; Fehlhammer, W. P. *Angew. Chem. Int. Ed. Engl.* **1996**, *35*, 310–312.

[19] Thomas, J. C.; Peters, J. C. *Inorg. Chem.* **2003**, *42*, 5055–5073.

[20] Feldman, J. D.; Peters, J. C.; Tilley, T. D. *Organometallics* **2002**, *21*, 4050–4064.

[21] Bontemps, S.; Bouhadir, G.; Dyer, P. W.; Miqueu, K.; Bourissou, D. *Inorg. Chem.* **2007**, *46*, 5149–5151.

[22] Kameo, H.; Hashimoto, Y.; Nakazawa, H. *Organometallics* **2012**, *31*, 3155–3162.

[23] Bontemps, S.; Gornitzka, H.; Bouhadir, G.; Miqueu, K.; Bourissou, D. *Angew. Chem. Int. Ed.* **2006**, *45*, 1611–1614.

[24] Harman, W. H.; Peters, J. C. *J. Am. Chem. Soc.* **2012**, *134*, 5080–5082.

[25] Hill, A. F.; Owen, G. R.; White, A. J. P.; Williams, D. J. *Angew. Chem. Int. Ed.* **1999**, *38*, 2759–2761.

[26] Anderson, J. S.; Moret, M.-E.; Peters, J. C. *J. Am. Chem. Soc.* **2013**, *135*, 534–537.

[27] Suess, D. L. M.; Peters, J. C. *J. Am. Chem. Soc.* **2013**, *135*, 4938–4941.

[28] Moret, M.-E.; Peters, J. C. *Angew. Chem. Int. Ed.* **2011**, *50*, 2063–2067.

[29] Moret, M.-E.; Peters, J. C. *J. Am. Chem. Soc.* **2011**, *133*, 18118–18121.

[30] Figueroa, J. S.; Melnick, J. G.; Parkin, G. *Inorg. Chem.* **2006**, *45*, 7056–7058.

[31] Suess, D. L. M.; Tsay, C.; Peters, J. C. *J. Am. Chem. Soc.* **2012**, *134*, 14158–14164.

[32] Nuss, G.; Saischek, G.; Harum, B. N.; Volpe, M.; Gatterer, K.; Belaj, F.; Mösch-Zanetti, N. C. *Inorg. Chem.* **2011**, *50*, 1991–2001.

[33] Pang, K.; Tanski, J. M.; Parkin, G. *Chem. Commun.* **2008**, 1008–1010.

[34] Mihalcik, D. J.; White, J. L.; Tanski, J. M.; Zakharov, L. N.; Yap, G. P. A.; Incarvito, C. D.; Rheingold, A. L.; Rabinovich, D. *Dalton Trans.* **2004**, 1626–1634.

[35] Senda, S.; Ohki, Y.; Hirayama, T.; Toda, D.; Chen, J.-L.; Matsumoto, T.; Kawaguchi, H.; Tatsumi, K. *Inorg. Chem.* **2006**, *45*, 9914–9925.

[36] Moret, M.-E.; Zhang, L.; Peters, J. C. *J. Am. Chem. Soc.* **2013**, *135*, 3792–3795.

[37] Nuss, G.; Saischek, G.; Harum, B. N.; Volpe, M.; Belaj, F.; Mösch-Zanetti, N. C. *Inorg. Chem.* **2011**, *50*, 12632–12640.

[38] Sircoglou, M.; Bontemps, S.; Mercy, M.; Miqueu, K.; Ladeira, S.; Saffon, N.; Maron, L.; Bouhadir, G.; Bourissou, D. *Inorg. Chem.* **2010**, *49*, 3983–3990.

[39] Parkin, G. In *Comprehensive Organometallic Chemistry III*; Crabtree, R. H., Mingos, D. M. P., Eds.; Elsevier: Oxford, 2007; pp 1–57.

[40] Parkin, G. *Organometallics* **2006**, *25*, 4744–4747.

[41] Hill, A. F. *Organometallics* **2006**, *25*, 4741–4743.

[42] Sircoglou, M.; Bontemps, S.; Bouhadir, G.; Saffon, N.; Miqueu, K.; Gu, W.; Mercy, M.; Chen, C.-H.; Foxman, B. M.; Maron, L.; Ozerov, O. V.; Bourissou, D. *J. Am. Chem. Soc.* **2008**, *130*, 16729–16738.

[43] Braunschweig, H.; Dewhurst, R. D. *Dalton Trans.* **2011**, *40*, 549–558.

[44] Welch, G. C.; Holtrichter-Roessmann, T.; Stephan, D. W. *Inorg. Chem.* **2008**, *47*, 1904–1906.

[45] Jacobsen, H.; Berke, H.; Döring, S.; Kehr, G.; Erker, G.; Fröhlich, R.; Meyer, O. *Organometallics* **1999**, *18*, 1724–1735.

[46] Fong, H.; Moret, M.-E.; Lee, Y.; Peters, J. C. *Organometallics* **2013**, *32*, 3053–3062.

[47] Owen, G. R. *Chem. Soc. Rev.* **2012**, *41*, 3535–3546.

[48] Krogman, J. P.; Foxman, B. M.; Thomas, C. M. *J. Am. Chem. Soc.* **2011**, *133*, 14582–14585.

[49] Tsoureas, N.; Kuo, Y.-Y.; Haddow, M. F.; Owen, G. R. *Chem. Commun.* **2011**, *47*, 484–486.

[50] Miller, A. J. M.; Labinger, J. A.; Bercaw, J. E. *J. Am. Chem. Soc.* **2008**, *130*, 11874–11875.

[51] Stephan, D. W.; Erker, G. *Angew. Chem. Int. Ed.* **2010**, *49*, 46–76.

[52] Rakowski Dubois, M.; DuBois, D. L. *Acc. Chem. Res.* **2009**, *42*, 1974–1982.

[53] Chapman, A. M.; Haddow, M. F.; Wass, D. F. *Eur. J. Inorg. Chem.* **2012**, *2012*, 1546–1554.

[54] Chapman, A. M.; Haddow, M. F.; Wass, D. F. *J. Am. Chem. Soc.* **2011**, *133*, 18463–18478.

2 Exploring the Lower Limits of An Iron→Tris(phosphine)borane Interaction

Contents

2.1 Introduction and Motivation

The transition metal-mediated activation of small molecules such as O_2, H_2O, CO_2 and N_2 proceeds via multistep, multielectron processes. These metal species must be able to access a range of oxidation states, accommodate both π-acidic and π-basic ligands and avoid the formation of overly stable, high-valent intermediates containing metal-ligand multiple bonds. Nature employs redox-active ligands, multimetallic species and redox-active clusters as electron reservoirs to overcome these challenges. For example, cytochrome P450 carries out the four-electron reduction of O_2 by utilizing an electron from a porphyrin ligand to generate an iron(IV) porphyrin radical cation that serves as a masked iron(V) species.[1] Rubrerythrin contains a redox-active, symmetric diiron site to avoid the formation of high-valent diferryl or ferric/ferryl species upon reaction with peroxide or O_2.[2] In the oxygen evolving complex (OEC) of photosystem II (PSII), a manganese-oxo cluster serves as a redox reservoir.[3] These motifs have been exploited in synthetic systems and have inspired an extremely active, ongoing area of research.[4–9]

To address the redox requirements of multielectron processes in synthetic systems, the Peters group has investigated the chemistry of iron tris(phosphine)borate [$PhBP^R_3$] ([$PhBP^R_3$] = $PhB(CH_2PR_2)^-_3$)[10,11] and tris(phosphine)silyl [SiP^R_3] ([SiP^R_3] = $(2\text{-}R_2PC_6H_4)_3\text{-}Si^-$)[12] complexes, primarily focusing on the activation and fixation of N_2. To this end, the [$PhBP^R_3$] scaffold was found to be particularly useful in the formation of metal-ligand multiply bonded species, such as imidoiron and nitridoiron complexes, while the [SiP^R_3] framework was better able to stabilize terminal N_2 species. The qualitative d-orbital splitting diagrams of both systems underscore the differences in reactivity and the limitations of each

ligand (Figure 2.1). For [$PhBP^R_3$] complexes, the empty, high-lying π-antibonding (d_{xz}, d_{yz}) orbitals allow for the stabilization of metal-ligand multiple bonds, as shown for the pseudotetrahedral complex [$PhBP^R_3$]FeN (Figure 2.1, left).[10,13–15] However, due to the difficulty of implementing sufficient steric protection at the metal center, no terminal N_2 complex of [$PhBP^R_3$]Fe has been accessed.[15] In contrast, terminal N_2 complexes of [SiP^R_3]Fe have been prepared in three different oxidation states.[16] However, inspection of the d-orbital splitting diagram of the trigonal bipyramidal complex [SiP^R_3]Fe(N_2) quickly informs the reader that this framework is not suitable for accommodating metal-ligand multiple bonds as a result of the occupied, low-lying π-antibonding orbitals (Figure 2.1, right). The purported imidoiron species [SiP^{iPr}_3]FeN(*p*-tolyl) can be observed by EPR spectroscopy in a frozen glass; upon warming to room temperature, this species rapidly converts to [SiP^{iPr}_3]Fe(N_2) and (*p*-tolyl)N=N(*p*-tolyl).[17]

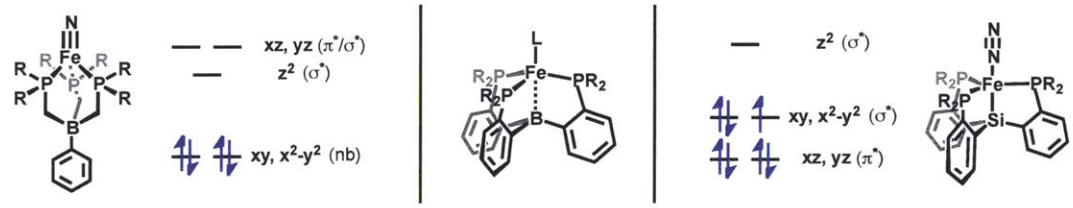

Figure 2.1 Qualitative d-orbital splitting diagrams for the tris(phosphine)borate scaffold (*left*) and tris(phosphine)silyl scaffold (*right*). (*center*) A hemi-labile tris(phosphine)borane ligand can access both pseudotetrahedral and trigonal bipyramidal geometries.

Drawing on the lessons above, a flexible ligand scaffold uniting the pseudotetrahedral and trigonal bipyramidal electronic structures is of obvious interest. Both these and intermediate geometries can be accessed with a single tetradentate NL_3-type ligand (L = phosphine,[18,19] N-heterocyclic carbene[20]). The geometries of these complexes are sensitive to the identity of the ligand in the fifth binding site. For example, the Fe–N donor interaction of [$TIMEN^{Mes}$]Fe ([$TIMEN^{Mes}$] = tris[2-(3-mesityl-imidazol-2-ylidene)ethyl]amine) complexes contracts in the absence of a fifth ligand to give a trigonal pyramidal complex ([[$TIMEN^{Mes}$]Fe][BPh_4]) and expands in the presence of a π-basic nitride ligand to give a pseudotetrahedral species ([[$TIMEN^{Mes}$]FeN][BPh_4]).[20] The Peters group has recently demonstrated that similar behavior may be achieved with a Lewis acidic borane in the apical position (Figure 2.1, center).[21,22] Iron complexes supported by the previously

reported tris(phosphine)borane ligand [TPB^{iPr}] ([TPB^{iPr}] = [(2-$^{i}Pr_2PC_6H_4)_3B$])[23] display flexible Fe−B bond distances (2.29 to 2.61 Å) depending on the nature of the fifth ligand.[22] Species with both π-acidic N_2 and π-basic NR ligands were isolated and structurally characterized (Scheme 2.1). Intrigued by these results, we sought to further explore the chemistry of [TPB^{R}]Fe complexes. Herein is described the chemistry of a less electron-rich tris(phosphine)borane scaffold in an effort to modify the donor-acceptor relationship between the iron and boron centers and probe the lower limits of their interaction.

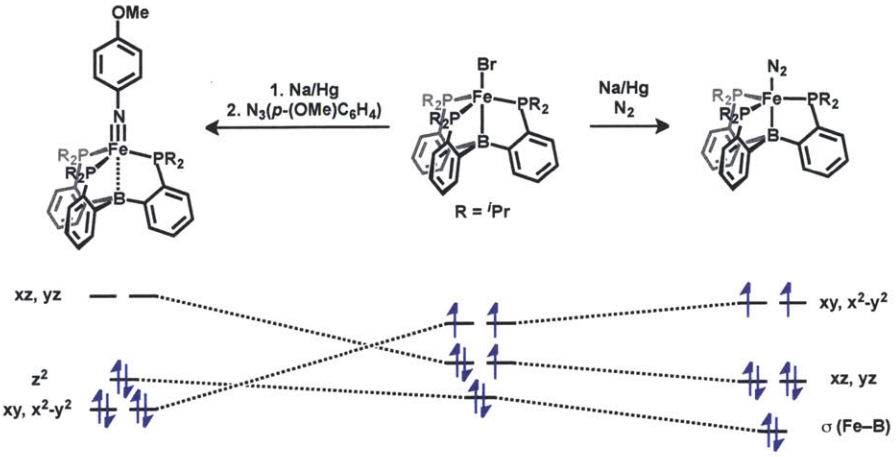

Scheme 2.1 Both π-acidic and π-basic ligands can be accessed by iron complexes supported by the tris(phosphine)borane ligand, [TPB^{iPr}].

2.2 Accessing the Iron Chemistry of [TPB^{Ph}]

The tris(phosphine)borane ligand [TPB^{Ph}] (**2.1**) is prepared by low temperature *ortho*-lithiation of 2-$Ph_2PC_6H_4Br$ with ^{n}BuLi and subsequent addition of 1/3 equiv of BCl_3 at −78 °C (Scheme 2.2). Isolated as a white powder in ca. 90% yield, **2.1** is soluble in THF, C_6H_6 and chlorinated solvents. Ligand **2.1** is thermally robust; no decomposition was observed after heating a THF solution of **2.1** to 100 °C over the period of 1 week. The room temperature $^{31}P\{^{1}H\}$ NMR spectrum of **2.1** in $CDCl_3$ features a singlet at −9.0 ppm. The $^{11}B\{^{1}H\}$ NMR resonance appears as a broad feature centered at −7.6 ppm. In general, free triarylboranes appear at ca. 70 ppm[24,25] and triarylborane-phosphine adducts appear at ca. −10 ppm.[26,27] The significantly upfield shifted $^{11}B\{^{1}H\}$ NMR resonance

of **2.1** implies greater electron density at the boron center, which likely manifests itself as an intramolecular P→B interaction. This interaction was also observed for [TPB^{iPr}]; at −100 °C in THF-d_8, the $^{31}P\{^1H\}$ NMR spectrum features two singlets centered at 26.1 and −2.1 ppm, corresponding to the one phosphine involved in the P→B interaction and the two free phosphines, respectively.[23] In contrast, cooling a THF solution of **2.1** to −80 °C does not result in splitting of the $^{31}P\{^1H\}$ NMR resonance to reflect an intramolecular P→B interaction.

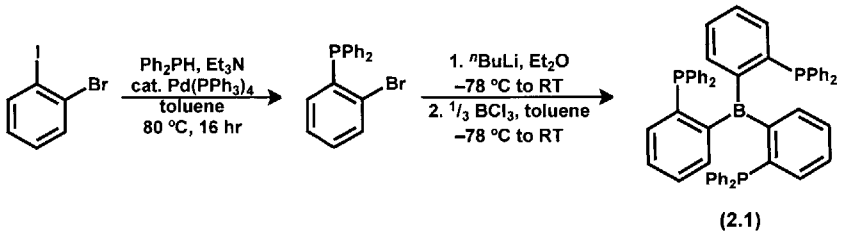

(2.1)

Scheme 2.2 Synthesis of the tris(phosphine)borane ligand **2.1**.

During completion of the work contained in this chapter, Nakazawa reported the synthesis of **2.1** by a route similar to that described above, with additional heating to 110 °C after the addition of BCl_3.[28] This report described the solid-state structure of **2.1** and it is pertinent to discuss the differences between it and the structure of [TPB^{iPr}] obtained by Bourissou.[23] The solid-state structure of [TPB^{iPr}] features two phosphines above and one phosphine below the C_3 plane defined by the boron-bound carbon atoms. In addition, there is one very short P−B distance (2.15 Å vs 3.27 and 3.31 Å), indicative of an intramolecular P→B interaction. The boron center of [TPB^{iPr}] is pyramidalized as a result of the P→B interaction, with the sum of the C−B−C angles being 348.9(3)°. The structure of **2.1** however, does not exhibit the same P→B interaction. Instead, the three phosphines lie above the C_3 plane, with the closest P−B distance being 3.09 Å. The sum of the C−B−C angles is 357.1(3)°, indicating near planar geometry at boron. A graphical representation summarizing the two structures is shown in Figure 2.2.

In his efforts to gain entry to the iron chemistry of [TPB^{iPr}], Moret developed a reliable synthetic route for the installation of the neutral borane on a low-valent iron center. Moret found that comproportionation of $FeBr_2$ and 12 equiv of iron powder in the presence of [TPB^{iPr}] (THF, 90 °C, 3 d), yielded [TPB^{iPr}]FeBr in high yield.[22] This compropor-

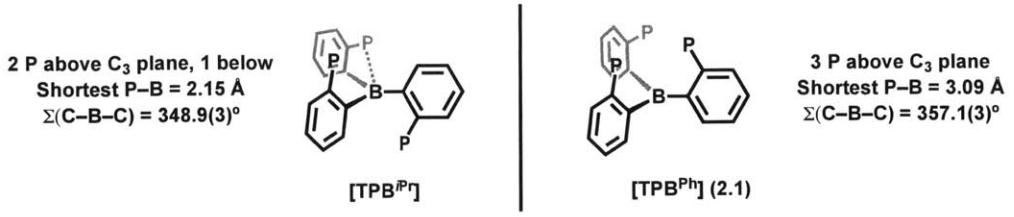

Figure 2.2 Graphical representations of the solid-state structures of [TPB$^{i\text{Pr}}$] (*left*) and **2.1** (*right*). The C_3 plane is defined by the three carbon atoms bound to boron.

tionation method is readily applied to the generation of [TPB$^{\text{Ph}}$]FeCl (**2.2**), as shown in Scheme 2.3. While free **2.1** is thermally stable in THF solution (vide supra), under the reducing conditions described above, an inconsistent and significant amount of PPh_3 is formed via B$-C_{aryl}$ bond cleavage of **2.1**. The formation of PPh_3 is dramatically attenuated by reducing the amount of iron powder and decreasing the reaction temperature. Thus, heating a THF slurry of **2.1**, $FeCl_2$, and 3 equiv of iron powder to 70 °C over 3 d yielded **2.2** as a dark brown powder in 75% yield. Once isolated, **2.2** is readily soluble in THF and sparingly soluble in toluene and C_6H_6.

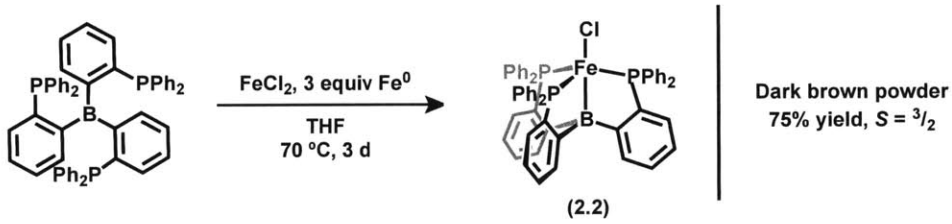

Scheme 2.3 Synthesis of the tris(phosphine)borane iron complex **2.2**.

Complex **2.2** is paramagnetic, with broad resonances in the ^{1}H NMR spectrum ranging from 35 to −25 ppm. The Evans method solution magnetic moment measurement (μ_{eff} = 4.0 μ_B, THF-d_8, 25 °C) is slightly higher than the spin-only value of 3.9 μ_B for three unpaired electrons. This S = 3/2 ground state is consistent with that observed for [TPB$^{i\text{Pr}}$]FeBr (Scheme 2.1).[22] X-ray crystallographic structure determination of **2.2** confirmed its assignment as a monomeric iron tris(phosphine)borane complex (Figure 2.3). Complex **2.2** crystallizes in the monoclinic space group $P2_1/c$, with one molecule in the asymmetric unit. The geometry at iron is best described as distorted trigonal bipyramidal (τ = 0.85),[29] with a nearly linear B–Fe–Cl linkage, at 175.64(4)°. The distortion from a

trigonal bipyramidal geometry is reflected in the inequivalent P−Fe−P angles (124.40(2)° vs 106.66(2)° and 110.99(2)°) and the non-90° B−Fe−P angles (74.13(4) – 77.98(4)°). These deviations may arise from an electronic distortion, but could also result from the steric requirements of the ligand framework. Indeed, examination of the crystal structure shows that of the six phenyl groups bound to the phosphorus atoms, three groups reside above the P_3 plane, two groups are orthogonal to the P_3 plane and one group lies in the P_3 plane. This last phenyl group is located within the largest P−Fe−P angle. The Fe−Cl distance of 2.2713(4) Å is typical and the elongated Fe−P distances (2.3325(4) – 2.3622(4) Å) are as expected for a high-spin complex.

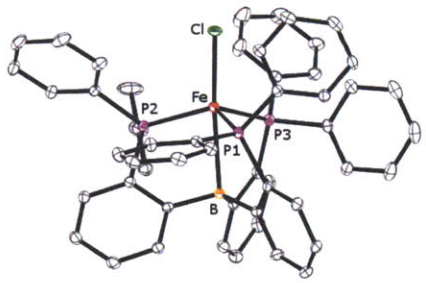

Selected Bond Lengths (Å) and Angles (°)
Fe–P (avg) = 2.3466(4)
P1–Fe–P2 = 124.40(2)
P1–Fe–P3 = 106.66(2)
P2–Fe–P3 = 110.99(2)
Fe–B = 2.542(2)
Σ(C–B–C) = 340.0(2)

Figure 2.3 Solid-state structure of **2.2**. Thermal ellipsoids are drawn at 40% probability. Hydrogen atoms are omitted for clarity.

As discussed in the introduction, although $^{11}B\{^1H\}$ NMR is a convenient tool for assessing the electron density at boron (i.e., for comparing the relative strengths of an intramolecular interaction), it is useless in the characterization of paramagnetic complexes featuring a M→B interaction, such as those described in this chapter. The M−B distance supports the presence or absence of a M→B interaction, however the distance alone is not a reliable parameter to compare the magnitude of the interaction.[30] For these complexes, the sum of the (C−B−C) angles should also be considered. In **2.2**, the Fe−B distance of 2.542(2) Å is long, however the boron is pyramidalized (Σ(C−B−C) = 340.0(2)°), indicating an interaction between iron and boron centers. A comparison of selected metrical parameters of **2.2** and [TPB^{iPr}]FeBr is given in Table 2.1.

Bond Length (Å)	**2.2**	[TPB^{iPr}]FeBr	Angle (°)	**2.2**	[TPB^{iPr}]FeBr
Fe–X	2.2713(4)	2.4138(8)	B–Fe–X	175.64(2)	173.7(1)
Fe–P1	2.3451(4)	2.403(1)	P1–Fe–P2	124.40(2)	106.82(5)
Fe–P2	2.3622(4)	2.383(1)	P1–Fe–P3	110.99(2)	113.82(5)
Fe–P3	2.3325(4)	2.435(1)	P2–Fe–P3	106.66(2)	122.09(5)
Fe–B	2.542(2)	2.458(5)	Σ(C–B–C)	340.0(2)	341.8(3)

Table 2.1 Comparison of selected bond lengths and angles of **2.2** and [TPB^{iPr}]FeBr.

2.3 Chemical Reduction of [TPB^{Ph}]FeCl: An Unexpected Product

An irreversible wave at −1.75 V vs Fc/Fc$^+$ in the cyclic voltammogram of **2.2** (0.4 M [^{n}Bu$_4$N][PF$_6$], THF) suggested the accessibility of a one-electron reduced species. The reduction event is anodically shifted 650 mV relative to [TPB^{iPr}]FeBr ($E_{1/2}$ = −2.40 V vs Fc/Fc$^+$).[22] Because reduction of **2.2** and [TPB^{iPr}]FeBr gives rise to two different one-electron reduced species (vide infra), the magnitude of $\Delta E_{1/2}$ cannot be discussed. However, the observed anodic shift is expected given the less electron-releasing nature of arylphosphines relative to alkylphosphines. A similar trend was observed for the Fe(II)/Fe(I) couple of tris(phosphine)borate complexes ($\Delta E_{1/2}$ = 320 mV)[11] and the Fe(III)/Fe(II) couple of tris(phosphine)silyl complexes ($\Delta E_{1/2}$ = 270 mV).[31]

In contrast to the chemistry of [TPB^{iPr}]FeBr, reduction of **2.2** does not lead to the expected "[TPB^{Ph}]Fe(N$_2$)" complex. Instead, treatment of a C_6H_6 slurry of **2.2** with 1.5 equiv of Na/Hg yielded a diamagnetic, dark red powder in ca. 90% yield. ^{1}H and ^{31}P$\{^1$H$\}$ NMR data indicate the product to be the one-electron reduced complex, [TPB$^{Ph'}$]Fe (**2.3**, Scheme 2.4). The room temperature ^{31}P$\{^1$H$\}$ NMR spectrum of **2.3** features three distinct resonances in a 1:1:1 ratio—two doublets, centered at 86.1 ($^2J_{PP}$ = 81.8 Hz) and 69.8 ppm ($^2J_{PP}$ = 82.2 Hz), and a singlet, centered at −12.1 ppm. The doublets arise from the coupling of two phosphorus atoms and their upfield shifts relative to free **2.1** (−12.9 ppm, C_6D_6) are consistent with metal-bound phosphines. The downfield shift of the singlet, on the other hand, is similar to that of free **2.1** and implies phosphine dissociation. The

asymmetry is further reflected in the ^{1}H NMR spectrum; in addition to the resonances corresponding to aryl protons, there are four resonances shifted upfield between 3.5 and 4.5 ppm and one resonance at 6.0 ppm (Figure 2.4). These chemical shifts are indicative of an iron-arene interaction and, given the geometric constraints of the ligand, the data are most consistent with an η^6-coordination of a phenyl group bound to the dissociated phosphine arm, as illustrated in Scheme 2.4. To rigorously assign the resonances associated with the bound phenyl group, 2D ^{1}H-^{13}C HSQC and HMBC NMR experiments were carried out to identify one, two and three bond correlations. The results of these experiments are summarized in Figure 2.4.

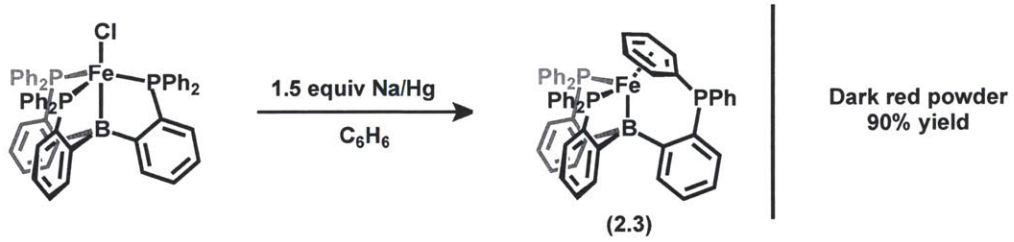

Scheme 2.4 Chemical reduction of **2.2** to generate the reduced iron-arene complex **2.3**.

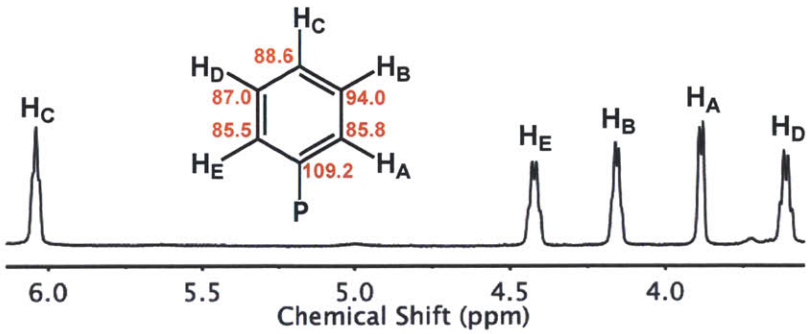

Figure 2.4 Partial ^{1}H NMR spectrum of **2.3** showing the upfield aryl resonances corresponding to the η^6-coordinated phenyl group. The corresponding ^{13}C$\{^{1}$H$\}$ NMR resonances are shown in red.

The assignment of **2.3** was confirmed by X-ray crystallographic analysis (Figure 2.5); complex **2.3** crystallizes in the orthorhombic space group $P2_12_12_1$, with one molecule in the asymmetric unit. The iron center is in a distorted three-legged piano stool configuration and features an η^6-arene interaction with one of the phenyl groups of the dissociated phosphine arm. The "legs" of the complex comprise the two coordinated phosphine arms

and the borane. The Fe···centroid distance is 1.593 Å and the Fe−P distances are as expected for a low-spin complex (2.1847(7) Å and 2.2465(7) Å). The Fe···C distances range from 2.095(2) Å (Fe−C1) to 2.172(2) Å (Fe−C4). The P−Fe−P angle (93.01(3)°) and P−Fe−B angles (78.42(6)° and 82.39(7)°) reflect the distortion from an idealized three-legged piano stool geometry. The Fe−B distance is 2.459(3) Å, which is ca. 0.08 Å shorter than in **2.2** (2.542(2) Å). As one might expect given the decrease in the Fe−B distance, the degree of pyramidalization at boron in **2.3** (Σ(C−B−C) = 334.3(3)°) is greater than in **2.2** (Σ(C−B−C) = 340.0(2)°).

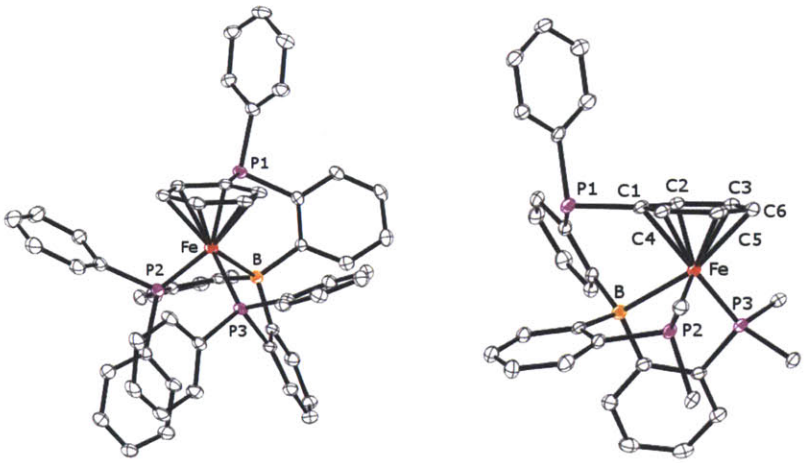

Figure 2.5 *(left)* Solid-state structure of **2.3**. Thermal ellipsoids are drawn at 40% probability. Hydrogen atoms and solvent molecules are omitted for clarity. *(right)* Thermal ellipsoid representation of **2.3** with aryl rings attached to P2 and P3 omitted for clarity. Selected bond lengths (Å) and angles (°): Fe−P (avg), 2.2156(7); Fe−B, 2.459(3); P2−Fe−P3, 93.01(3); P2−Fe−B, 78.42(6); P3−Fe−B, 82.39(7), Σ(C–B–C), 334.4(3).

2.4 Accessing M−L Multiple Bonds: Synthesis of Terminal Imidoiron Complexes

Despite the dechelation of a phosphine arm and the presence of an iron-arene interaction, **2.3** serves as a well-defined starting material for further transformations. For example, **2.3** can be treated with 1 atm of CO to cleanly generate a new, three-fold symmetric species bearing a carbonyl ligand, as determined by $^{31}P\{^{1}H\}$ and IR spectroscopy (77 ppm (br)

and 1885 cm^{-1}, respectively). This species is tentatively assigned as the carbonyl complex, [TPB^{Ph}]Fe(CO), however isolation of this species was not pursued. Treatment of **2.3** with 1.1 equiv of N_3Ad (N_3Ad = 1-azidoadamantane) in C_6H_6 at room temperature resulted in a color change from red to emerald green. Analysis of the reaction mixture by ^1H NMR spectroscopy after 6 hours indicated quantitative consumption of **2.3** concomitant with formation of a new, 3-fold symmetric species. Accordingly, the $^{31}P\{^1H\}$ NMR spectrum features a sharp singlet at 96.0 ppm; no N_3 vibrations were observed by IR spectroscopy. Crystallographic structure determination of the product from the reaction of **2.3** and N_3Ad established its identity as the adamantylimidoiron species, [TPB^{Ph}]FeNAd (**2.4**, Scheme 2.5). Complex **2.4** was obtained reproducibly in ca. 70% yield as an emerald green powder.

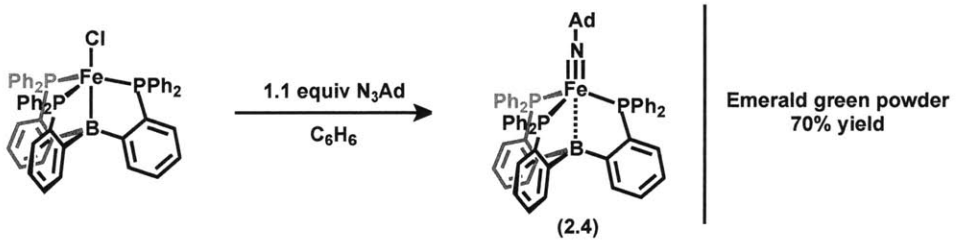

Scheme 2.5 Synthesis of the terminal imidoiron complex **2.4**.

Complex **2.4** crystallizes in the monoclinic space group *C*2/*c*, with one molecule in the asymmetric unit; the solid-state molecular structure reveals a four-coordinate iron center ligated by three phosphines and an adamantylimido fragment (Figure 2.6). The Fe–P distances range from 2.2051(6) to 2.2221(6) Å, as expected for a low-spin complex. The P–Fe–P angles range from 107.13(2) to 112.07(2)° and their sum is 330.54(3)°, close to the value of 328.5° for a regular tetrahedron. The very long Fe–B distance of 2.737 Å is ca. 0.2 Å longer than in **2.2** and 0.1 Å longer than that in the related [TPB^{iPr}]FeN(*p*-(OMe)C_6H_4) complex.[22] Taken together, these data indicate that the geometry at iron is best described as pseudotetrahedral. Interestingly, despite the increase in the Fe–B distance, the pyramidalization at boron in **2.4** is very similar to that in **2.2** (342.0(3)° and 340.0(2)°, respectively), indicating that even at such a long distance, there is still an interaction between the iron and boron centers. The Fe–N–C linkage is linear (178.3(1)°) and the Fe–N dis-

tance of 1.6333(2) Å is consistent with other structurally characterized terminal imidoiron complexes reported in the literature.[10,13,15,32–37] These features, in addition to the $S = 0$ ground state, collectively indicate Fe−N multiple bonding character in the complex.

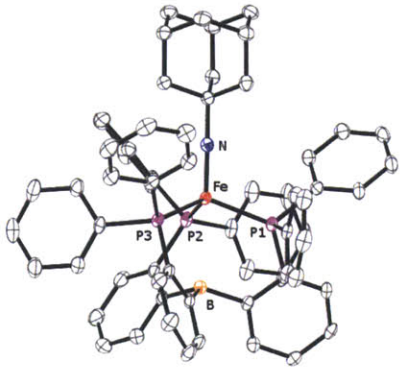

Selected Bond Lengths (Å) and Angles (°)
Fe–N = 1.6333(2)
Fe–N–C = 178.3(1)
Fe–P (avg) = 2.2104(6)
∑(P–Fe–P) = 330.54(3)
Fe–B = 2.737
∑(C–B–C) = 342.0(3)

Figure 2.6 Solid-state structure of **2.4**. Thermal ellipsoids are drawn at 40% probability. Hydrogen atoms are omitted for clarity.

Lowering the symmetry of a tetrahedral ligand field for a d^6 iron species, coupled with the strong axial distortion expected for a tripodal ligand, yields the qualitative C_{3v} d-orbital splitting diagram illustrated in Figure 2.7 (left).[10] Here, the orbital of a_1 symmetry is stabilized via a decrease in the angular overlap between the ligands and d_{z^2}. This a_1 orbital lies low in energy, close to the nearly degenerate nonbonding orbitals of $d_{x^2-y^2}$ and d_{xy} character. A single point energy calculation on **2.4** provides an electronic structure picture consistent with this analysis (Figure 2.7, right). The calculation predicts that the orbital of d_{z^2} (and Fe−B σ-bonding character) character lies lowest in energy (HOMO−2) and the HOMO is of d_{xy} parentage; the unoccupied π^* and σ^* orbitals with d_{xz} and d_{yz} character lie still higher in energy. Lobal representations of the HOMO−2, HOMO and LUMO+1 orbitals are shown in Figure 2.8.

The cyclic voltammogram of **2.4** (0.4 M [^{n}Bu$_4$N][PF$_6$], THF) reveals very different features from those observed in the related [PhBP$^R_3$]FeNAd and [PhBP$^{t\text{Bu}}_2$(pz)]FeNAd complexes. The cyclic voltammograms of [PhBP$^R_3$]FeNAd show reversible Fe(III)/Fe(II) couples (−1.79 and −1.32 V vs Fc/Fc$^+$ for R = ^{i}Pr and Ph, respectively) and irreversible Fe(IV)/Fe(III) couples (−0.45 and −0.35 V vs Fc/Fc$^+$ for R = ^{i}Pr and Ph, respectively).[13,15] The cyclic voltammogram of the mixed donor species, [PhBP$^{t\text{Bu}}_2$(pz)]FeNAd, features an

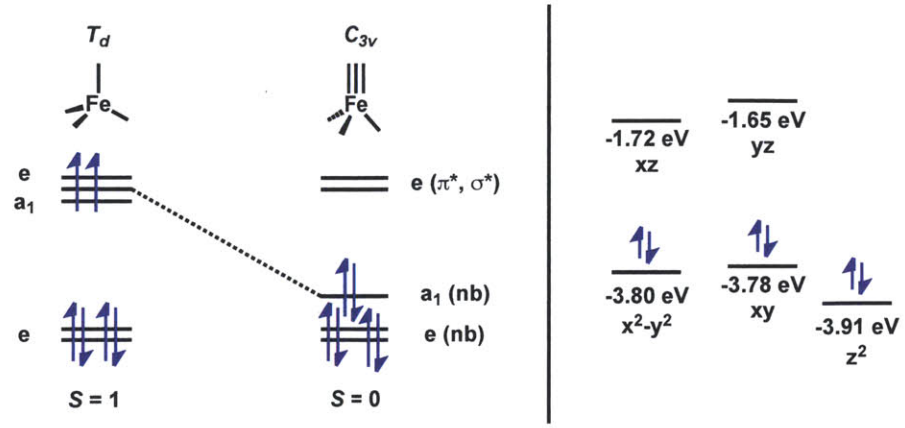

Figure 2.7 (*left*) Qualitative d-orbital splitting diagrams illustrating the predicted ground-state electronic structures of T_d and C_{3v} symmetric structures for d^6 configurations. For the C_{3v} species, the orbital of a_1 symmetry with d_{z^2} character lies close in energy to the nonbonding orbitals of $d_{x^2-y^2}$ and d_{xy} character. (*right*) Calculated electronic structure (DFT, Gaussian 09, M06L, 6-31G(d,p)) of imidoiron **2.4**.

irreversible Fe(III)/Fe(II) couple (-2.2 V vs Fc/Fc^+) and a reversible Fe(IV)/Fe(III) couple (-0.72 V vs Fc/Fc^+).[33] In contrast, the cyclic voltammogram of **2.4** exhibits two redox features: a reversible event centered at -0.42 V vs Fc/Fc^+ and a second, quasi-reversible event centered at 0.38 V vs Fc/Fc^+ (Figure 2.9). The quasi-reversible wave becomes fully reversible upon increasing the scan rate to 500 mV/s. The open circuit potential rests at -0.58 V vs Fc/Fc^+ and so these waves can be ascribed to the formation of the cationic and dicationic imidoiron complexes, respectively.

Attempts to chemically generate the dicationic adamantylimidoiron species have, thus

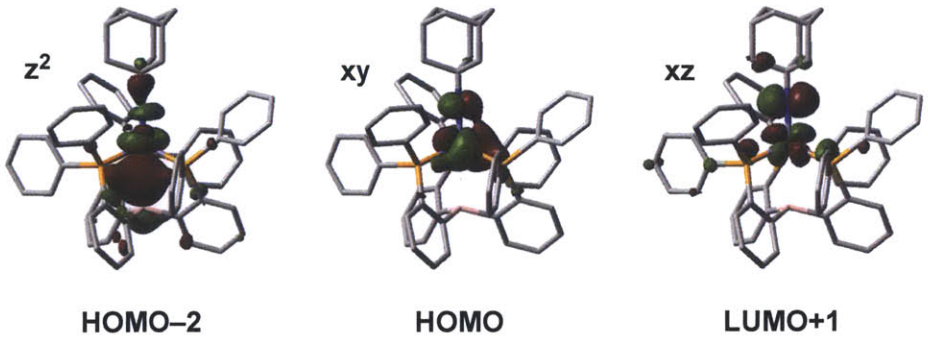

Figure 2.8 Surface plots of the orbitals of d_{z^2} (and Fe–B σ-bonding) parentage (HOMO–2), d_{xy} parentage (HOMO), and d_{xz} parentage (LUMO+1) (DFT, Gaussian 09, M06L, 6-31G(d,p), isovalue = 0.004) for imidoiron **2.4**.

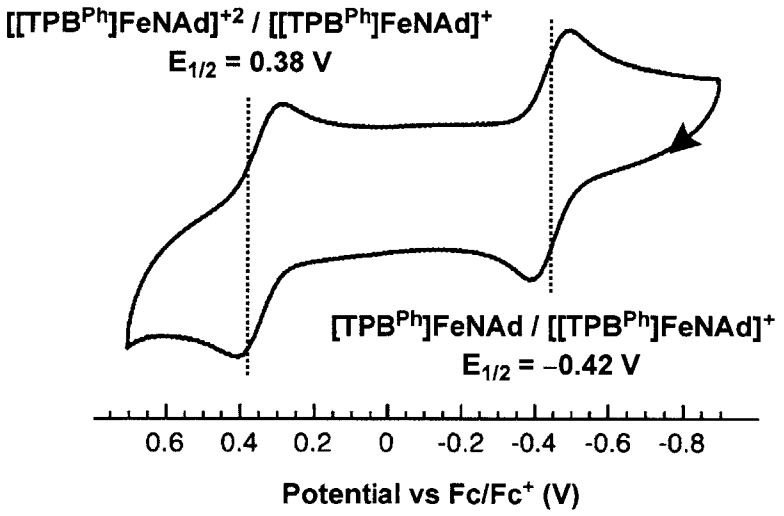

Figure 2.9 Cyclic voltammogram of neutral imidoiron complex **2.4** (0.4 M [^{n}Bu$_4$N][PF$_6$], THF, scan rate = 100 mV/s).

far, been unsuccessful. However, the monocationic complex [[TPB^{Ph}]FeNAd][PF$_6$] ([**2.5**]-[**PF$_6$**]) can be generated in moderate yield via treatment of a THF solution of **2.4** with 1.1 equiv of FcPF$_6$ (Scheme 2.6). Complex [**2.5**][**PF$_6$**] is paramagnetic with broad resonances ranging from 23 to −10 ppm. The Evans method solution magnetic moment measurement (μ_{eff} = 1.8 μ_B, THF-d_8, 25 °C) is slightly higher than the spin-only value of 1.7 μ_B for one unpaired electron and implies an S = 1/2 ground state. Single crystals of [**2.5**][**PF$_6$**] invariably suffered from severe disorder, preventing an unambiguous assignment of the number of counterions associated with the adamantylimidoiron species crystallized. To aid in assignment, the larger [BAr$^F_4$] counterion was employed ([BAr$^F_4$] = tetrakis[3,5-bis(trifluoromethyl)phenyl]borate); treatment of a diethyl ether slurry of [**2.5**][**PF$_6$**] with an excess of NaBAr$^F_4$ yielded [**2.5**][**BAr$^F_4$**] in near quantitative yield.

Gratifyingly, crystals of [**2.5**][**BAr$^F_4$**] do not suffer severe disorder and the identity of [**2.5**][**BAr$^F_4$**] was confirmed by X-ray crystallographic analysis (Figure 2.10). Cationic [**2.5**][**BAr$^F_4$**] crystallizes in the triclinic space group $P\bar{1}$, with one molecule in the asymmetric unit. The core structure is very similar to that of **2.4**: a four-coordinate, pseudotetrahedral iron center ligated by three phosphines and an adamantylimido moiety. Upon oxidation from **2.4** to [**2.5**][**BAr$^F_4$**], the Fe−N−C angle contracts ca. 7° (178.3(1)° vs

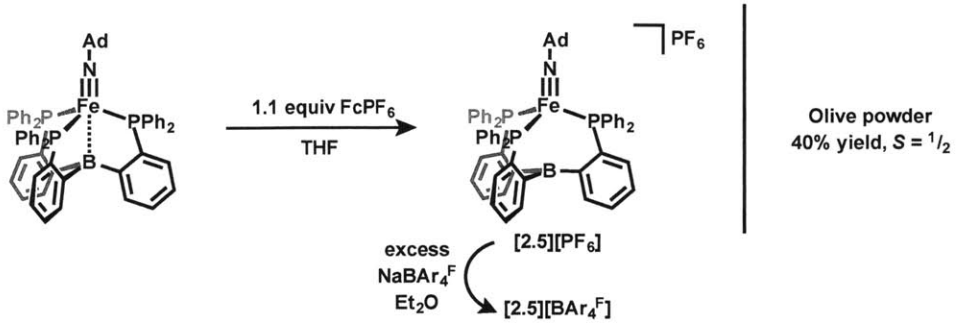

Scheme 2.6 Chemical oxidation of **2.4** to synthesize the cationic, terminal imidoiron species [**2.5**][$\mathbf{PF_6}$]. Subsequent anion exchange generates [**2.5**][$\mathbf{BAr^F_4}$].

171.0(2)°) and the Fe−N distance remains essentially the same (1.6333(2) Å vs 1.6422 Å). Little structural change is expected for the Fe−N−C linkage, as an electron should be removed from a largely nonbonding orbital (Figure 2.7, right). The Fe−B distance is very long in [**2.5**][$\mathbf{BAr^F_4}$] (3.136 Å) and is ca. 0.4 Å longer than that of **2.4**; the sum of the C−B−C angles is 354.2(2)°, indicating near planarity at the boron center. These metrical parameters make [**2.5**][$\mathbf{BAr^F_4}$] quite unique among the [TPB^R]Fe complexes prepared in the Peters group, in that there is unequivocally no interaction between the iron and boron centers.[21,22] The P−Fe−P angles of [**2.5**][$\mathbf{BAr^F_4}$] range from 101.92(1) to 112.70(1)° and their sum is 317.14(2)°, less than that that expected for a regular tetrahedron (328.5°). Interestingly, the average Fe−P bond length increases ca. 0.1 Å upon oxidation. This change is counterintuitive, as the unpaired spin should reside in an orbital of primarily non-bonding character. A similar observation was made for the related [PhBP$^{Ph}_3$]FeNAd and [[PhBP$^{Ph}_3$]FeNAd][^{n}Bu$_4$N] complexes.[13] The phenomenon was rationalized on the basis that the divalent iron center can more strongly π-backbond into the σ-antibonding orbitals of the tripodal ligand than the trivalent iron center by virtue of its d^6 (versus d^5) configuration. This reasoning may also be applied to [**2.5**][$\mathbf{BAr^F_4}$]; consistent with this argument is that the average P−C bonds of **2.4** are ca. 0.02 Å longer than those of [**2.5**][$\mathbf{BAr^F_4}$] (1.84 Å vs 1.82 Å).

The X-band EPR spectrum of [**2.5**][$\mathbf{PF_6}$], recorded in 2-MeTHF at 10 K, is shown in Figure 2.11. The EPR signal is rhombic, with g_1, g_2 and g_3 values of 2.370, 2.085 and 1.975, respectively. The g_{iso} value of 2.143 suggests that the unpaired spin resides

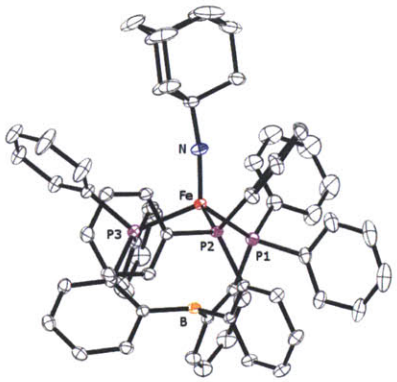

Selected Bond Lengths (Å) and Angles (°)
Fe–N = 1.642(1)
Fe–N–C = 171.0(2)
Fe–P (avg) = 2.2913(4)
∑(P–Fe–P) = 317.14(2)
Fe–B = 3.136
∑(C–B–C) = 354.2(2)

Figure 2.10 Solid-state structure of [**2.5**][$\mathbf{BAr^F_4}$]. Thermal ellipsoids are drawn at 40% probability. Hydrogen atoms, the BAr^F_4 counterion and the minor component of the disordered adamantyl group are omitted for clarity.

in an orbital orthogonal to the Fe−N vector. If the unpaired electron is located in either the $d_{x^2-y^2}$ or d_{xy} orbital (see Figure 2.8 for the relative order of the energy levels), then rotation of one of these d-orbitals moves the unpaired electron into an occupied orbital (i.e., $d_{x^2-y^2} \rightarrow d_{xy}$ and $d_{xy} \rightarrow d_{x^2-y^2}$), leading to a magnetic field that is in concert with the applied field. A smaller applied magnetic field is required and the calculated g value will therefore be greater than that of a free electron ($g = 2.0$).[38] For this discussion, the contribution from the rotation of $d_{x^2-y^2}$ or d_{xy} into the unoccupied d_{xz} or d_{yz} orbitals of cation **2.5** are omitted because they are much higher in energy and the spin-orbit effects between $d_{x^2-y^2}$ and d_{xy} should be dominant. These parameters are similar to the related [BP^R_3]FeNR imidoiron(III) complexes,[10,33] suggesting a similar electronic configuration in which the unpaired electron resides in one of the nonbonding $d_{x^2-y^2}$ and d_{xy} orbitals. The σ- and π-nonbonding character of this singly occupied molecular orbital (SOMO) implies that cation **2.5** should have mostly metalloradical character. A single point energy calculation on **2.5** supports this interpretation, with a Mulliken spin density of 1.54 at the iron center (Figure 2.11, right).

These results are in stark contrast with those obtained for the isoelectronic nitridoiron complex [TPB^{iPr}]FeN prepared by Moret.[39] This species is highly unstable, but can be generated by photolysis of the azidoiron precursor [TPB^{iPr}]FeN_3 in frozen solution and detected by EPR. The X-band EPR spectrum of the nitridoiron species, shown in Figure 2.12,

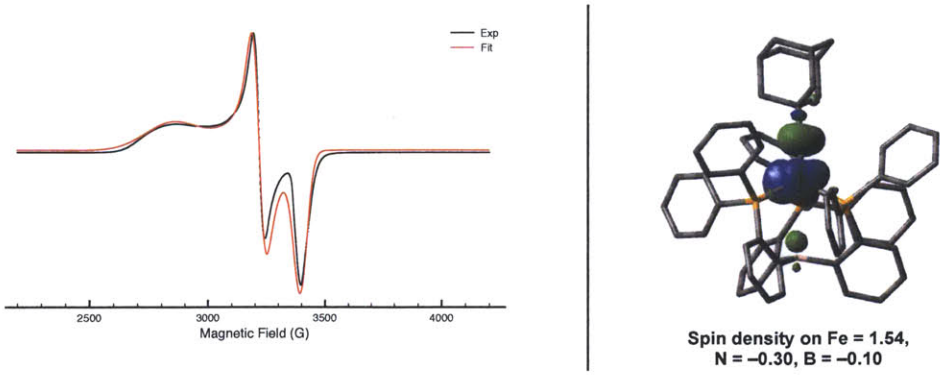

Figure 2.11 (*left*) Experimental (black) and simulated (red) X-band EPR spectrum of [**2.5**][$\mathbf{PF_6}$] (2-MeTHF, 10 K). (*right*) Spin density surface calculated for **2.5** (DFT, Gaussian 09, M06L, 6-311+G(d,p), isovalue = 0.003).

is well simulated as an axial signal (77 K, toluene, $g_{\|} = 1.999$, $g_{\perp} = 2.031$) with hyperfine coupling to N ($A_{\|}$ = 19 MHz), B ($A_{\|}$ = 80 MHz, $A_{\perp}$ = 21.6 MHz) and three P nuclei ($A_{\|}$ = 42.0 MHz, $A_{\perp}$ = 46.5 MHz). These parameters indicate a ground state electronic configuration in which the Fe−N σ-antibonding SOMO is stabilized by delocalization onto the boron atom. The calculated spin density of [TPB$^{i\mathrm{Pr}}$]FeN also indicates significant delocalization onto the boron atom (Figure 2.12, right). The difference in the electronic structures of [**2.5**][$\mathbf{PF_6}$] and [TPB$^{i\mathrm{Pr}}$]FeN likely arises as a result of the lower σ-donor strength of the adamantylimido ligand relative to the nitrido ligand, thereby stabilizing the orbital of d_{z^2} character and rendering it mostly nonbonding.

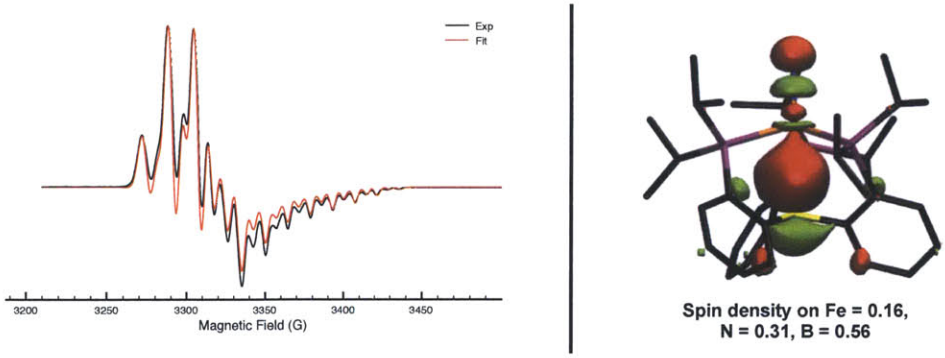

Figure 2.12 (*left*) Experimental (black) and simulated (red) X-band EPR spectrum of [TPB$^{i\mathrm{Pr}}$]FeN (2-MeTHF, 10 K). (*right*) SOMO calculated for [TPB$^{i\mathrm{Pr}}$]FeN (DFT, Gaussian 09, B3LYP, 6-311+G(d,p), isovalue = 0.004).

2.5 Mössbauer Spectroscopic Studies

The Mössbauer spectra of **2.3**, **2.4** and [**2.5**][$\mathbf{BAr^F_4}$] obtained at 5 K and zero applied field are shown in Figure 2.13. Although the isomer shift is often used to identify a particular iron valence state, strong covalency can compress the range of isomer shifts,[40] resulting in an ambiguous assignment of the iron valence. In addition, the local geometry can significantly affect both the isomer shift and the quadrupole splitting parameters.[41–43] Therefore, only the spectra of **2.4** and [**2.5**][$\mathbf{BAr^F_4}$] can be internally compared.

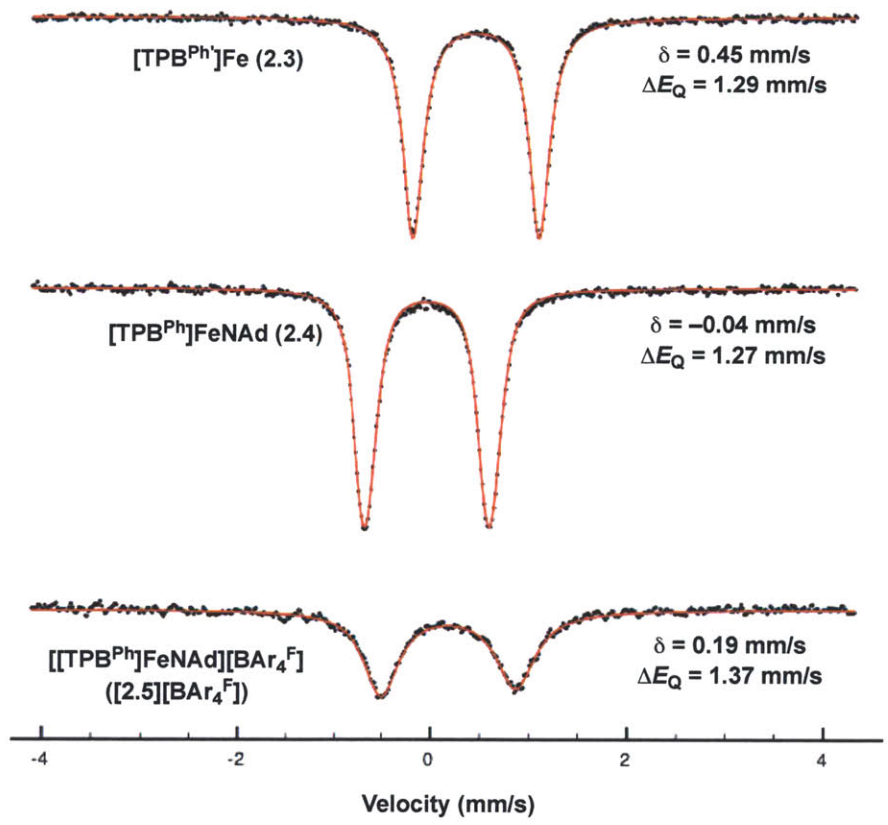

Figure 2.13 (*top*) Experimental (black) and simulated (red) Mössbauer spectrum of **2.3**. (*center*) Experimental (black) and simulated Mössbauer spectrum of **2.4**. (*bottom*) Experimental (black) and simulated (red) Mössbauer spectrum of [**2.5**][$\mathbf{BAr^F_4}$]. All spectra were collected at 5 K and zero applied field.

The spectrum of **2.3** consists of a quadrupole doublet centered at δ = 0.45 mm/s, with a quadrupole splitting of ΔE_Q = 1.29 mm/s. The line widths are slightly asymmetric, with

γ_L = 0.26 mm/s and γ_R = 0.25 mm/s (Figure 2.13, top). The spectrum of **2.4** features a quadrupole doublet centered at δ = −0.04 mm/s, with a quadrupole splitting of ΔE_Q = 1.27 mm/s (Figure 2.13, center). Finally, the spectrum of [**2.5**][$\mathbf{BAr^F_4}$] shows a quadrupole doublet centered at δ = 0.19 mm/s, with a quadrupole splitting of ΔE_Q = 1.37 mm/s. This spectrum is significantly broader and more asymmetric than the other two, with γ_L = 0.44 mm/s and γ_R = 0.48 mm/s (Figure 2.13, bottom). The Mössbauer spectrum of [**2.5**][$\mathbf{BAr^F_4}$] measured in an externally applied field (54 mT) is identical to that obtained in zero applied field. The isomer shifts of **2.4** and [**2.5**][$\mathbf{BAr^F_4}$] (−0.04 mm/s vs 0.19 mm/s) shift positive as the overall formal oxidation state of iron increases from iron(II) to iron(III). This trend mirrors the decrease in s-electron density at iron upon removal of electrons from the system. The isomer shift of **2.3** is much more positive than the other two complexes (0.45 mm/s), however the geometry of this complex is very different from the imido complexes and so the significance of this isomer shift cannot be discussed without first obtaining Mössbauer spectra of similar complexes for comparison.

2.6 Conclusions and Future Work

In this chapter, the preparation and characterization of a series of iron tris(phosphine)borane complexes were described. In contrast to the related [TPB^{iPr}]FeBr complex, reduction of [TPB^{Ph}]FeCl yields a one-electron reduced species featuring an η^6-arene interaction, as a result of dechelation of a phosphine arm. This structural motif is maintained in both the solid and solution states. The one-electron reduced species serves as a well-defined material for further transformations, most notably for the decomposition of adamantylazide to yield a terminal imidoiron complex. Interestingly, this imidoiron complex can be oxidized to yield the cationic imidoiron species in which there is no interaction between the iron and boron centers. This species has a different ground electronic state than the isoelectronic [TPB^{iPr}]FeN complex, thereby showcasing the ability of the tris(phosphine)borane ligand to stabilize various electronic structures by an axial delocalization of electrons onto the boron center.

Qualitative inspection of the molecular orbital diagram in Figure 2.7 suggests that the

dicationic imidoiron species can be generated; this is supported by electrochemical studies of [TPB^{Ph}]FeNAd (Figure 2.9). The isolation of such a dicationic species would be of interest in relation to the tris(phosphine)borate imidoiron chemistry reported by the Peters group and the tris(carbene)borate imidoiron chemistry described by the Smith group. To our knowledge, the addition of the dicationic species would provide the first example of a pseudotetrahedral imidoiron complex in three different oxidation states.

Although the Peters group has begun study of catalytic reactions mediated by the related [TPB^{iPr}]FeN_2 complex, one could envision that even if a phosphine arm dechelates during a catalytic process, the steric bulk of the ligand may slow or even preclude catalysis and make the system less amenable to various larger substrates of interest (e.g. a 1,2-disubstituted olefin in the case of hydrogenation catalysis). Complex [$TPB^{Ph'}$]Fe would be an ideal candidate for catalytic studies, as the η^6-arene interaction is a stable, yet labile, configuration. In addition, dechelation of one of the phosphine arms has already occurred in [$TPB^{Ph'}$]Fe, thereby relieving some of the steric strain of the system and potentially providing a large substrate other approaches to the iron center.

2.7 Experimental Methods

2.7.1 General Considerations

All manipulations were carried out using standard Schlenk or glovebox techniques under a dinitrogen atmosphere. Unless otherwise noted, solvents were dried and deoxygenated by sparging with argon and passing through activated alumina in a solvent purification system from SG Waters USA, LLC (Nashua, NH). Non-halogenated solvents were tested with a standard purple solution of sodium benzophenone ketyl in tetrahydrofuran in order to confirm effective oxygen and moisture removal. *o*-$Ph_2(C_6H_4)Br$[44] and $NaBAr^F_4$[45] (BAr^F_4 = tetrakis[3,5-bis(trifluoromethyl)phenyl]borate) were prepared according to literature methods. All other reagents were purchased from commercial suppliers and used without further purification. Elemental analyses were performed by Midwest Microlab, LLC (Indianapolis, IN) and Robertson Microlit Laboratories, Inc (Ledgewood, NJ). Deuterated solvents were

purchased from Cambridge Isotope Laboratories, Inc., degassed, and dried over activated 3-Å molecular sieves prior to use.

2.7.2 Spectroscopic Measurements

Varian 300, 400 and 500 MHz spectrometers were used to record ^{1}H, ^{13}C, ^{31}P and ^{11}B NMR spectra at room temperature, unless otherwise noted. ^{1}H and ^{13}C NMR chemical shifts were referenced to the residual solvent peaks. ^{31}P NMR chemical shifts were referenced to external 85% phosphoric acid (δ = 0 ppm). ^{11}B NMR chemical shifts were referenced to external $BF_3 \cdot Et_2O$ (δ = 0 ppm). Solution magnetic moment measurements were determined by the method of Evans.[46,47] To determine the error in these measurements, an error analysis was performed and the error bars were established at 95% confidence using regression analysis. The values are reported to two significant figures and are understood to have an error of $\pm$ 0.1 μB. Optical spectroscopy measurements were taken on a Cary 50 UV-vis spectrophotometer using a 1 cm two-window quartz cell sealed with a closed cap (Starna Cells, Inc, Altascadero, CA). Infrared measurements were obtained in thin films using a Bruker ALPHA FT-IR spectrometer equipped with a diamond ATR probe and OPUS/Mentor software. X-band EPR spectra were recorded using a Bruker EMX spectrometer at 77 K in 2-MeTHF glasses. EPR samples were prepared in a glovebox under an N_2 atmosphere in quartz EPR tubes equipped with J. Young caps. EPR spectra were simulated using EasySpin.[48] ^{57}Fe Mössbauer spectra were measured with a constant acceleration spectrometer (SEE Co., Minneapolis, MN). Isomer shifts are quoted relative to Fe metal at room temperature. Data were analyzed and simulated with WMOSS software (Web Research Corp., Edina, MN).

2.7.3 Electrochemistry

Electrochemical measurements were carried out in a glovebox under a dinitrogen atmosphere in a one-compartment cell using a CH Instruments 630-C Electrochemistry Analyzer with CHI Version 8.09 software package. A glassy carbon electrode and platinum wire were used as the working and auxiliary electrodes, respectively. The reference elec-

trode was $Ag/AgNO_3$ in THF. Solutions of electrolyte (0.4 M $[^nBu_4N][PF_6]$) and analyte were prepared in a glovebox. Experiments were conducted at room temperature. The ferrocene couple Fc/Fc^+ was used as an external reference.

2.7.4 DFT Calculations

Calculations for **2.4** and **2.5** were performed using the Gaussian09 suite of programs.[49] Single point calculations were performed with the M06L functional[50] and the 6-31G(d) basis set for all atoms of **2.4** and 6-311+G(d,p) basis set for all atoms of **2.5**. The Mulliken spin densities calculated for **2.5** are summarized in Table 2.2.

Atom	Value	Atom	Value
Fe	1.537288	P	−0.041476
N	−0.296205	P	−0.061982
B	−0.105632	P	−0.045213

Table 2.2 Mulliken spin densities calculated for **2.5**. For clarity, only the values for the heteroatoms are shown.

2.7.5 Preparation of $[TPB^{Ph}]$ (2.1)

The ligand was prepared by modification of the recently reported literature procedure.[28] ^{n}BuLi (13.5 mL, 1.6 M in hexane, 21.60 mmol) was added to a solution of o-$Ph_2(C_6H_4)Br$ (7.38 g, 21.60 mmol) in OEt_2 (100 mL) at −78 °C. The slurry was stirred for 10 min, then warmed to room temperature and stirred for 1.5 h, yielding a light yellow slurry. The volatiles were removed in vacuo, the residual solids dissolved in toluene and the solution recooled to −78 °C. BCl_3 was added (7.2 mL, 1 M in heptane, 7.2 mmol), resulting in a slightly darker yellow mixture. The reaction mixture was slowly warmed to room temperature (12 h). The volatiles were removed in vacuo and the residue triturated with pentane. The residual solids were then slurried in CH_2Cl_2 and filtered through Celite. The filtrate was concentrated to ca. 50% of its original volume and pentane was added. The resulting white precipitate was collected and washed with pentane (5.16 g, 90%). The ^1H and $^{31}P\{^1H\}$ NMR spectra match those previously reported in the literature.

2.7.6 Preparation of [TPB^{Ph}]FeCl (2.2)

A Schlenk tube was charged with **2.2** (922.8 mg, 1.24 mmol), $FeCl_2$ (197.9 mg, 1.56 mmol), iron powder (176.4 mg, 3.16 mmol) and THF (50 mL). The reaction was stirred vigorously for 3 d at 70 °C, during which time the slurry turned dark brown. The mixture was filtered through Celite to remove the excess iron powder and the volatiles removed in vacuo. The residual solids were triturated with toluene, slurried in CH_2Cl_2 and filtered to collect a dark brown powder (841.2 mg, 76%). Crystals suitable for X-ray analysis were grown by slow evaporation of a C_6H_6 solution. ^{1}H NMR (300 MHz, THF-d_8) δ 34.23, 23.91, 9.89, 7.30, 4.73, 2.31, −23.84. μ_{eff} (THF-d_8, Evans method, 25 °C): 4.0 μB. Anal. Calcd for $C_{54}H_{42}BClFeP_3$: C, 73.21; H, 4.78. Found: C, 72.96; H, 4.62.

2.7.7 Preparation of [TPB$^{Ph'}$]Fe (2.3)

Sodium (3.4 mg, 0.15 mmol) and mercury (500 mg) were stirred vigorously with C_6H_6 (1 mL). A slurry of **2.2** (95.1 mg, 0.11 mmol) in C_6H_6 (10 mL) was added and the reaction mixture stirred for 6 h at room temperature. The resulting dark red mixture was filtered and lyophilized (80.5 mg, 88%). Crystals suitable for X-ray analysis were grown by vapor diffusion of OEt_2 into a concentrated THF solution at −35 °C. ^{1}H NMR (400 MHz, C_6D_6) δ 8.38 (t, J = 8.4 Hz, 2H), 7.94 (d, J = 7.4 Hz, 1H), 7.85 (t, J = 7.3 Hz, 2H), 7.59 (ddt, J = 9.6, 7.3, 3.1 Hz, 4H), 7.41 (d, J = 7.5 Hz, 1H), 7.31 – 7.17 (m, 6H), 7.09 – 6.79 (m, 12H), 6.73 (dd, J = 4.4, 2.6 Hz, 3H), 6.60 (t, J = 8.6 Hz, 2H), 6.54 – 6.42 (m, 2H), 6.33 – 6.15 (m, 2H), 6.04 (t, J = 5.9 Hz, 1H), 4.42 (q, J = 6.7 Hz, 1H), 4.16 (q, J = 5.6 Hz, 1H), 3.89 (d, J = 6.1 Hz, 1H), 3.62 (q, J = 6.6 Hz, 1H). ^{13}C$\{^1$H$\}$ NMR (126 MHz, C_6D_6) δ 160.5 (s), 145.7 (d, J = 7.0 Hz), 144.1 (s), 143.8 (s), 142.9 (s), 142.5 (s), 141.9 (s), 141.5 (s), 140.9 (s), 140.6 (s), 139.8 (s), 139.7 (s), 137.7 (s), 137.4 (s), 136.0 (d, J = 10.8 Hz), 135.6 (s), 135.2 (m), 134.8 (s), 134.6 (s), 132.9 (m), 132.3 (d, J = 8.7 Hz), 132.0 (d, J = 7.3 Hz), 130.9 (m), 129.2 (s), 129.0 (s), 128.7 (s), 126.9 (m), 126.3 (d, J = 8.7 Hz), 125.9 (s), 124.3 (s), 123.8 (d, J = 6.6 Hz), 123.6 (d, J = 6.5 Hz), 109.2 (d, J = 15.7 Hz), 94.0 (d, J = 14.3 Hz), 88.6 (s), 87.0 (s), 85.8 (s), 85.5 (m). ^{31}P$\{^1$H$\}$ NMR (121 MHz, C_6D_6) δ 86.1 (d, J = 81.8 Hz), 69.8 (d, J = 82.2 Hz), −12.1 (s). ^{11}B$\{^1$H$\}$ NMR (128 MHz, C_6D_6) δ 15.9.

Anal. Calcd for $C_{54}H_{42}BFeP_3$: C, 76.26; H, 4.98. Found: C, 76.69; H, 5.59.

2.7.8 Preparation of [TPB^{Ph}]Fe(NAd) (2.4)

A mixture of **2.3** (142.6 mg, 0.17 mmol) and N_3Ad (32.4 mg, 0.18 mmol) in C_6H_6 (10 mL) were stirred at room temperature. The red solution turned dark green over the course of 30 min. The reaction was stirred for 6 h, frozen and lyophilized. Pentane was added and the slurry mixed vigorously for 30 min before filtering to remove a light yellow filtrate. The green solids were redissolved in C_6H_6, filtered and lyophilized (116.3 mg, 68%). Crystals suitable for X-ray analysis were grown by vapor diffusion of OEt_2 into a concentrated THF solution. ^{1}H NMR (500 MHz, toluene-d_8) δ 7.82 (t, J = 7.0 Hz, 6H), 7.54 (d, J = 7.3 Hz, 3H), 7.15 (s, 9H), 7.09 – 6.95 (m, 12H), 6.70 (d, J = 7.5 Hz, 12H), 2.17 (d, J = 10.8 Hz, 3H), 1.77 (s, 3H), 1.65 (d, J = 10.5 Hz, 3H), 1.53 (s, 6H). $^{13}C\{^1H\}$ NMR (126 MHz, toluene-d_8) δ 160.3, 145.4, 145.1, 141.1, 140.8, 140.2, 140.0, 136.1, 132.5, 129.9, 127.2, 126.6, 126.4, 72.3, 37.9, 34.0, 28.7, 25.4. $^{31}P\{^1H\}$ NMR (121 MHz, C_6D_6) δ 96.0 (s). $^{11}B\{^1H\}$ NMR (128 MHz, C_6D_6, 45 °C) δ 39.5. UV-vis (ε, C_6H_6, nm cm^{-1}M^{-1}): 625 {460}, 875 {4}. Anal. Calcd for $C_{64}H_{57}BFeNP_3$: C, 76.89; H, 5.75; N, 1.40. Found: C, 76.68; H, 5.99; N, 1.35.

2.7.9 Preparation of [[TPB^{Ph}]Fe(NAd)][PF$_6$] ([2.5][PF$_6$])

A mixture of **2.4** (80.7 mg, 0.79 mmol) and $FcPF_6$ (28.8 mg, 0.87 mmol) in THF (10 mL) were stirred at room temperature for 2 h, during which time the reaction changed color from dark green to brown. The solution was concentrated and OEt_2 added to precipitate a brown powder. The mixture was stirred vigorously for 30 min and filtered to remove a light brown filtrate. The solids were washed with C_6H_6, then dissolved in THF and filtered to yield a greenish-brown solution. The volatiles were removed in vacuo and the residual solids triturated with OEt_2 to yield a greenish-brown powder (36.9 mg, 40%). ^{1}H NMR (500 MHz, THF-d_8) δ 22.68, 16.18, 11.49, 10.47, 9.47, 9.15, 8.94, 7.43, 7.08, 6.55, 6.22, 5.56, 3.46, 3.28, 3.16, 3.06, −9.80. μ_{eff} (THF-d_8, Evans method, 25 °C): 1.8 μB. Anal. Calcd for $C_{64}H_{57}BF_6FeNP_4 \cdot (THF)_2$: C, 67.09; H, 5.71; N, 1.09. Found: C, 66.48; H, 5.30;

N, 1.02. Crystals suitable for X-ray analysis were grown by vapor diffusion of pentane into a concentrated THF solution. These crystals invariably suffered from severe disorder that prevented an unambiguous assignment of the charge of the imidoiron moiety in the crystal by charge balance as well as the assignment of any solvent molecules. Thus, the larger counteranion tetrakis[3,5-bis(trifluoromethyl)phenyl]borate ($[BAr^F_4]^-$) was employed for X-ray structure determination.

2.7.10 Preparation of [[TPB^{Ph}]Fe(NAd)][BAr$^F_4$] ([2.5][BAr$^F_4$])

To a OEt_2 slurry (10 mL) of [**2.5**][$\mathbf{PF_6}$] (80.0 mg, 73.89 μmol) was added a OEt_2 solution of $NaBAr^F_4$ (98.0 mg, 110.6 μmol) at room temperature. After 2 h, the reaction mixture was filtered through Celite and the solvent removed in vacuo to yield a brown microcrystalline material (130.6 mg, 95%). X-ray quality crystals were grown by vapor diffusion of CH_2Cl_2 into a concentrated OEt_2 solution. ^{1}H NMR (300 MHz, THF-d_8) δ 20.76, 14.02, 9.31, 8.31, 7.81, 7.59, 6.98, 6.81, 5.19, 5.00, 4.50, 4.10, 1.64, −11.81. μ_{eff} (THF-d_8, Evans method, 25 °C): 2.1 μB. Anal. Calcd for $C_{96}H_{69}B_2F_{24}FeNP_3 \cdot 2\,CH_2Cl_2$: C, 57.90; H, 3.62; N, 0.69. Found: C, 58.37; H, 3.62; N, 0.62.

2.7.11 X-ray Crystallographic Details

Single crystals of **2.2** were obtained by slow evaporation of a C_6H_6 solution, crystals of **2.3** were grown by vapor diffusion of OEt_2 into a concentrated THF solution at −35 °C, crystals of **2.4** were obtained by vapor diffusion of OEt_2 into a concentrated THF solution, crystals of [**2.5**][$\mathbf{BAr^F_4}$] were grown by by vapor diffusion of CH_2Cl_2 into a concentrated OEt_2 solution. Low-temperature single crystal X-ray diffraction studies were carried out at the Beckman Institute Crystallography Facility on a Bruker Kappa Apex II diffractometer with Mo Kα radiation (λ = 0.71073 Å). Crystals were coated with Paratone-N oil and mounted on glass fibers. Structures were solved by direct or Patterson methods using SHELXS[51] and refined against F2 on all data by full-matrix least squares with SHELXL-97[52] using established refinement techniques.[53] All non-hydrogen atoms were refined anisotropically. All hydrogen atoms were included into the model at geometrically calculated positions

and refined using a riding model. The isotropic displacement parameters of all calculated hydrogen atoms were fixed to 1.2 times the U values of the atoms they are linked to (1.5 times for methyl groups). Thermal ellipsoid diagrams were created using Olex2.[54] In the structure of [**2.5**][$\mathbf{BAr_4^F}$], the adamantyl group and the CF_3 groups of C89, C88 and C71 were disordered over two sites. The structures of **2.3**, **2.4** and [**2.5**][$\mathbf{BAr_4^F}$] contained voids with disordered solvent molecules. The program SQUEEZE[55] as implemented in Platon[56] was used to remove the contribution of the disordered solvent to the structure factors. The crystallographic details for **2.2** – [**2.5**][$\mathbf{BAr_4^F}$] are summarized in Tables 2.3 and 2.4.

	2.2	**2.3** · THF
Formula	$C_{54}H_{42}BClFeP_3$	$C_{59}H_{52.50}BFeO_{1.25}P_3$
Formula Weight	885.90	941.08
Temperature/K	100(2)	100(2)
Crystal syst.	Monoclinic	Orthorhombic
Space group	$P2_1/c$	$P2_12_12_1$
Color	Brown	Red
a/Å	12.9941(8)	10.8211(6)
b/Å	17.1371(11)	18.6466(12)
c/Å	19.5570(11)	23.1518(13)
α/°	90	90
β/°	98.255(3)	90
γ/°	90	90
V/^{3}	4309.9(5)	4671.5(5)
ρ (calc.)/(gcm^{-1})	1.365	1.338
Z	4	4
No. refl.	92375	61463
No. unique refl.	16422	15131
R_{int}	0.0535	0.0520
R_1 (all data)[a]	0.0643	0.0695
wR_2 (all data)[b]	0.1063	0.1225
R_1 [(I >2σ)]	0.0408	0.0511
wR_2 [(I >2σ)]	0.0956	0.1160
GOF[c]	1.011	1.019

Table 2.3 Crystallographic summary for **2.2** and **2.3**. [a]$R_1 = \Sigma||F_0 - |F_e||/\Sigma|F_0|$. [b]$wR_2 = (\Sigma[w(F_0^2 - F_e^2)^2]/\Sigma[w(F_0^2)^2])^{1/2}$. [c]$GOF = (\Sigma[w(F_0^2 - F_e^2)^2]/(n-p))^{1/2}$ where n is the number of data and p is the number of parameters refined.

	2.4	**[2.5][BAr^F_4]**
Formula	$C_{71.50}H_{75.75}BFeNO_{1.88}P_3$	$C_{98}H_{74}B_2F_{24}FeNO_{0.5}P_3$
Formula Weight	1138.65	1899.96
Temperature/K	100(2)	100(2)
Crystal syst.	Monoclinic	Triclinic
Space group	$C2/c$	$P\bar{1}$
Color	Green	Brown
a/Å	28.412(2)	13.0465(6)
b/Å	24.6270(19)	16.8546(8)
c/Å	19.3403(14)	20.9305(10)
α/°	90	89.516(3)
β/°	115.820(4)	74.763(3)
γ/°	90	87.214(3)
V/^{3}	12181.3(16)	4435.4(4)
ρ (calc.)/(gcm^{-1})	1.242	1.423
Z	8	2
No. refl.	83995	240059
No. unique refl.	14529	40635
R_{int}	0.0656	0.0462
R_1 (all data)[a]	0.0780	0.0752
wR_2 (all data)[b]	0.1179	0.1491
R_1 [(I >2σ)]	0.0463	0.0528
wR_2 [(I >2σ)]	0.1087	0.1382
GOF[c]	0.982	1.084

Table 2.4 Crystallographic summary for **2.4** and **[2.5][BAr^F_4]**. [a]$R_1 = \Sigma||F_0 - |F_e||/\Sigma|F_0|$. [b]$wR_2 = (\Sigma[w(F_0^2 - F_e^2)^2]/\Sigma[w(F_0^2)^2])^{1/2}$. [c]$GOF = (\Sigma[w(F_0^2 - F_e^2)^2]/(n-p))^{1/2}$ where n is the number of data and p is the number of parameters refined.

2.8 Bibliography

[1] Luthra, A.; Denisov, I. G.; Sligar, S. G. *Arch. Biochem. Biophys.* **2011**, *507*, 26–35.

[2] Kurtz, D. M., Jr. *J. Inorg. Biochem.* **2006**, *100*, 679–693.

[3] Britt, R. D.; Campbell, K. A.; Peloquin, J. M.; Gilchrist, M. L.; Aznar, C. P.; Dicus, M. M.; Robblee, J.; Messinger, J. *Biochim. Biophys. Acta* **2004**, *1655*, 158–171.

[4] Dey, S.; Das, P. K.; Dey, A. *Coord. Chem. Rev.* **2013**, *257*, 42–63.

[5] Lyaskovskyy, V.; de Bruin, B. *ACS Catal.* **2012**, *2*, 270–279.

[6] Arifin, K.; Majlan, E. H.; Daud, W. R. W.; Kassim, M. B. *Int. J. Hydrogen Energy* **2012**, *37*, 3066–3087.

[7] Sankar, M.; Dimitratos, N.; Miedziak, P. J.; Wells, P. P.; Kiely, C. J.; Hutchings, G. J. *Chem. Soc. Rev.* **2012**, *41*, 8099–8139.

[8] Weller, A. S.; McIndoe, J. S. *Eur. J. Inorg. Chem.* **2007**, *2007*, 4411–4423.

[9] Dempsey, J. L.; Esswein, A. J.; Manke, D. R.; Rosenthal, J.; Soper, J. D.; Nocera, D. G. *Inorg. Chem.* **2005**, *44*, 6879–6892.

[10] Brown, S. D.; Betley, T. A.; Peters, J. C. *J. Am. Chem. Soc.* **2003**, *125*, 322–323.

[11] Betley, T. A.; Peters, J. C. *Inorg. Chem.* **2003**, *42*, 5074–5084.

[12] Mankad, N. P.; Whited, M. T.; Peters, J. C. *Angew. Chem. Int. Ed.* **2007**, *46*, 5768–5771.

[13] Brown, S. D.; Peters, J. C. *J. Am. Chem. Soc.* **2005**, *127*, 1913–1923.

[14] Betley, T. A.; Peters, J. C. *J. Am. Chem. Soc.* **2004**, *126*, 6252–6254.

[15] Betley, T. A.; Peters, J. C. *J. Am. Chem. Soc.* **2003**, *125*, 10782–10783.

[16] Lee, Y.; Mankad, N. P.; Peters, J. C. *Nat. Chem.* **2010**, *2*, 558–565.

[17] Mankad, N. P.; Müller, P.; Peters, J. C. *J. Am. Chem. Soc.* **2010**, *132*, 4083–4085.

[18] MacBeth, C. E.; Harkins, S. B.; Peters, J. C. *Can. J. Chem.* **2005**, *83*, 332–340.

[19] Di Vaira, M.; Ghilardi, C. A.; Sacconi, L. *Inorg. Chem.* **1976**, *15*, 1555–1561.

[20] Vogel, C.; Heinemann, F. W.; Sutter, J.; Anthon, C.; Meyer, K. *Angew. Chem. Int. Ed.* **2008**, *47*, 2681–2684.

[21] Moret, M.-E.; Peters, J. C. *J. Am. Chem. Soc.* **2011**, *133*, 18118–18121.

[22] Moret, M.-E.; Peters, J. C. *Angew. Chem. Int. Ed.* **2011**, *50*, 2063–2067.

[23] Bontemps, S.; Bouhadir, G.; Dyer, P. W.; Miqueu, K.; Bourissou, D. *Inorg. Chem.* **2007**, *46*, 5149–5151.

[24] Brown, N. M. D.; Davidson, F.; Wilson, J. W. *J. Organomet. Chem.* **1981**, *209*, 1–11.

[25] Brown, H. C.; Racherla, U. S. *J. Org. Chem.* **1986**, *51*, 427–432.

[26] Welch, G. C.; Holtrichter-Roessmann, T.; Stephan, D. W. *Inorg. Chem.* **2008**, *47*, 1904–1906.

[27] Jacobsen, H.; Berke, H.; Döring, S.; Kehr, G.; Erker, G.; Fröhlich, R.; Meyer, O. *Organometallics* **1999**, *18*, 1724–1735.

[28] Kameo, H.; Hashimoto, Y.; Nakazawa, H. *Organometallics* **2012**, *31*, 3155–3162.

[29] Addison, A. W.; Rao, T. N.; Reedijk, J.; van Rijn, J.; Verschoor, G. C. *J. Chem. Soc., Dalton Trans.* **1984**, 1349–1356.

[30] Sircoglou, M.; Bontemps, S.; Bouhadir, G.; Saffon, N.; Miqueu, K.; Gu, W.; Mercy, M.; Chen, C.-H.; Foxman, B. M.; Maron, L.; Ozerov, O. V.; Bourissou, D. *J. Am. Chem. Soc.* **2008**, *130*, 16729–16738.

[31] Whited, M. T.; Mankad, N. P.; Lee, Y.; Oblad, P. F.; Peters, J. C. *Inorg. Chem.* **2009**, *48*, 2507–2517.

[32] Verma, A. K.; Nazif, T. N.; Achim, C.; Lee, S. C. *J. Am. Chem. Soc.* **2000**, *122*, 11013–11014.

[33] Thomas, C. M.; Mankad, N. P.; Peters, J. C. *J. Am. Chem. Soc.* **2006**, *128*, 4956–4957.

[34] Mehn, M. P.; Brown, S. D.; Jenkins, D. M.; Peters, J. C.; Que, L., Jr. *Inorg. Chem.* **2006**, *45*, 7417–7427.

[35] Lu, C. C.; Saouma, C. T.; Day, M. W.; Peters, J. C. *J. Am. Chem. Soc.* **2007**, *129*, 4–5.

[36] Nieto, I.; Ding, F.; Bontchev, R. P.; Wang, H.; Smith, J. M. *J. Am. Chem. Soc.* **2008**, *130*, 2716–2717.

[37] Scepaniak, J. J.; Young, J. A.; Bontchev, R. P.; Smith, J. M. *Angew. Chem. Int. Ed.* **2009**, *48*, 3158–3160.

[38] Palmer, G. In *Physical Methods in Bioinorganic Chemistry*; Que, L., Jr., Ed.; University Science Books: Sausalito, CA, pp 121–185.

[39] Moret, M.-E.; MacMillan, S. N.; Peters, J. C. *Manuscript in Preparation.*

[40] Lee, Y.; Peters, J. C. *J. Am. Chem. Soc.* **2011**, *133*, 4438–4446.

[41] Sosinsky, B. A.; Norem, N.; Shong, R. G. *Inorg. Chem.* **1982**, *21*, 4229–4233.

[42] Pribula, C. D.; Brown, T. L.; Münck, E. *J. Am. Chem. Soc.* **1974**, *96*, 4149–4154.

[43] Clark, M. G.; Cullen, W. R.; Garrod, R. E. B.; Maddock, A. G.; Sams, J. R. *Inorg. Chem.* **1973**, *12*, 1045–1051.

[44] Whited, M. T.; Rivard, E.; Peters, J. C. *Chem. Commun.* **2006**, 1613–1615.

[45] Peters, J. C.; Thomas, J. C. *Inorg. Synth.* **2004**, *34*, 8–14.

[46] Sur, S. K. *J. Magn. Reson.* **1989**, *82*, 169–173.

[47] Evans, D. F. *J. Chem. Soc.* **1959**, 2003–2005.

[48] Stoll, S.; Schweiger, A. *J. Magn. Reson.* **2006**, *178*, 42–55.

[49] Frisch, M. J. et al. Gaussian 09, Revision B.01. Gaussian, Inc., Wallingford, CT, 2010.

[50] Zhao, Y.; Truhlar, D. G. *Theor. Chem. Acc.* **2008**, *120*, 215–241.

[51] Sheldrick, G. M. *Acta Cryst.* **1990**, *A46*, 467–473.

[52] Sheldrick, G. M. SHELXL-97: Program for Crystal Structure Refinement. University of Göttingen, Göttingen, Germany, 1997.

[53] Müller, P. *Crystallogr. Rev.* **2009**, *15*, 57–83.

[54] Dolomanov, O. V.; Bourhis, L. J.; Gildea, R. J.; Howard, J. A. K.; Puschmann, H. *J. Appl. Cryst.* **2009**, *42*, 339–341.

[55] van der Sluis, P.; Spek, A. L. *Acta Cryst.* **1990**, *A46*, 194–201.

[56] Spek, A. L. *Acta Cryst.* **2009**, *D65*, 148–155.

3 Si-H Bond Activation by a Bifunctional Nickel-Borane System

Contents

3.1 Introduction and Motivation

The metal-mediated activation of E−H bonds constitutes a fundamental step in a number of transition metal catalyzed transformations.[1] In particular, the activation of Si−H bonds finds broad application in organic synthesis and is a key component of olefin hydrosilylation, dehydrogenative silylation and silane dehydrocoupling processes.[2–4] Hydrosilylation provides a direct and efficient strategy for the functionalization of organic substrates to produce industrially important organosilicon compounds.[5] In such a process, the oxidative addition of the Si−H bond to the metal center is invoked as one of the first steps of the catalytic cycle. For example, olefin hydrosilylation may proceed by the Chalk-Harrod mechanism,[6–8] in which Si−H bond activation occurs to form a silyl hydride complex (Scheme 3.1, left). Subsequent olefin insertion into the M−H (Chalk-Harrod) or M−Si bond (modified Chalk-Harrod),[7,9,10] followed by reductive elimination yields the final reaction product. In the Glaser-Tilley mechanism,[11–14] a silylene hydride complex is formed by double Si−H bond activation (Scheme 3.1, right). Direct addition of the olefin to the Si−H bond of the silylene fragment and metal-to-silicon hydride transfer forms a silyl hydride species. Finally, reductive elimination yields the organic product. The Chalk-Harrod and modified Chalk-Harrod mechanisms are invoked for many transition-metal catalysts; the Glaser-Tilley mechanism, however, is specific to ruthenium-mediated hydrosilylation processes.

Although Si−H bond activation is well known for metals of the nickel triad,[15–29] there

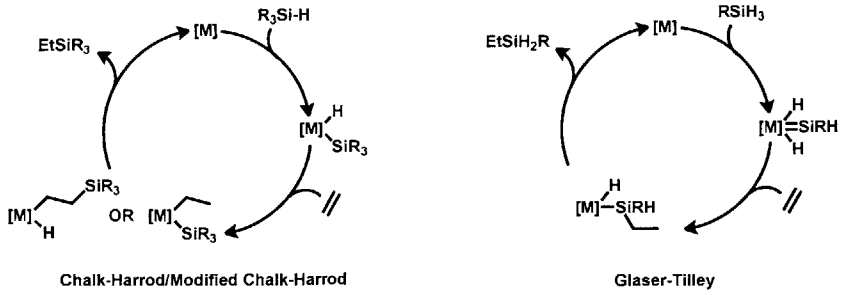

Scheme 3.1 (*left*) Chalk-Harrod and modified Chalk-Harrod mechanisms and (*right*) Glaser-Tilley mechanism for the hydrosilylation of olefins.

is far less knowledge about nickel silyl and nickel silyl hydride species in comparison to their platinum counterparts due to their instability and high reactivity.[15] The use of bulky or chelating ligands has allowed for the isolation of a number of mononuclear nickel silyl[16,30–33] and nickel silane complexes.[30,34–36] However, well-characterized mononuclear nickel silyl hydride complexes, which are the expected products of Si–H bond oxidation addition at nickel, are rare.[35,37,38] Fischer reported the isolation and crystal structure of the unusual nickel silyl hydride species $Ni(AlCp^*)_3(H)(SiEt_3)$ ($Cp^* = \eta^5$-C_5Me_5) supported by pentamethylcyclopentadienyl aluminum(I) ligands (Figure 3.1, left).[38] Subsequently, Radius employed the N-heterocyclic carbene (NHC) ligand ^{i}PrIm (^{i}PrIm = 1,3-di-isopropyl-imidazolin-2-ylidene) to stabilize four-coordinate nickel silyl hydride complexes of the form $(^iPrIm)_2Ni(H)(SiRPh_2)$ (R = Me or Ph, Figure 3.1, right).[37]

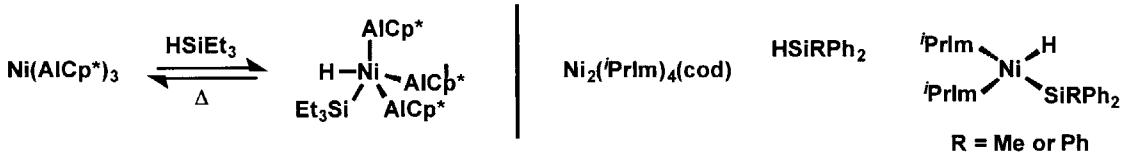

Figure 3.1 Structurally characterized nickel silyl hydride complexes reported by (*left*) Fischer[38] and (*right*) Radius[37] ($Cp^* = \eta^5$-C_5Me_5; ^{i}PrIm = 1,3-di-isopropyl-imidazolin-2-ylidene).

The Peters group recently reported the preparation of a low-valent bis(phosphine)borane nickel complex, [^{Mes}DPB^{Ph}]Ni (**3.1**), which can reversibly cleave H_2 to generate the boro-hydridohydride species, [^{Mes}DPB^{Ph}](H)Ni(H), as shown in Scheme 3.2 ([^{Mes}DPB^{Ph}] = $MesB(o\text{-}PPh_2C_6H_4)_2$).[39] Preliminary results indicate that **3.1** is a competent olefin hydrogenation catalyst. Intrigued by the observed bifunctional activity of [^{Mes}DPB^{Ph}], the

work in this chapter seeks to access traditionally reactive nickel silyl hydride species by exploiting the stabilizing Ni→B interaction of **3.1**. Herein is described the preparation of well-characterized nickel borohydridosilyl complexes derived from the oxidative addition of silane substrates to a nickel(0) center and the mechanism of benzaldehyde hydrosilylation by **3.1**.

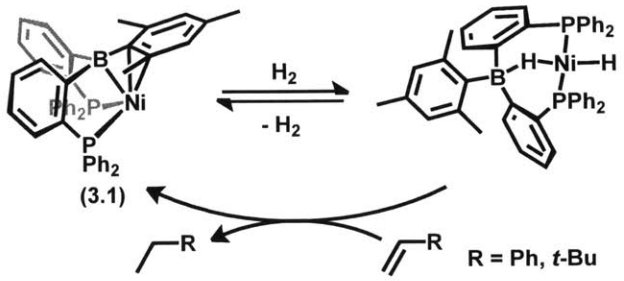

Scheme 3.2 Reversible H_2 activation by the bis(phosphine)borane nickel complex **3.1**. Complex **3.1** is also a competent hydrogenation catalyst.

3.2 Si–H and Ge–H Bond Activation

The previously reported nickel bis(phosphine)borane complex **3.1**, is prepared by comproportionation of 0.5 equiv of $Ni(cod)_2$ and 0.5 equiv of $NiCl_2$ in the presence of [^{Mes}DPB^{Ph}], followed by reduction with an excess of Na/Hg in THF (Scheme 3.3).[39] This species is a dark brown powder, with a singlet in the $^{31}P\{^1H\}$ NMR spectrum at 25.6 ppm. The ^1H NMR spectrum features three well-separated, diagnostic peaks at 5.63, 1.82 and 1.63 ppm, corresponding to the mesityl aryl protons, mesityl *p*-methyl group and the mesityl *o*-methyl groups, respectively. Complex **3.1** does not react with tertiary aryl or alkylsilanes, such as $HSiPh_3$, $HSiEt_3$ and $HSi(OEt)_3$; heating C_6H_6 solutions of **3.1** and a tertiary silane to 50 °C for 6 h does not promote any reaction. Heating C_6H_6 solutions of **3.1** and an excess of tertiary silane (i.e., more than 2 equiv) to 50 °C forms a complex mixture of products. Free mesitylene is a major product of these reactions and forms as a result of $B-C_{aryl}$ bond cleavage. Despite these complications, **3.1** does activate Si–H bonds of primary and secondary arylsilanes at room temperature.[40]

Treatment of a C_6H_6 solution **3.1** with 1 equiv of H_3SiPh resulted in an immediate

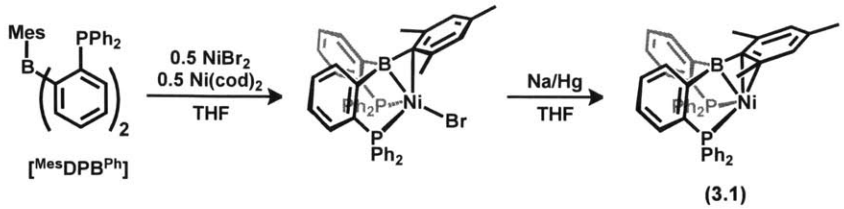

Scheme 3.3 Synthesis of **3.1**.

color change from brown to yellow-orange. Analysis of the reaction mixture after 2 h by $^{31}P\{^{1}H\}$ NMR spectroscopy indicated the quantitative consumption of **3.1**, concomitant with the formation of a single new product, [^{Mes}DPB^{Ph}](H)Ni(SiH_2Ph) (**3.2**, Scheme 3.4, left). Notably, no second Si−H bond activation occurs, nor is H_2 released during the course of the reaction. Complex **3.2** is obtained reliably as an orange powder in ca. 70% yield. In contrast, addition of 1 equiv of H_2SiPh_2 to **3.1** in C_6H_6 solution yields an equilibrium mixture of the yellow-orange borohydridosilyl complex [^{Mes}DPB^{Ph}](H)Ni($SiHPh_2$) (**3.3**), **3.1** and free H_2SiPh_2 (Scheme 3.4, right). Analytically pure samples of **3.3** can be isolated as a yellow-orange powder in ca. 75% yield by crystallization. Both **3.2** and **3.3** are readily soluble in THF, OEt_2, C_6H_6 and sparingly soluble in pentane and $O(SiMe_3)_2$.

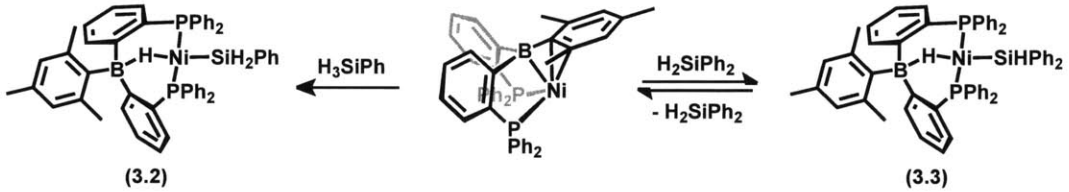

Scheme 3.4 Preparation of the nickel borohydridosilyl complexes **3.2** and **3.3**.

The signature NMR resonances of **3.2** are shown in Figure 3.2. The room temperature $^{31}P\{^{1}H\}$ NMR spectrum features a singlet at 41.1 ppm; this downfield shift is consistent with that observed for the previously reported complex, [^{Mes}DPB^{Ph}](H)Ni(H) (42.9 ppm, $^{2}J_{HP}$ = 52.1 Hz),[39] suggesting that the overall solution-state structures of the two species should be similar. While [^{Mes}DPB^{Ph}](H)Ni(H) has not been crystallographically characterized, the ^{1}H and $^{31}P\{^{1}H\}$ NMR spectra and DFT calculations imply a square planar nickel complex with a terminal hydride and a bridging borohydride ligand. The ^{1}H NMR spectrum of **3.2** features two unique resonances that integrate in a 2:1 ratio; the first is a sharp triplet centered at 4.30 ppm ($^{3}J_{HP}$ = 9.2 Hz, $^{1}J_{HSi}$ = 138 Hz) and the second is

a broad singlet at -2.47 ppm. The triplet arises from the coupling of the proton to two equivalent phosphorus nuclei. The presence of silicon satellites and the distinct chemical shift indicates that this resonance corresponds to the Si$-H$ protons. The broad resonance at -2.47 ppm is assigned to the bridging borohydride ligand. Although one might predict coupling of this proton to the two equivalent phosphorus nuclei, the expected line shape is broadened due to quadrupolar relaxation of the attached ^{11}B nucleus. The $^{11}\mathrm{B}\{^{1}\mathrm{H}\}$ NMR resonance of **3.2** is shifted upfield relative to **3.1** (-2.2 ppm vs 21.6 ppm), consistent with an increase in electron density at boron. The $^{29}\mathrm{Si}\{^{1}\mathrm{H}\}$ NMR spectrum features a triplet centered at -17.0 ppm ($^{2}J_{\mathrm{SiP}}$ = 38.7 Hz); the small $^{2}J_{\mathrm{SiP}}$ value suggests a *cis*-arrangement of the silicon and phosphorus atoms. The solid-state (ATR, thin film) IR spectrum contains an Si$-$H stretch at 2060 cm^{-1}. Taken together, these spectral features indicate that the geometry around the nickel center is as drawn in Scheme 3.4: a distorted square planar center with two *trans*-phosphine donors, a terminal silyl group and a hydride ligand bridging the nickel and boron centers.

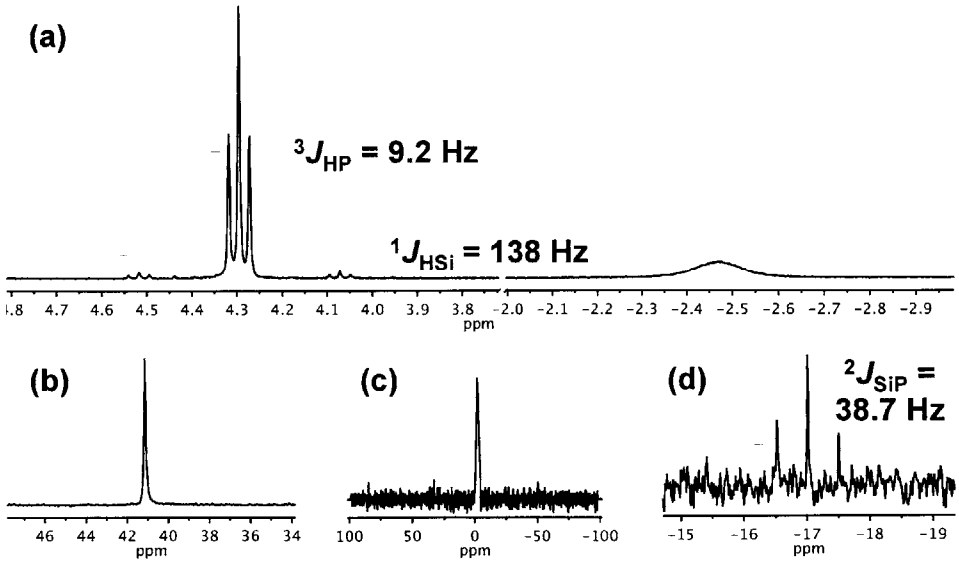

Figure 3.2 Signature resonances in the (*a*) ^{1}H, (*b*) $^{31}\mathrm{P}\{^{1}\mathrm{H}\}$, (*c*) $^{11}\mathrm{B}\{^{1}\mathrm{H}\}$, and (*d*) $^{29}\mathrm{Si}\{^{1}\mathrm{H}\}$ NMR spectra of **3.2**.

The NMR resonances of **3.3** are similar to those of **3.2** and a summary of the unique resonances is given in Table 3.1. The room temperature ^{1}H NMR spectrum of **3.3** features two signature resonances that integrate in a 1:1 ratio. The sharp triplet at 5.01 ppm ($^{3}J_{\mathrm{HP}}$

= 14.7 Hz, $^{1}J_{HSi}$ = 88 Hz) corresponds to the Si–*H* proton, while a broad resonance at −2.61 ppm is assigned as the bridging borohydride ligand. The $^{31}P\{^{1}H\}$ and $^{11}B\{^{1}H\}$ NMR resonances of 40.9 and −1.7 ppm, respectively, are analogous to those observed for **3.2**. The $^{29}Si\{^{1}H\}$ NMR spectrum shows a triplet centered at 3.1 ppm with a small $^{2}J_{SiP}$ coupling constant (37.9 Hz), again suggesting a *cis*-arrangement of the silicon and phosphorus atoms. The solid-state (ATR, thin film) IR spectrum contains a Si–H stretch at 2058 cm^{-1}.

	3.2	**3.3**
^{1}H δ (m)	4.30 (t, $^{3}J_{HP}$ = 9.2 Hz, $^{1}J_{HSi}$ = 138 Hz, 2H) −2.47 (s, 1H)	5.01 (t, $^{3}J_{HP}$ = 14.7 Hz, $^{1}J_{HSi}$ = 88 Hz, 1H) −2.61 (s, 1H)
^{31}P δ (m)	41.1 (s)	40.9 (s)
^{11}B δ (m)	−2.2 (br, s)	−1.7 (br, s)
^{29}Si δ (m)	−17.0 (t, $^{2}J_{SiP}$ = 38.7 Hz)	3.1 (t, $^{2}J_{SiP}$ = 37.9 Hz)

Table 3.1 Comparison of the signature NMR resonances of **3.2** and **3.3**.

The assignment of **3.2** and **3.3** was confirmed by X-ray crystallographic analysis. Both complexes crystallize in the triclinic space group $P\bar{1}$ with one and two molecules in the asymmetric unit, respectively. As predicted, the nickel centers are in distorted square planar geometries, with two *trans*-phosphine ligands, a terminal silyl group and a bridging borohydride ligand (Figure 3.3). Selected bond lengths and angles of **3.2** and **3.3** are summarized in Table 3.2. The nickel, phosphorus and silicon atoms are coplanar and the angles about nickel deviate slightly from the value expected for a square plane. This distortion is also reflected in the deviation of the P1–Ni–P2 and Si–Ni–H100 angles from ideal linearity. The average Ni–P distances (**3.2**: 2.1495(4) Å; **3.3**: 2.1713(7) and 2.1578(8) Å) are within the range found for other *trans*-phosphine nickel complexes (2.10 – 2.32 Å). There are very few structurally characterized bridging triarylborohydride transition metal complexes; however, the B–H distances of **3.2** (1.31(2)°) and **3.3** (1.26(3) and 1.27(3)°) are consistent with those in the literature (1.25 – 1.48 Å).[41–45] Although these previously reported species exhibit a wide range of B–H–M angles, the majority lie between ca. 100 and 120°. The B–H–Ni angles of **3.2** (114.27°) and **3.3** (118.72 and 120.20°) also fall

within that range. The Ni−H distances (**3.2**: 1.59(2) Å; **3.3**: 1.64(3) and 1.63(3) Å) are shorter than the M−H distances observed in bridging triarylborohydride transition-metal complexes (avg 2.02 Å). They are, however, similar to the average Ni−H distance of other terminal bis(phosphine) nickel(II) hydride species (1.52 Å).[35,46–55] The Ni−Si distances (**3.2**: 2.2379(4) Å; **3.3**: 2.24669(7) and 2.2491(7) Å) are comparable to other mononuclear nickel complexes containing a monodentate silyl fragment (2.14 – 2.37 Å).[30–32,37,56–60]

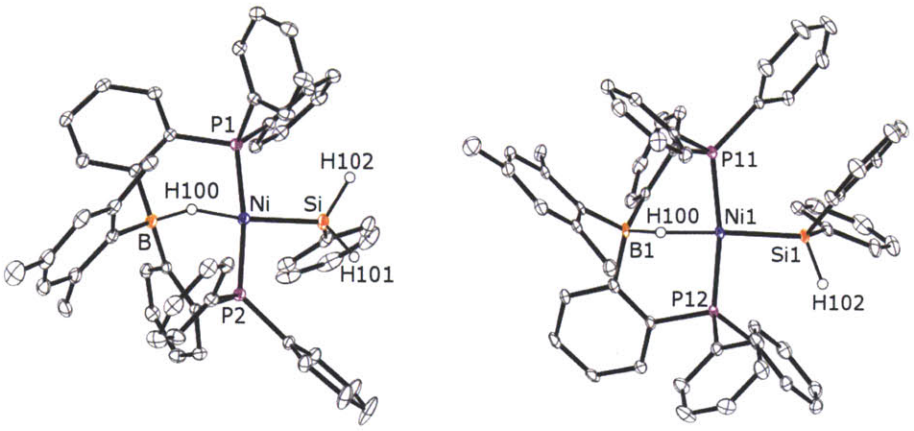

Figure 3.3 Solid-state structures of **3.2** (*left*) and **3.3** (*right*). Thermal ellipsoids are drawn at 40% probability. Hydrogen atoms bound to carbon and solvent molecules are omitted for clarity. For **3.3**, only one molecule of the asymmetric unit is shown.

Secondary arylgermanes are also activated by **3.1**; treatment of **3.1** with 1 equiv of H_2GePh_2 generates yellow [^{Mes}DPB^{Ph}](H)Ni(GeHPh$_2$) (**3.4**) in ca. 75% yield (Scheme 3.5). As with **3.2** and **3.3**, the room temperature $^{31}P\{^1H\}$ NMR resonance is shifted downfield from that of **3.1** (40.4 ppm) and the $^{11}B\{^1H\}$ NMR resonance of −0.8 ppm is indicative of increased electron density at boron. The sharp triplet at 4.64 ppm ($^3J_{HP}$ = 12.5 Hz) and the broad resonance at −4.28 ppm in the ^{1}H NMR spectrum are assigned to the Ge−*H* proton and bridging borohydride, respectively. Crystals for X-ray spectroscopic analysis were obtained by vapor diffusion of O(SiMe$_3$)$_2$ into a concentrated toluene solution of **3.4** and the structure is shown in Figure 3.4. Unfortunately, the crystals selected for data collection were not single and the solution to the structure of **3.4** poses some problems. Initial refinement suggests that the preferred solution is the triclinic space group $P\bar{1}$, with three independent molecules in the asymmetric unit. This solution furnishes two well-behaved molecules

	3.2	3.3	
		Molecule 1	*Molecule 2*
Ni–Si	2.2379(4)	2.2466(7)	2.2491(7)
Ni–P (avg)	2.1495(4)	2.1713(7)	2.1578(8)
Ni–B	2.440(2)	2.498(3)	2.514(3)
Ni–H100	1.59(2)	1.64(3)	1.63(3)
B–H100	1.31(2)	1.26(3)	1.27(3)
P1–Ni–Si	89.83(2)	98.91(3)	100.08(3)
P1–Ni–H100	87.2(7)	82.7(9)	84.8(9)
P2–Ni–Si	98.10(2)	90.34(3)	90.95(3)
P1–Ni–P2	171.81(2)	169.56(3)	168.63(3)
Si–Ni–H100	168.3(7)	167.2(9)	160.0(9)
B–H100–Ni	114.27	118.72	120.20

Table 3.2 Selected bond lengths (Å) and angles (°) for **3.2** and **3.3**.

and one highly disordered molecule with a number of non-positive definite atoms. The structure was revisited and refined using a smaller unit cell; this method provided a solution in the same space group ($P\bar{1}$) with one independent molecule in the asymmetric unit. Although this solution is more appropriate than the first ($R1 \approx 9\%$ vs 16%), the data is still of poor quality and only sufficient to provide a picture of the connectivity of the molecule. The geometry of **3.4** is distorted square planar with two *trans*-disposed phosphines and a terminal germyl ligand. The bridging borohydride ligand was not located in the difference map. The P–Ni–Ge angles are asymmetric; the P1–Ni–Ge angle is ca. 90.8° and the P2–Ni–Ge angle is ca. 98.0°. The Ni–Ge distance is ca. 2.3 Å and the average Ni–P distance is ca. 2.2 Å. These distances are expected given the metrical parameters of **3.2** and **3.3**.

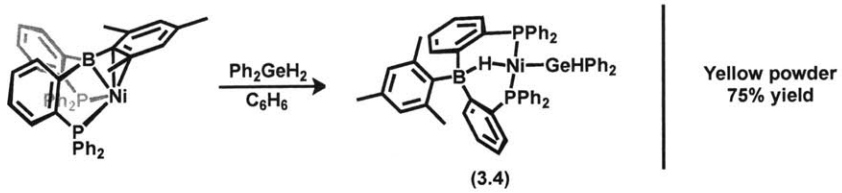

Scheme 3.5 Treatment of **3.1** with 1 equiv of H_2GePh_2 yields the borohydridogermyl complex **3.4**.

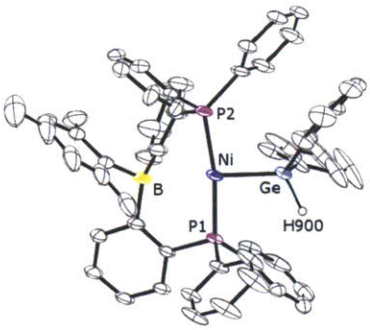

Selected Bond Lengths (Å) and Angles (°)
Ni–Ge = 2.3
Ni–P (avg) = 2.2
Ni–B = 2.5
P1–Ni–Ge = 90.8
P2–Ni–Ge = 98.0

Figure 3.4 Solid-state structure of **3.4**. Thermal ellipsoids are drawn at 40% probability. Hydrogen atoms bound to carbon are omitted for clarity. See the main text for more information about the selected bond lengths and angles.

Because of the greater interest in silane chemistry in the literature, the chemistry of **3.4** was not pursued. Other E−H bonds, such as O−H, N−H and P−H, are also of interest. However, treatment of THF solutions of **3.1** with these types of E−H substrates did not result in bond activation. For example, heating a THF solution of **3.1** with 1 equiv of HOPh to 70 °C for one week yielded no reaction; the addition of excess HOPh did not promote any reaction. Treatment of **3.1** with 1 equiv of $HPPh_2$ did result in the formation of a new product, but it was identified as the phosphine adduct, $[^{Mes}DPB^{Ph}]Ni(PHPh_2)$, not the desired P−H activated species. Complex **3.1** does activate S−H bonds and these results will be presented in Chapter 4.

3.3 $[^{Mes}DPB^{Ph}](H)Ni(SiHPh_2)$: Solution Equilibrium Studies

The well-defined solution equilibrium of **3.1** and **3.3** provided the opportunity to study both the thermodynamics and kinetics of Si−H bond activation by **3.1**. At 27 °C, dissolution of pure **3.3** in C_6D_6 gives an equilibrium mixture of **3.1**, **3.3** and H_2SiPh_2, corresponding to a K_{eq} of ca. 960 M^{-1}. A van't Hoff analysis over a 50 K range, shown in Figure 3.5, yielded thermal parameters of $\Delta H = -12 \pm 1$ kcal/mol and $\Delta S = -27 \pm 3$ eu. Repeating the experiment with D_2SiPh_2 over a 70 K range yielded thermal parameters of $\Delta H = -20 \pm 1$ kcal/mol and $\Delta S = -47 \pm 3$ eu, with an inverse equilibrium isotope effect of EIE_{328} =

0.18.[61] A representative ^{1}H NMR spectrum of this solution equilibrium taken at 65 °C in C_6D_6 is shown in Figure 3.6.

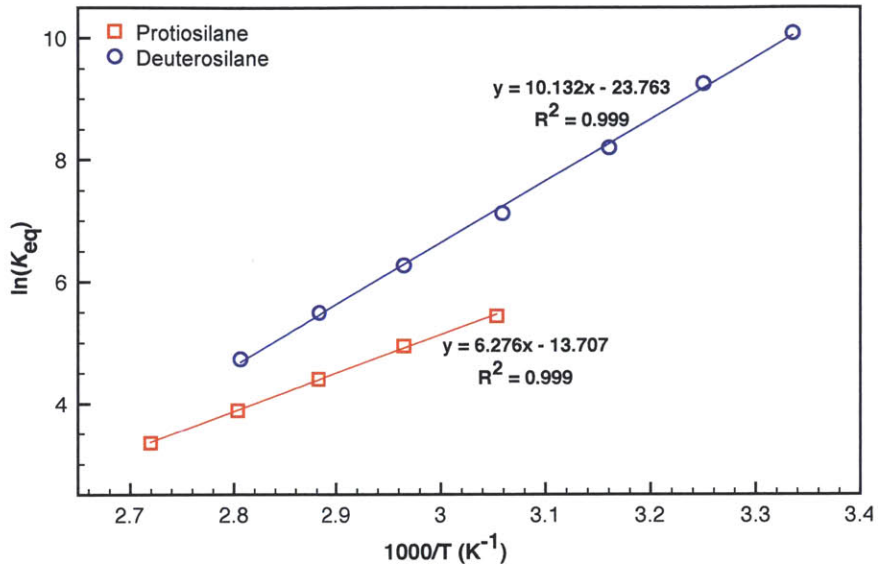

Figure 3.5 Van't Hoff plots derived from variable temperature ^{1}H NMR spectra of the solution equilibrium of **3.1**, **3.3** and free H_2SiPh or D_2SiPh_2. The equilibrium involving H_2SiPh_2 was monitored from 328 to 368 K, while the equilibrium involving D_2SiPh_2 was monitored from 298 to 358 K.

The chemical exchange kinetics of the Si−H bond activation process defined in Scheme 3.4 were studied by 2D exchange spectroscopy (EXSY) NMR experiments.[62,63] This well-established technique has been used to measure quantitative kinetic data of chemical exchange processes in organometallic complexes. In practice, the exchanging resonances must be resolved, meaning that the exchange process is slow on the NMR time scale. Too slow of an exchange process, however, can lead to a decrease in the cross-peak signal due to relaxation during the mixing time of the experiment. Thus, exchange processes with rates of ca. 10^2 to 10^{-2} s^{-1} can be appropriately investigated using the EXSY NMR technique.

^{1}H-^{1}H EXSY spectra were recorded in C_6D_6 over a range of temperatures with mixing times (T_m) of 0 and 700 ms. A representative EXSY spectrum recorded at 75 °C is shown in Figure 3.7. The Mes-*H* aryl resonances of **3.1** and **3.3** are well separated and so these were the peaks chosen for analysis. Figure 3.8 shows EXSY spectra recorded at 75 °C, expanded to focus on the Mes-*H* resonances of interest (left: T_m = 0 ms; right: T_m =700 ms). The peak

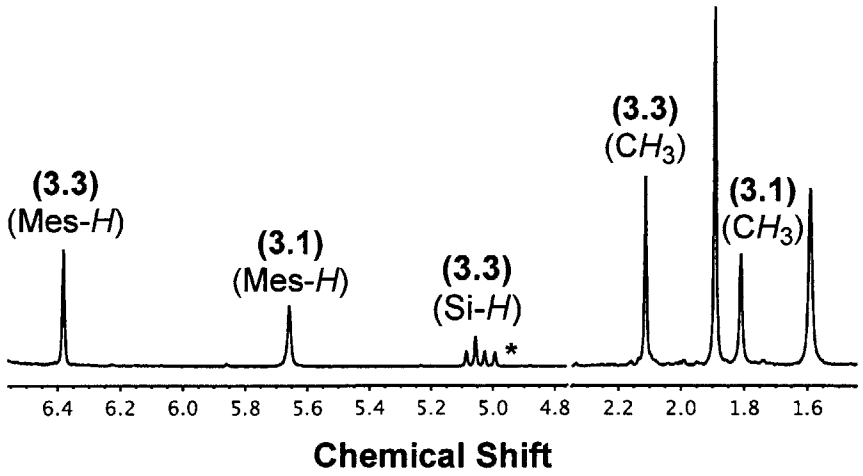

Figure 3.6 Representative ^{1}H NMR spectrum of the solution equilibrium of **3.1**, **3.3** and free H_2SiPh_2 collected at 65 °C in C_6D_6. Free H_2SiPh_2 is indicated by the ⋆ symbol.

volumes of the diagonal and off-diagonal signals were obtained by integration and then processed with EXSYCalc[64] to determine the forward (k'_1) and reverse (k'_{-1}) magnetization rate constants. These rates were then converted to chemical exchange rate constants, k_1 and k_{-1}, by taking into account the concentration of H_2SiPh_2 using the following equations:

$$k_1 = \frac{k'_{-1}}{[H_2SiPh_2]} \qquad k_{-1} = k'_{-1} \qquad K_{app} = \frac{k_1}{k_{-1}}$$

where the concentration of H_2SiPh_2 is assumed to be equal to the concentration of **3.1** in solution. The results of the analysis are shown in Table 3.3. The K_{app} values obtained from this technique are in good agreement with the K_{eq} values obtained by the variable temperature van't Hoff analysis. Eyring analysis of the data obtained from the EXSY experiments gave $\Delta H^{\ddagger} = 3.9 \pm 1$ kcal/mol and $\Delta S^{\ddagger} = -39 \pm 3$ eu for the forward reaction and $\Delta H^{\ddagger} = 17 \pm 1$ kcal/mol and $\Delta S^{\ddagger} = -9.6 \pm 3$ eu for the reverse process. Unfortunately, the chemical exchange process for the system with D_2SiPh_2 is too slow on the NMR time scale and study by the EXSY technique is not suitable.

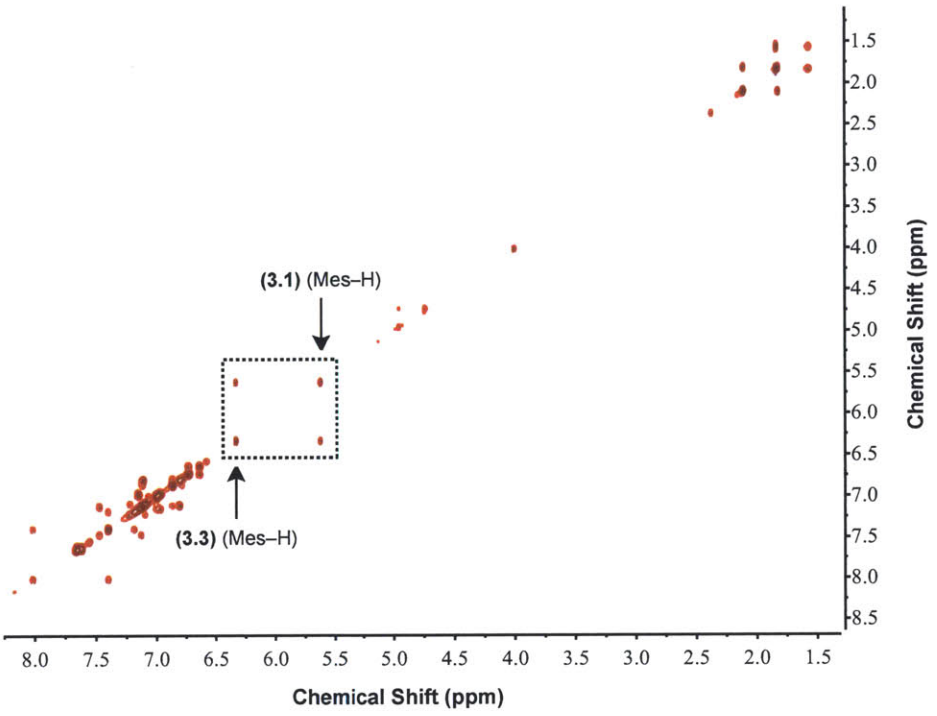

Figure 3.7 Representative ^{1}H-^{1}H EXSY NMR spectrum of the solution equilibrium of **3.1**, **3.3** and free H_2SiPh_2 (75 °C, C_6D_6, T_m = 700 ms).

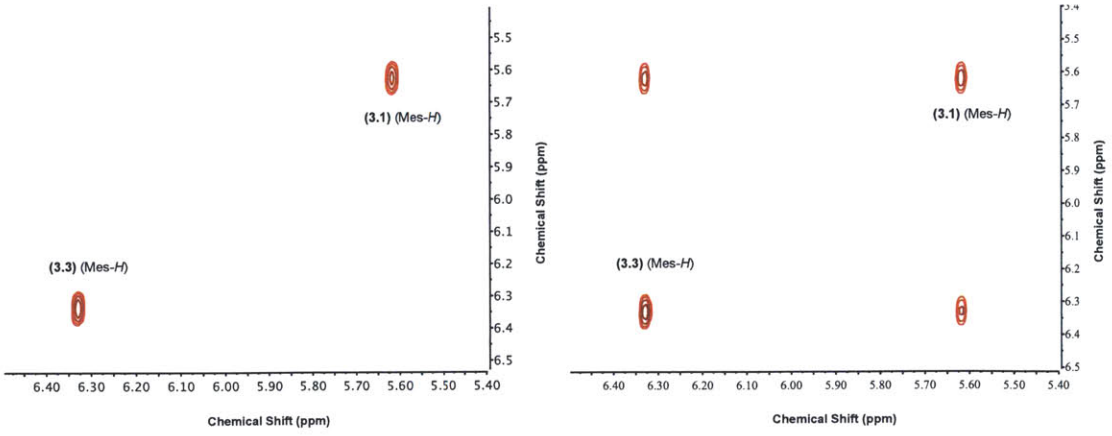

Figure 3.8 Expansion of the ^{1}H-^{1}H EXSY NMR spectrum of the solution equilibrium of **3.1**, **3.3** and free H_2SiPh_2 (75 °C, C_6D_6). (*left*) T_m = 0 ms. (*right*) T_m = 700 ms.

Temperature (K)	$[H_2SiPh_2]$ = [**3.1**] (M)	k_1 ($M^{-1}s^{-1}$)	k_{-1} (s^{-1})	K_{app} (M^{-1})	K_{eq}
327	1.29 x 10^{-2}	43	0.16	270	230
337	1.45 x 10^{-2}	51	0.36	140	139
347	1.76 x 10^{-2}	67	0.79	85	81
357	1.99 x 10^{-2}	73	1.4	50	49

Table 3.3 Rate constants for the solution equilibrium of **3.1**, **3.3** and free H_2SiPh_2 as determined by 2D EXSY spectroscopy. K_{eq} values determined by the variable temperature van't Hoff analysis are included for comparison.

3.4 Hydrosilylation of Benzaldehyde by [^{Mes}DPB^{Ph}]Ni

In an effort to incorporate the Si−H bond activation process into a useful catalytic cycle, the hydrosilylation of unsaturated substrates was examined. Attempts to hydrosilylate olefins and alkynes with 5 mol % of **3.1** at room temperature resulted in isomerization or no reaction, respectively; heating these reaction mixtures to 40 °C led to decomposition of **3.1** by B−C_{aryl} bond cleavage. Gratifyingly, the hydrosilylation of benzaldehyde with 5 mol % of **3.1** was accomplished in 99% yield within 6 h (Table 3.4, entry 1). Catalyst **3.1** is tolerant of a range of *para*-substituents, including electron-donating, electron-withdrawing and basic groups (Table 3.4). In general, the rate of reaction increases with more electron-donating substituents in the para position. This is in contrast to the iron pyridinediimine system (PDI) reported by Chirik.[65] Doubling the concentration of **3.1** doubled the reaction rate, suggesting that the transformation is first order in **3.1**. The rate of the reaction did not change with varying ratios of H_2SiPh_2 or aldehyde, indicating that the reaction is zero order in both H_2SiPh_2 and aldehyde substrate (Figure 3.9).

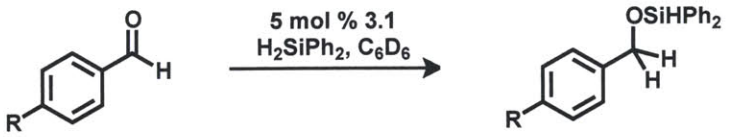

Entry[a]	Substrate	Conversion; Time	Chemical Yield[b]
1	R = H	>98%; 5.9 h	99%
2	R = Me	>98%; 2.5 h	97%
3	R = OMe	>98%; 2.7 h	98%
4	R = NMe_2	>98%; 44 m	98%
5	R = CF_3	>98%; 4.6 d	92%

[a] 1 mmol substrate, 1 mmol H_2SiPh_2, 5 mol % **3.1**, 500 μL C_6D_6. [b] Determined by NMR integration against an internal standard.

Table 3.4 Summary of results of catalytic hydrosilylation of *para*-substituted benzaldehydes by **3.1**.

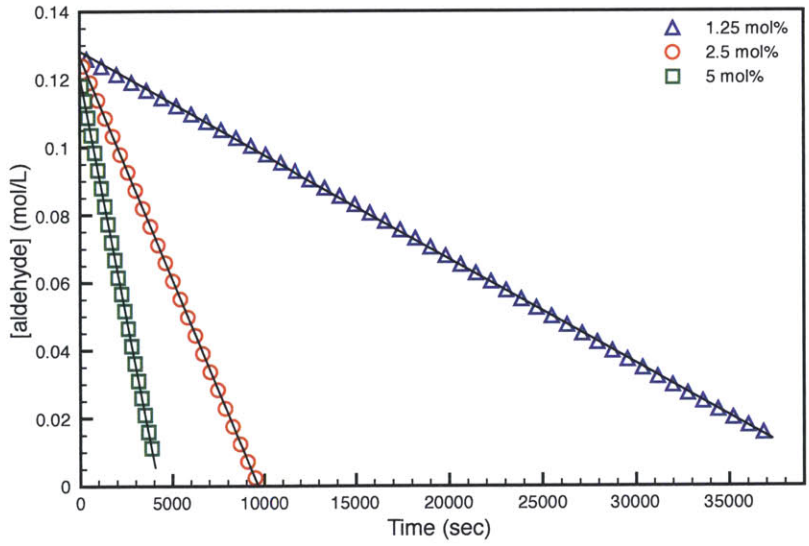

Figure 3.9 Plot of aldehyde concentration versus time for the hydrosilylation of *p*-dimethylaminobenzaldehyde by 1.25, 2.5 and 5 mol % of **3.1**.

In addition to studying the individual rates of hydrosilylation, competition experiments were carried out to assess substituent effects. For each experiment, the hydrosilylation of two equimolar substrates was monitored (1 equiv benzaldehyde A: 1 equiv benzaldehyde B: 1 equiv H_2SiPh_2) in the presence of 5 mol % of **3.1**. The Hammett correlation of the rel-

ative rates of hydrosilylation is illustrated in Figure 3.10 and shows that electron-donating substituents in the para position accelerate the rate of hydrosilylation. The reaction solution remained transparent during the course of catalysis and mercury has no effect on the rate or products of the reaction, supporting a homogeneous catalytic system.

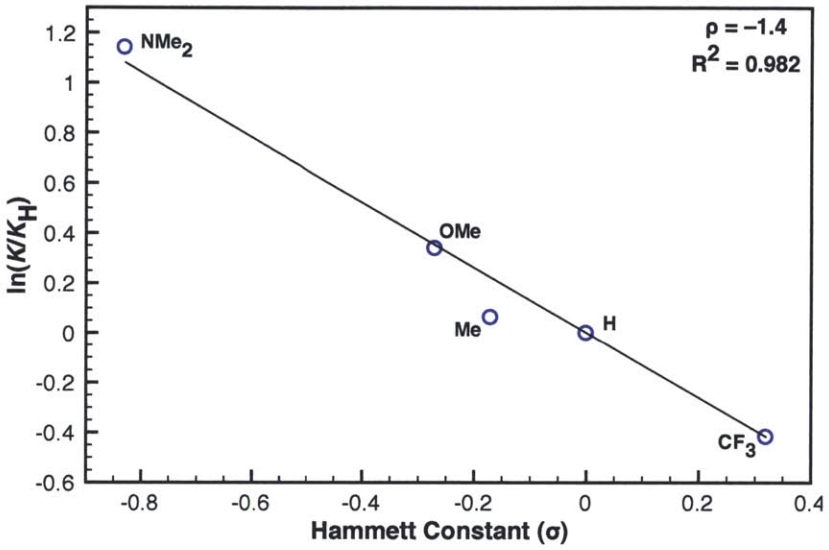

Figure 3.10 Hammett correlation diagram for the relative rates of hydrosilylation of *para*-substituted benzaldehydes by **3.1**.

3.5 Probing the Mechanism of Benzaldehyde Hydrosilylation

Typically, the transition metal-catalyzed reduction of carbonyl functionalities is mediated by rhodium, platinum and other precious metals. In recent years, however, there have been numerous efforts to incorporate more environmentally benign and less expensive first-row metals, such as titanium,[66–69] iron,[70–74] nickel[52,75–77] and copper.[78–80] Mechanistic proposals for these metal catalysts generally invoke a hydride mechanism in which a metal hydride species is generated, followed by carbonyl insertion into the M−H bond to give an alkoxide complex.

Three possible mechanisms for the hydrosilylation of benzaldehydes catalyzed by **3.1** are outlined in Scheme 3.6. In each mechanism, H_2SiPh_2 adds to **3.1** to generate **3.3**.

Benzaldehyde can insert into the Ni−H bond to generate a nickel alkoxide intermediate [**A**], which can then undergo reductive elimination of the organic product to regenerate **3.1** (Scheme 3.6, left). Alternatively, in an Ojima-type mechanism,[81] benzaldehyde can insert into the Ni−Si bond to generate a nickel borohydridosiloxyalkyl intermediate [**B**], followed by reductive elimination of the hydrosilylated product (Scheme 3.6, right). Finally, in a Zheng-Chan-type mechanism, benzaldehyde can insert into the Si−H bond to generate the intermediate species [**C**], which can then lose the organic product via reductive elimination to close the catalytic cycle (Scheme 3.6, right).[82]

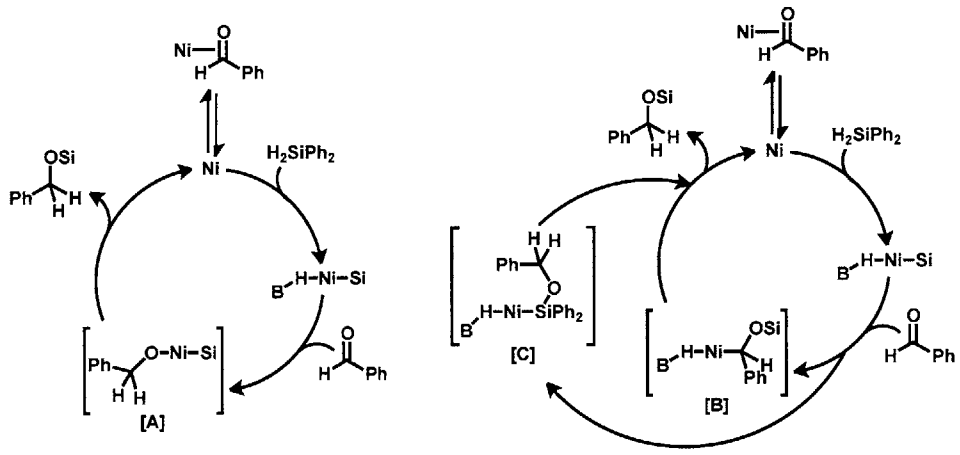

Scheme 3.6 Possible mechanisms for the hydrosilylation of benzaldehyde by **3.1**.

To better understand the hydrosilylation process, stoichiometric reactions were carried out using [$\alpha-^{13}$C]-benzaldehyde. Treatment of a toluene-d_8 solution of **3.1** with a stoichiometric amount of [$\alpha-^{13}$C]-benzaldehyde yielded a red solution with a singlet in the $^{31}P\{^1H\}$ NMR spectrum at 38.0 ppm. In the $^{13}C\{^1H\}$ NMR spectrum, there is a broad resonance at 84.1 ppm (free aldehyde = 193 ppm) that is coupled to a broad ^{1}H NMR resonance at 5.81 ppm, as determined by a 2D HSQC NMR experiment. Upon cooling to −60 °C, these features sharpen and shift, with a ^{1}H NMR resonance at 5.99 ppm that is coupled to a $^{13}C\{^1H\}$ NMR resonance at 91.3 ppm (HSQC). In the proton-coupled ^{13}C NMR spectrum at this temperature, the peak at 91.3 ppm splits into a doublet with J_{CH} = 174 Hz (free aldehyde, J_{CH} = 174 Hz). The upfield shifts of the ^{1}H and ^{13}C NMR resonances are indicative of substantial d→ $\pi^\star$ back donation,[83] consistent with other nickel η^2-aldehyde species reported in the literature.[84–86] Based on these observations, this new

species is assigned as [^{Mes}DPB^{Ph}]Ni(η^2-benzaldehyde) (**3.5**, Scheme 3.7, left).

Complex **3.5** was isolated as a red microcrystalline material in ca. 80% yield and the identity of **3.5** confirmed by X-ray crystallographic analysis (Figure 3.7, right). Complex **3.5** crystallizes in the monoclinic space group $P2_1/n$ with one molecule in the asymmetric unit. As predicted by the solution NMR data, the nickel atom is formally three-coordinate with benzaldehyde bound in an η^2 fashion. The C−O linkage lies in the trigonal coordination plane; the sum of the angles around the benzaldehyde carbon is 353.5(8)° and the phenyl ring and C=O bond are coplanar. The C−O bond length of 1.312(2) Å is slightly shorter than those reported for related Ni(η^2-CO) complexes (1.32 – 1.34 Å), for example, 1.345(2) Å in Ni(η^2-HPhCO)(dippe) (dippe = 1,2- bis(diisopropylphosphino)ethane), reported by Cámpora.[84]

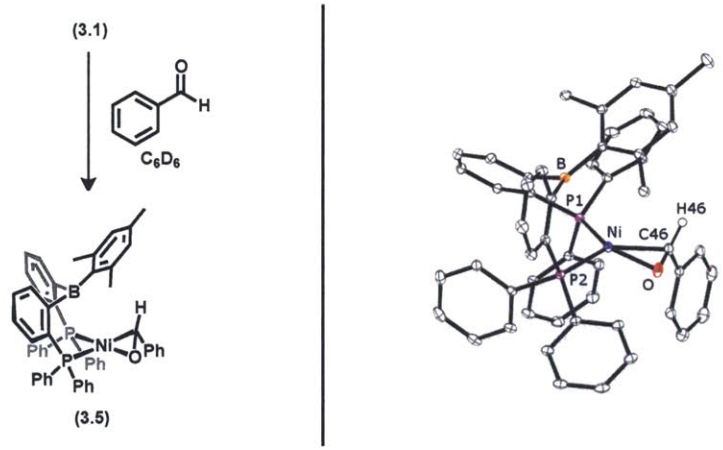

Scheme 3.7 (*left*) Preparation of **3.5**. (*right*) Solid-state structure of **3.5**. Thermal ellipsoids are drawn at 40% probability. Hydrogen atoms, except for H46, and solvent molecules are omitted for clarity. Selected bond lengths (Å) and angles (°) for **3.5**: Ni−P1 = 2.1376(2); Ni−P2 = 2.2198(2); Ni−O = 1.8749(6); Ni−C46 = 1.9906(8); C−O = 1.314(1); P1−Ni−P2 = 111.08(1); sum of the angles about C46 = 353.5(8).

Upon treatment of an equimolar solution of **3.1** and [$\alpha-^{13}$C]-benzaldehyde with stoichiometric H_2SiPh_2, a new intermediate species forms. This species has a half-life of ca. 15 minutes at room temperature. The $^{13}C\{^1H\}$ NMR spectrum of the solution features two singlets at 76.9 ppm and 66.4 ppm, corresponding to the intermediate and the final hydrosilylated product, respectively. In the proton-coupled ^{13}C NMR spectrum, the peak at 76.9 ppm splits into a doublet (J_{CH} = 159 Hz) and the peak at 66.4 ppm splits into a triplet (J_{CH}

= 142 Hz). Over the course of the reaction, the resonance associated with the intermediate decays, concomitant with growth of the product peak. The intermediate resonance is coupled to a ^{1}H NMR signal at 5.18 ppm, as determined by 2D HSQC NMR. In addition, there is a new hydride resonance at -11.4 ppm in the ^{1}H NMR spectrum. The $^{31}P\{^{1}H\}$ NMR spectrum exhibits a singlet at 38.0 ppm, corresponding to **3.5** and two doublets centered at 34.9 ($^{2}J_{PP}$ = 210.6 Hz) and 28.0 ppm ($^{2}J_{PP}$ = 210.6 Hz), corresponding to the intermediate species. These three sets of peaks decay over the course of the reaction and at the end of the reaction the only $^{31}P\{^{1}H\}$ NMR resonance is that of **3.1**. No other $^{31}P\{^{1}H\}$ NMR resonances are observed during the reaction, indicating that [^{Mes}DPB^{Ph}] remains bound to nickel throughout. No $^{13}C-^{31}P$ coupling was resolved, even upon cooling to -80 °C. Repeating the reaction under catalytic conditions (5 mol % of **3.1**) yielded spectra with signals analogous to those described above (Figure 3.11). Under these conditions, a small amount of an off-path, unidentified nickel complex is formed and best observed by $^{31}P\{^{1}H\}$ NMR spectroscopy. In addition to the peaks corresponding to **3.5** and the intermediate species, there is another set of doublets centered at 12.7 ($^{2}J_{PP}$ = 294.8 Hz) and 8.3 ppm ($^{2}J_{PP}$ = 294.8 Hz); this species does not decay over the course of the reaction and accounts for 6% of the total phosphorus content in solution, as determined by integration at the end of the reaction.

In evaluating the mechanisms and intermediates outlined in Scheme 3.6, the following considerations are of particular importance:

1. A hydride resonance is observed in the ^{1}H NMR spectrum, ruling out [**A**] as the intermediate species.

2. In the proton-coupled ^{13}C NMR spectrum, the peak corresponding to the intermediate species splits into a doublet, indicating that only one proton is directly attached to the ^{13}C-labeled carbon atom, thereby ruling out both [**A**] and [**C**] as the intermediate species.

3. Siloxyalkyl complexes of various transition metals have been reported in the literature[87–92] and the $^{13}C\{^{1}H\}$ NMR shifts of the metal-bound carbon atoms range from 69 ppm to 76 ppm; the $^{13}C\{^{1}H\}$ NMR shift of the intermediate species for this

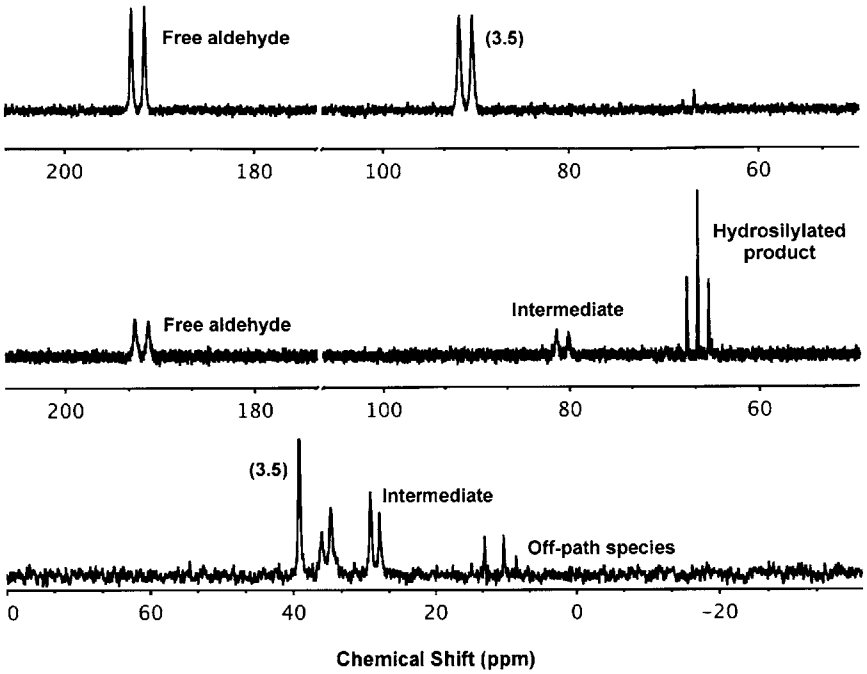

Figure 3.11 Representative spectra for hydrosilylation under catalytic conditions. (*top*) Proton-coupled ^{13}C NMR spectrum recorded at -60 °C after thawing the reaction mixture. (*middle*) Proton-coupled ^{13}C NMR spectrum recorded at -60 °C after removing from the probe and shaking at room temperature for 5 min. (*bottom*) $^{31}P\{^{1}H\}$ NMR spectrum recorded at room temperature 5 min after silane addition.

system (76.9 ppm) is slightly downfield of this range.

Taken together, the data is most consistent with the hydrosilylation reaction proceeding by an Ojima-type mechanism and the intermediate species observed being a nickel borohydridosiloxyalkyl complex (Scheme 3.6, right, [**B**]).

3.6 Conclusions and Future Work

In this chapter, the facile E−H (E = Si, Ge) bond activation by a nickel bis(phosphine)borane complex was described. The crystal structures of the resulting nickel borohydrido-E complexes were discussed. Complex [^{Mes}DPB^{Ph}](H)Ni(SiHPh$_2$) is in solution equilibrium with [^{Mes}DPB^{Ph}]Ni and free H_2SiPh_2 and the process was characterized by 2D EXSY NMR experiments. The system displays an inverse equilibrium isotope effect (EIE_{328} =

0.18). The catalytic hydrosilylation of *para*-substituted benzaldehydes by [^{Mes}DPB^{Ph}]Ni was studied. In general, the rate of hydrosilylation increased with electron-donating substituents in the *para*-position. The mechanism of the hydrosilylation transformation was explored and an intermediate species identified. The solution NMR spectral features are most consistent with an intermediate nickel borohydridosiloxyalkyl species that forms by insertion of aldehyde into the Ni–Si bond.

Given the facile Si–H bond activation by [^{Mes}DPB^{Ph}]Ni, future studies will explore the substrate scope and alternative reaction pathways. For example, preliminary studies have suggested that [^{Mes}DPB^{Ph}]Ni is an excellent catalyst for the dehydrogenative silylation of acetophenone to generate a silyl enol ether within minutes of silane addition, as shown in Scheme 3.8. Silyl enol ethers are important intermediates in organic synthesis and are frequently used as nucleophiles in Mukaiyama aldol additions[93] and Michael reactions.[94] Although they can be easily generated in situ under strongly basic conditions, the nickel-catalyzed dehydrogenative silylation reaction described above offers a base-free methodology that could allow for the incorporation of silyl enol ethers in base-sensitive transformations. The organometallic frustrated Lewis-pair approach outlined in this chapter will also be applied to other E–H bonds and unsaturated substrates in the context of two-electron organometallic reactions that are typically catalyzed by noble metals.

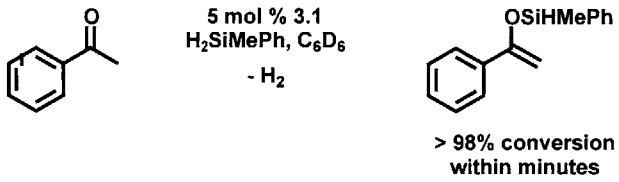

Scheme 3.8 Dehydrogenative silylation of acetophenone catalyzed by **3.1**.

3.7 Experimental Methods

3.7.1 General Considerations

All manipulations were carried out using standard Schlenk or glovebox techniques under a dinitrogen atmosphere, unless otherwise indicated. Unless otherwise noted, solvents

were dried and deoxygenated by sparging with argon and passing through activated alumina in a solvent purification system from SG Waters USA, LLC (Nashua, NH). Non-halogenated solvents were tested with a standard purple solution of sodium benzophenone ketyl in tetrahydrofuran in order to confirm effective oxygen and moisture removal. **3.1**[39] and [$\alpha-^{13}$C]-benzaldehyde[95] were prepared according to literature methods. D_2SiPh_2 was prepared via lithium aluminum deuteride (LAD) reduction of Cl_2SiPh_2 in OEt_2. All other reagents were purchased from commercial suppliers and used without further purification. Elemental analyses were performed by Midwest Microlab, LLC (Indianapolis, IN) and Robertson Microlit Laboratories, Inc (Ledgewood, NJ). Deuterated solvents were purchased from Cambridge Isotope Laboratories, Inc., degassed, and dried over activated 3-Å molecular sieves prior to use.

3.7.2 Spectroscopic Measurements

Varian 300, 400 and 500 MHz spectrometers were used to record ^{1}H, ^{13}C, ^{31}P, ^{29}Si and ^{11}B NMR spectra at room temperature, unless otherwise noted. ^{1}H and ^{13}C NMR chemical shifts were referenced to the residual solvent peaks. ^{31}P NMR chemical shifts were referenced to external 85% phosphoric acid ($\delta = 0$ ppm). ^{11}B NMR chemical shifts were referenced to external $BF_3 \cdot Et_2O$ ($\delta = 0$ ppm). ^{29}Si NMR chemical shifts were referenced to external tetramethylsilane. Infrared measurements were obtained in thin films using a Bruker ALPHA FT-IR spectrometer equipped with a diamond ATR probe and OPUS/Mentor software. GC-MS analyses were performed on an Agilent Technologies 6890N GC system with an HP-5MS column.

3.7.3 Preparation of [^{Mes}DPB^{Ph}](H)NiSiH$_2$Ph (3.2)

To a solution of **3.1** (44.5 mg, 62.6 μmol) in benzene (1 mL) was added neat H_3SiPh (7.8 μL, 63.2 μmol). The solution was stirred 2 h at room temperature and pentane was added to precipitate an orange powder. The slurry was stirred for another 30 min and the solids collected. The solids were washed with pentane and dried in vacuo (36.6 mg, 71%). Crystals suitable for X-ray analysis were by slow evaporation of a OEt_2 solution. ^{1}H NMR

(400 MHz, C_6D_6) δ 7.63 (q, J = 5.8 Hz, 4H), 7.52 (d, J = 7.4 Hz, 2H), 7.33 – 7.22 (m, 6H), 7.14 – 7.07 (m, 4H), 7.06 – 6.82 (m, 17H), 6.43 (s, 2H), 4.30 (t, $^3J_{HP}$ = 9.2 Hz, $^1J_{HSi}$ = 138 Hz, 2H), 2.14 (s, 3H), 1.93 (s, 6H), −2.47 (s, 1H). $^{13}C\{^1H\}$ NMR (101 MHz, C_6D_6) δ 141.2, 136.5, 135.0, 133.8, 133.5, 130.6, 130.0, 129.8, 129.6, 128.9, 127.0, 126.3, 25.2, 20.6. $^{31}P\{^1H\}$ NMR (162 MHz, C_6D_6) δ 41.1 (s). $^{29}Si\{^1H\}$ NMR (79 MHz, C_6D_6) δ −17.0 (t, J = 38.7 Hz). $^{11}B\{^1H\}$ NMR (128 MHz, C_6D_6) δ −2.2. IR (ATR, C_6H_6 film, cm^{-1}): 2060. Anal. Calcd for $C_{51}H_{47}BNiP_2Si \cdot OEt_2$: C, 73.93; H, 6.43. Found: C, 74.05; H, 6.13.

3.7.4 Preparation of [^{Mes}DPB^{Ph}](H)NiSiHPh$_2$ (3.3)

To a solution of **3.1** (59.4 mg, 83.5 μmol) in benzene (1 mL) was added neat H_2SiPh_2 (16.4 μL, 88.1 μmol). The solution was stirred 2 h at room temperature and pentane was added to precipitate a yellow powder. The slurry was stirred for another 30 min and the solids collected. The solids were washed with pentane and dried in vacuo (56.8 mg, 76%). Crystals suitable for X-ray analysis were by slow evaporation of a C_6H_6 solution. ^1H NMR (400 MHz, toluene-d_8) δ 7.69 (s, 4H), 7.43 (d, J = 7.5 Hz, 2H), 7.18 (s, 2H), 7.15 – 6.91 (m, 20H), 6.89 – 6.76 (m, 6H), 6.71 – 6.60 (m, 4H), 6.33 (s, 2H), 5.01 (t, $^3J_{HP}$ = 14.7 Hz, $^1J_{HSi}$ = 88 Hz, 1H), 2.11 (s, 3H), 1.84 (s, 6H), −2.61 (s, 1H). $^{13}C\{^1H\}$ NMR (101 MHz, C_6D_6) δ 141.2, 139.3, 137.1, 136.3, 135.6, 134.1, 133.8, 133.1, 130.5, 129.9, 129.8, 129.3, 128.9, 127.5, 127.4, 127.0, 126.3, 124.5, 25.4, 20.6. $^{31}P\{^1H\}$ NMR (162 MHz, C_6D_6) δ 40.9 (s). $^{29}Si\{^1H\}$ NMR (79 MHz, C_6D_6) δ 3.1 (t, J = 37.9 Hz). $^{11}B\{^1H\}$ NMR (128 MHz, C_6D_6) δ −1.7. IR (ATR, C_6H_6 film, cm^{-1}): 2058. Anal. Calcd for $C_{57}H_{51}BNiP_2Si$: C, 76.45; H, 5.74. Found: C, 76.03; H, 5.99.

3.7.5 Preparation of [^{Mes}DPB^{Ph}](H)NiGeHPh$_2$ (3.4)

To a solution of **3.1** (44.3 mg, 62.3 μmol) in benzene (1 mL) was added neat H_2GePh_2 (11.8 μL, 63.5 μmol). The solution was stirred 12 h at room temperature, frozen and lyophilized. Crystalline material was obtained by vapor diffusion of $O(SiMe_3)_2$ into a concentrated toluene solution. The solids were washed with $O(SiMe_3)_2$ and dried in vacuo

(45.3 mg, 76%). Crystals suitable for X-ray analysis were grown by the same method. ^{1}H NMR (400 MHz, C_6D_6) δ 7.73 (q, J = 4.2 Hz, 4H), 7.49 (d, J = 7.5 Hz, 2H), 7.22 – 7.14 (m, 2H), 7.14 – 7.05 (m, 10H), 7.00 – 6.89 (m, 10H), 6.86 (t, J = 7.3 Hz, 4H), 6.77 (t, J = 7.4 Hz, 2H), 6.63 (t, J = 7.5 Hz, 4H), 6.36 (s, 2H), 4.64 (t, $^{3}J_{HP}$ = 12.5 Hz, 1H), 2.08 (s, 3H), 1.88 (s, 6H), −4.28 (s, 1H). $^{13}C\{^{1}H\}$ NMR (101 MHz, C_6D_6) δ 142.4, 141.1, 135.9, 135.1, 133.8, 133.4, 130.7, 129.9, 129.8, 129.4, 128.9, 126.9, 126.3, 25.4, 20.6. $^{31}P\{^{1}H\}$ NMR (162 MHz, C_6D_6) δ 40.4 (s). $^{11}B\{^{1}H\}$ NMR (128 MHz, C_6D_6) δ −0.8. Anal. Calcd for $C_{57}H_{51}BGeNiP_2$: C, 72.82; H, 5.47. Found: C, 73.08; H, 5.60.

3.7.6 Preparation of [^{Mes}DPB^{Ph}]Ni(η^2-benzaldehyde) (3.5)

To a slurry of **3.1** (53.2 mg, 74.8 μmol) in pentane (15 mL) was added neat benzaldehyde (7.7 μL, 75.5 μmol). The slurry was stirred 2 h at room temperature, during which time brown-red microcrystalline material precipitated. The solids were collected and washed with pentane, then dried in vacuo (48.2 mg, 78%). Crystals suitable for X-ray analysis were by slow evaporation of a toluene solution. ^{1}H NMR (500 MHz, C_6D_6) δ 7.77 – 7.59 (m, 4H), 7.07 – 6.87 (m, 14H), 6.87 – 6.71 (m, 7H), 6.68 (d, J = 4.7 Hz, 4H), 6.50 (s, 2H), 6.48 – 6.38 (m, 4H), 6.25 (s, 1H), 2.35 (s, 6H), 2.07 (s, 3H). $^{13}C\{^{1}H\}$ NMR (126 MHz, C_6D_6) δ 161.9, 145.7, 144.0, 140.0, 134.2, 132.5, 132.3, 139.6, 128.7, 126.5, 125.2, 124.7, 84.1, 26.9, 21.0. $^{31}P\{^{1}H\}$ NMR (202 MHz, C_6D_6) δ 38.6 (s). $^{11}B\{^{1}H\}$ NMR (128 MHz, C_6D_6) δ 58.2 (br). Anal. Calcd for $C_{52}H_{45}BNiOP_2$: C, 76.41; H, 5.55. Found: C, 76.03; H, 5.99.

3.7.7 General Procedure for Catalytic Hydrosilylation Experiments

In a typical experiment, a J. Young NMR tube was charged with **3.1** (100 μL, 0.039 M in C_6D_6), substrate (20 equiv relative to **3.1**), ferrocene (83 μL, 0.236 M in C_6D_6), C_6D_6 and frozen. Once frozen, H_2SiPh_2 (20 equiv relative to **3.1**) was added and the tube frozen (total volume = 600 μL). Once at the spectrometer, the solution was thawed and spectra collected at regular intervals. After completion, the reaction mixture was exposed to air, diluted with toluene, filtered through a plug of silica and analyzed by GC-MS. Hydrosilylation

products were identified using ^{1}H NMR and GC-MS data in comparison to the literature data.[65,96,97] To aid characterization, (1-(4-trifluoromethylphenyl)methoxy)diphenylsilane was converted to 4-(trifluoromethyl)phenyl methanol by treatment with 1 M HCl; the ^{1}H NMR and GC-MS data obtained agree with the literature data.[98]

3.7.8 General Procedure for Stoichiometric Hydrosilylation Experiments.

In a typical experiment, a J. Young NMR tube was charged with **3.1**, [$\alpha-^{13}$C]-benzaldehyde (1 equiv relative to **3.1**), toluene-d_8 (ca. 500 μL) and frozen. Once frozen, H_2SiPh_2 (1 equiv relative to **3.1**) was added and the tube frozen. Once at the spectrometer, the solution was thawed and pertinent spectra collected.

3.7.9 Mercury Tests for Homogeneity

Method 1: A solution of **3.1** (30 μL, 0.061 M, 5 mol %) in C_6D_6 was stirred with excess Hg (0.0726 g, ca. 200 equiv per nickel atom) for 15 min. A solution of *p*-dimethylaminobenzaldehyde (0.0052 g, 34.8 μmol) and H_2SiPh_2 (6.5 μL, 35.0 μmol) in C_6D_6 was added and the mixture stirred at 23 °C for 2 h. The solution was then filtered through Celite and analyzed by ^{1}H NMR spectroscopy. Complete hydrosilylation was observed.

Method 2: **3.1** (30 μL, 0.061 M, 5 mol %) was added to a C_6D_6 solution of *p*-dimethylaminobenzaldehyde (0.0052 g, 34.8 μmol) and H_2SiPh_2 (6.5 μL, 35.0 μmol). The resulting solution was stirred for 5 min at 23 °C, then added to Hg (0.0465 g, ca. 125 equiv per nickel atom) and stirred for 2 h at 23 °C. The mixture was filtered through Celite and analyzed by ^{1}H NMR spectroscopy. Complete hydrosilylation was observed.

3.7.10 Variable Temperature van't Hoff Study of the Equilibrium of 3.1 and 3.3

Ferrocene and **3.3** were dissolved in toluene-d_8 and transferred to a sealed J. Young NMR tube. The tube was inserted into a temperature controlled NMR probe and ^{1}H NMR spectra

were collected at 10 K intervals from 328 K to 368 K, allowing 20 min for equilibration at each temperature. The concentrations of **3.1** and **3.3** were determined by integration of the mesityl aryl C-H resonance for the respective complexes and H_2SiPh_2 concentration was assumed to be equal to the concentration of **3.1**. The plot of $\ln(K_{obs})$ as a function of T^{-1} was fit by a line and the enthalpy and entropy of the reaction were extracted from the slope and intercept, respectively.

3.7.11 Variable Temperature van't Hoff Study of the Equilibrium of 3.1 and [^{Mes}DPB^{Ph}](D)Ni(SiDPh$_2$)

Ferrocene, D_2SiPh_2 and **3.1** were dissolved in toluene-d_8 and transferred to a sealed J. Young NMR tube. The tube was inserted into a temperature controlled NMR probe and a ^{1}H NMR spectra were collected at 10 K intervals from 298 K to 358 K, allowing 20 min for equilibration at each temperature. The concentrations of **3.1** and [^{Mes}DPB^{Ph}](D)Ni(SiDPh$_2$) were determined by integration of the mesityl aryl C-H resonance for the respective complexes and D_2SiPh_2 concentration was assumed to be equal to the concentration of **3.1**.

3.7.12 2D ^{1}H-^{1}H EXSY study of the equilibrium of 3.1 and 3.3

2D ^{1}H-^{1}H EXSY spectra were collected using the samples prepared for the variable temperature experiments outlined above. To determine the exchange rates of the equilibrium between **3.1** and **3.3**, two 2D EXSY experiments were acquired (mixing time, T_m = 0 ms and 700 ms) at 10 K intervals from 328 K to 368 K, allowing 30 min for equilibration at each temperature.

3.7.13 X-ray Crystallographic Details

Single crystals of **3.2** were obtained by slow evaporation of a OEt_2 solution, crystals of **3.3** were grown by slow evaporation of a C_6H_6 solution, crystals of **3.4** were obtained by vapor diffusion of $O(SiMe_3)_2$ into a concentrated toluene solution, crystals of **3.5** were grown by slow evaporation of a toluene solution. Low-temperature single crystal X-ray diffraction studies were carried out at the Beckman Institute Crystallography Facility on a

Bruker Kappa Apex II diffractometer with Mo Kα radiation ($\lambda = 0.71073$ Å). Crystals were coated with Paratone-N oil and mounted on glass fibers. Structures were solved by direct or Patterson methods using SHELXS[99] and refined against F2 on all data by full-matrix least squares with SHELXL-97[100] using established refinement techniques.[101] All non-hydrogen atoms were refined anisotropically. All hydrogen atoms (except the hydrogen atoms bound to heteroatoms in **3.2**, **3.3** and **3.4**) were included into the model at geometrically calculated positions and refined using a riding model. The isotropic displacement parameters of all calculated hydrogen atoms were fixed to 1.2 times the U values of the atoms they are linked to (1.5 times for methyl groups). Thermal ellipsoid diagrams were created using Olex2.[102] In the structure of **3.2**, the OEt_2 solvent molecule was disordered over two sites. The structure of **3.5** contained one positionally disordered toluene solvent molecule. The toluene molecule was refined anisotropically, however hydrogen atoms were not added due to the complicated nature of the positional disorder. The crystallographic details for **3.2**, **3.3**, **3.4** and **3.5** are summarized in Tables 3.5 and 3.6.

	3.2 · OEt_2	**3.3** · 0.5 C_6H_6
Formula	$C_{26.50}H_{26}B_{0.50}Ni_{0.50}O_{0.25}PSi_{0.50}$	$C_{60}H_{54}BNiP_2Si$
Formula Weight	428.25	934.58
Temperature/K	100(2)	100(2)
Crystal syst.	Triclinic	Triclinic
Space group	$P\bar{1}$	$P\bar{1}$
Color	Orange	Yellow
a/Å	11.6097(8)	12.1452(6)
b/Å	13.0379(9)	20.3316(10)
c/Å	17.3875(12)	21.4335(11)
α/°	68.361(4)	69.986(3)
β/°	72.030(4)	77.017(3)
γ/°	64.875(4)	82.180(3)
V/^{3}	2178.5(3)	4835.7(4)
ρ (calc.)/(gcm^{-1})	1.306	1.284
Z	4	4
No. refl.	105776	107064
No. unique refl.	13243	19001
R_{int}	0.0472	0.0675
R_1 (all data)[a]	0.0467	0.0686
wR_2 (all data)[b]	0.0904	0.1192
R_1 [(I >2σ)]	0.0358	0.0442
wR_2 [(I >2σ)]	0.0831	0.1068
GOF[c]	1.036	1.021

Table 3.5 Crystallographic summary for **3.2**, **3.3** and **3.5**. [a]$R_1 = \Sigma||F_0 - |F_e||/\Sigma|F_0|$. [b]$wR_2 = (\Sigma[w(F_0^2 - F_e^2)^2]/\Sigma[w(F_0^2)^2])^{1/2}$. [c]$GOF = (\Sigma[w(F_0^2 - F_e^2)^2]/(n-p))^{1/2}$ where n is the number of data and p is the number of parameters refined.

	3.4	**3.5** · C_7
Formula	$C_{57}H_{50}BGeNiP_2$	$C_{55.50}H_{45}BNiOP_2$
Formula Weight	939.02	859.38
Temperature/K	100(2)	100(2)
Crystal syst.	Triclinic	Monoclinic
Space group	$P\bar{1}$	$P2_1/n$
Color	Orange	Red
a/Å	9.626(2)	12.9166(8)
b/Å	12.422(3)	15.2418(9)
c/Å	20.146(4)	22.8933(15)
$\alpha/^\circ$	79.14(3)	90
$\beta/^\circ$	77.22(3)	105.256(3)
$\gamma/^\circ$	87.68(3)	90
V/^{3}	2307.2(8)	4348.2(5)
ρ (calc.)/(gcm^{-1})	1.352	1.313
Z	2	4
No. refl.	89439	250827
No. unique refl.	12960	30670
R_{int}	0.0371	0.0536
R_1 (all data)[a]	0.1092	0.0710
wR_2 (all data)[b]	0.1789	0.1058
R_1 [(I >2σ)]	0.0845	0.0385
wR_2 [(I >2σ)]	0.1642	0.0935
GOF[c]	1.035	1.025

Table 3.6 Crystallographic summary for **3.4** and **3.5**. [a]$R_1 = \Sigma||F_0 - |F_e||/\Sigma|F_0|$. [b]$wR_2 = (\Sigma[w(F_0^2 - F_e^2)^2]/\Sigma[w(F_0^2)^2])^{1/2}$. [c]$GOF = (\Sigma[w(F_0^2 - F_e^2)^2]/(n-p))^{1/2}$ where n is the number of data and p is the number of parameters refined.

3.8 Bibliography

[1] Crabtree, R. H. *The Organometallic Chemistry of the Transition Metals*; John Wiley & Sons: New York, 2001.

[2] Ball, Z. In *Comprehensive Organometallic Chemistry III*; Crabtree, R. H., Mingos, D. M. P., Eds.; Elsevier: Oxford, UK, 2007; pp 789–813.

[3] Hayashi, T.; Yamasaki, K. In *Comprehensive Organometallic Chemistry III*; Crabtree, R. H., Mingos, D. M. P., Eds.; Elsevier: Oxford, UK, 2007; pp 815–838.

[4] Ojima, I. In *The Chemistry of Organic Silicon Compounds*; Patai, S., Rappoport, Z., Eds.; John Wiley & Sons: Chichester, UK, 1989; pp 1479–1526.

[5] Marciniec, B. *Silicon Chem.* **2002**, *1*, 155–174.

[6] Magistrato, A.; Woo, T. K.; Togni, A.; Rothlisberger, U. *Organometallics* **2004**, *23*, 3218–3227.

[7] Sakaki, S.; Mizoe, N.; Sugimoto, M. *Organometallics* **1998**, *17*, 2510–2523.

[8] Chalk, A. J.; Harrod, J. F. *J. Am. Chem. Soc.* **1965**, *87*, 16–21.

[9] Sakaki, S.; Sumimoto, M.; Fukuhara, M.; Sugimoto, M.; Fujimoto, H.; Matsuzaki, S. *Organometallics* **2002**, *21*, 3788–3802.

[10] Bergens, S. H.; Noheda, P.; Whelan, J.; Bosnich, B. *J. Am. Chem. Soc.* **1992**, *114*, 2128–2135.

[11] Beddie, C.; Hall, M. B. *J. Phys. Chem. A* **2006**, *110*, 1416–1425.

[12] Beddie, C.; Hall, M. B. *J. Am. Chem. Soc.* **2004**, *126*, 13564–13565.

[13] Brunner, H. *Angew. Chem. Int. Ed.* **2004**, *43*, 2749–2750.

[14] Glaser, P. B.; Tilley, T. D. *J. Am. Chem. Soc.* **2003**, *125*, 13640–13641.

[15] Corey, J. Y. *Chem. Rev.* **2011**, *111*, 863–1071.

[16] Shimada, S.; Tanaka, M. *Coord. Chem. Rev.* **2006**, *250*, 991–1011.

[17] Corey, J. Y.; Braddock-Wilking, J. *Chem. Rev.* **1999**, *99*, 175–292.

[18] Nakata, N.; Fukazawa, S.; Kato, N.; Ishii, A. *Organometallics* **2011**, *30*, 4490–4493.

[19] Boyle, R. C.; Mague, J. T.; Fink, M. J. *J. Am. Chem. Soc.* **2003**, *125*, 3228–3229.

[20] Braddock-Wilking, J.; Zhang, Y.; Corey, J. Y.; Rath, N. P. *J. Organomet. Chem.* **2008**, *693*, 1233–1242.

[21] Arii, H.; Takahashi, M.; Noda, A.; Nanjo, M.; Mochida, K. *Organometallics* **2008**, *27*, 1929–1935.

[22] Chan, D.; Duckett, S. B.; Heath, S. L.; Khazal, I. G.; Perutz, R. N.; Sabo-Etienne, S.; Timmins, P. L. *Organometallics* **2004**, *23*, 5744–5756.

[23] Kim, Y.-J.; Choi, E.-H.; Lee, S. W. *Organometallics* **2003**, *22*, 3316–3319.

[24] Simons, R. S.; Sanow, L. M.; Galat, K. J.; Tessier, C. A.; Youngs, W. J. *Organometallics* **2000**, *19*, 3994–3996.

[25] Ozawa, F.; Kamite, J. *Organometallics* **1998**, *17*, 5630–5639.

[26] Tsuji, Y.; Nishiyama, K.; Hori, S.-I.; Ebihara, M.; Kawamura, T. *Organometallics* **1998**, *17*, 507–512.

[27] Koizumi, T.-A.; Osakada, K.; Yamamoto, T. *Organometallics* **1997**, *16*, 6014–6016.

[28] Azizian, H.; Dixon, K. R.; Eaborn, C.; Pidcock, A.; Shuaib, N. M.; Vinaixa, J. *J. Chem. Soc., Chem. Commun.* **1982**, 1020–1022.

[29] Eaborn, C.; Pidcock, A.; Ratcliff, B. *J. Organomet. Chem.* **1972**, *43*, C5–C6.

[30] Iluc, V. M.; Hillhouse, G. L. *J. Am. Chem. Soc.* **2010**, *132*, 11890–11892.

[31] Smith, E. E.; Du, G.; Fanwick, P. E.; Abu-Omar, M. M. *Organometallics* **2010**, *29*, 6527–6533.

[32] Adhikari, D.; Pink, M.; Mindiola, D. J. *Organometallics* **2009**, *28*, 2072–2077.

[33] Kang, S. O.; Lee, J.; Ko, J. *Coord. Chem. Rev.* **2002**, *231*, 47–65.

[34] Takaya, J.; Iwasawa, N. *Dalton Trans.* **2011**, *40*, 8814–8821.

[35] Iluc, V. M.; Hillhouse, G. L. *Tetrahedron* **2006**, *62*, 7577–7582.

[36] Chen, W.; Shimada, S.; Tanaka, M.; Kobayashi, Y.; Saigo, K. *J. Am. Chem. Soc.* **2004**, *126*, 8072–8073.

[37] Zell, T.; Schaub, T.; Radacki, K.; Radius, U. *Dalton Trans.* **2011**, *40*, 1852–1854.

[38] Steinke, T.; Gemel, C.; Cokoja, M.; Winter, M.; Fischer, R. A. *Angew. Chem. Int. Ed.* **2004**, *43*, 2299–2302.

[39] Harman, W. H.; Peters, J. C. *J. Am. Chem. Soc.* **2012**, *134*, 5080–5082.

[40] MacMillan, S. N.; Harman, W. H.; Peters, J. C. *Manuscript in Preparation.*

[41] Liu, S.; Liu, F.-C.; Renkes, G.; Shore, S. G. *Organometallics* **2001**, *20*, 5717–5723.

[42] Arndt, P.; Baumann, W.; Spannenberg, A.; Rosenthal, U.; Burlakov, V. V.; Shur, V. B. *Angew. Chem. Int. Ed.* **2003**, *42*, 1414–1418.

[43] Al-Humydi, A.; Garrison, J. C.; Mohammed, M.; Youngs, W. J.; Collins, S. *Polyhedron* **2005**, *24*, 1234–1249.

[44] Choukroun, R.; Lorber, C.; Vendier, L.; Lepetit, C. *Organometallics* **2006**, *25*, 1551–1553.

[45] Arndt, P.; Jäger-Fiedler, U.; Klahn, M.; Baumann, W.; Spannenberg, A.; Burlakov, V. V.; Rosenthal, U. *Angew. Chem. Int. Ed.* **2006**, *45*, 4195–4198.

[46] Lansing, R. B., Jr.; Goldberg, K. I.; Kemp, R. A. *Dalton Trans.* **2011**, *40*, 8950–8958.

[47] Lin, S.; Day, M. W.; Agapie, T. *J. Am. Chem. Soc.* **2011**, *133*, 3828–3831.

[48] Hatnean, J. A.; Beck, R.; Borrelli, J. D.; Johnson, S. A. *Organometallics* **2010**, *29*, 6077–6091.

[49] Boro, B. J.; Duesler, E. N.; Goldberg, K. I.; Kemp, R. A. *Inorg. Chem.* **2009**, *48*, 5081–5087.

[50] Steinke, T.; Shaw, B. K.; Jong, H.; Patrick, B. O.; Fryzuk, M. D. *Organometallics* **2009**, *28*, 2830–2836.

[51] Laird, M. F.; Pink, M.; Tsvetkov, N. P.; Fan, H.; Caulton, K. G. *Dalton Trans.* **2009**, 1283–1285.

[52] Chakraborty, S.; Krause, J. A.; Guan, H. *Organometallics* **2009**, *28*, 582–586.

[53] Liang, L.-C.; Chien, P.-S.; Lee, P.-Y. *Organometallics* **2008**, *27*, 3082–3093.

[54] Aresta, M.; Quaranta, E.; Dibenedetto, A.; Giannoccaro, P.; Tommasi, I.; Lanfranchi, M.; Tiripicchio, A. *Organometallics* **1997**, *16*, 834–841.

[55] Müller, U.; Keim, W.; Krüger, C.; Betz, P. *Angew. Chem. Int. Ed. Engl.* **1989**, *28*, 1011–1013.

[56] Stoelzel, M.; Präsang, C.; Inoue, S.; Enthaler, S.; Driess, M. *Angew. Chem. Int. Ed.* **2012**, *51*, 399–403.

[57] Tavčar, G.; Sen, S. S.; Azhakar, R.; Thorn, A.; Roesky, H. W. *Inorg. Chem.* **2010**, *49*, 10199–10202.

[58] Meltzer, A.; Inoue, S.; Präsang, C.; Driess, M. *J. Am. Chem. Soc.* **2010**, *132*, 3038–3046.

[59] Meltzer, A.; Präsang, C.; Driess, M. *J. Am. Chem. Soc.* **2009**, *131*, 7232–7233.

[60] Schaub, T.; Döring, C.; Radius, U. *Dalton Trans.* **2007**, 1993–2002.

[61] Churchill, D. G.; Janak, K. E.; Wittenberg, J. S.; Parkin, G. *J. Am. Chem. Soc.* **2003**, *125*, 1403–1420.

[62] Pastor, A.; Martínez-Viviente, E. *Coord. Chem. Rev.* **2008**, *252*, 2314–2345.

[63] Pons, M.; Millet, O. *Prog. Nucl. Magn. Reson. Spectrosc.* **2001**, *38*, 267–324.

[64] EXSYCalc. `http://www.mestrec.com/`.

[65] Tondreau, A. M.; Lobkovsky, E.; Chirik, P. J. *Org. Lett.* **2008**, *10*, 2789–2792.

[66] Ramón, D. J.; Yus, M. *Chem. Rev.* **2006**, *106*, 2126–2208.

[67] Bandini, M.; Bernardi, F.; Bottoni, A.; Cozzi, P. G.; Miscione, G. P.; Umani-Ronchi, A. *Eur. J. Org. Chem.* **2003**, 2972–2984.

[68] Beagley, P.; Davies, P. J.; Blacker, A. J.; White, C. *Organometallics* **2002**, *21*, 5852–5858.

[69] Yun, J.; Buchwald, S. L. *J. Am. Chem. Soc.* **1999**, *121*, 5640–5644.

[70] Darwish, M.; Wills, M. *Catal. Sci. Technol.* **2012**, *2*, 243–255.

[71] Junge, K.; Schröder, K.; Beller, M. *Chem. Commun.* **2011**, *47*, 4849–4859.

[72] Chirik, P. J. *Catal. Precious Met.* **2010**, 83–110.

[73] Zhang, M.; Zhang, A. *Appl. Organomet. Chem.* **2010**, *24*, 751–757.

[74] Morris, R. H. *Chem. Soc. Rev.* **2009**, *38*, 2282–2291.

[75] Kundu, S.; Brennessel, W. W.; Jones, W. D. *Inorg. Chem.* **2011**, *50*, 9443–9453.

[76] Tran, B. L.; Pink, M.; Mindiola, D. J. *Organometallics* **2009**, *28*, 2234–2243.

[77] Fontaine, F.-G.; Zargarian, D. *Organometallics* **2002**, *21*, 401–408.

[78] Lipshutz, B. H. *Synlett* **2009**, *4*, 509–524.

[79] Díez-González, S.; Nolan, S. P. *Acc. Chem. Res.* **2008**, *41*, 349–358.

[80] Rendler, S.; Oestreich, M. *Angew. Chem. Int. Ed.* **2007**, *46*, 498–504.

[81] Ojima, I.; Kogure, T.; Kumagai, M.; Horiuchi, S.; Sato, T. *J. Organomet. Chem.* **1976**, *122*, 83–97.

[82] Zheng, G. Z.; Chan, T. H. *Organometallics* **1995**, *14*, 70–79.

[83] Tolman, C. A.; English, A. D.; Manzer, L. E. *Inorg. Chem.* **1975**, *14*, 2353–2356.

[84] Matas, I.; Cámpora, J.; Palma, P.; Álvarez, E. *Organometallics* **2009**, *28*, 6515–6523.

[85] Ogoshi, S.; Ueta, M.; Arai, T.; Kurosawa, H. *J. Am. Chem. Soc.* **2005**, *127*, 12810–12811.

[86] Walther, D. *J. Organomet. Chem.* **1980**, *190*, 393–401.

[87] Akita, M.; Mitani, O.; Sayama, M.; Moro-oka, Y. *Organometallics* **1991**, *10*, 1394–1399.

[88] Gregg, B. T.; Hanna, P. K.; Crawford, E. J.; Cutler, A. R. *J. Am. Chem. Soc.* **1991**, *113*, 384–385.

[89] Hanna, P. K.; Gregg, B. T.; Cutler, A. R. *Organometallics* **1991**, *10*, 31–33.

[90] Akita, M.; Mitani, O.; Moro-oka, Y. *J. Chem. Soc., Chem. Commun.* **1989**, 527–529.

[91] Selover, J. C.; Vaughn, G. D.; Strouse, C. E.; Gladysz, J. A. *J. Am. Chem. Soc.* **1986**, *108*, 1455–1462.

[92] Gladysz, J. A. *Acc. Chem. Res.* **1984**, *17*, 326–332.

[93] Mukaiyama, T.; Narasaka, K.; Banno, K. *Chem. Lett.* **1973**, 1011–1014.

[94] Miyashita, M.; Yanami, T.; Kumazawa, T.; Yoshikoshi, A. *J. Am. Chem. Soc.* **1984**, *106*, 2149–2156.

[95] Blake, M. E.; Bartlett, K. L.; Jones, M., Jr. *J. Am. Chem. Soc.* **2003**, *125*, 6485–6490.

[96] Wei, Y.; Han, S.; Kim, J.; Soh, S.; Grzybowski, B. A. *J. Am. Chem. Soc.* **2010**, *132*, 11018–11020.

[97] Yang, J.; Tilley, T. D. *Angew. Chem. Int. Ed.* **2010**, *49*, 10186–10188.

[98] Nagendra, G.; Madhu, C.; Vishwanatha, T. M.; Sureshbabu, V. V. *Tetrahedron Lett.* **2012**, *53*, 5059–5063.

[99] Sheldrick, G. M. *Acta Cryst.* **1990**, *A46*, 467–473.

[100] Sheldrick, G. M. SHELXL-97: Program for Crystal Structure Refinement. University of Göttingen, Göttingen, Germany, 1997.

[101] Müller, P. *Crystallogr. Rev.* **2009**, *15*, 57–83.

[102] Dolomanov, O. V.; Bourhis, L. J.; Gildea, R. J.; Howard, J. A. K.; Puschmann, H. *J. Appl. Cryst.* **2009**, *42*, 339–341.

4 Isolation of an Unusual Nickel(I) Borohydridothiolate Complex

Contents

4.1 Introduction

Hydrothiolation, much like the hydrosilylation processes discussed in Chapter 3, is a well-recognized synthetic method for the functionalization of unsaturated substrates with 100% atom efficiency.[1] The addition of S−H bonds to alkynes offers a stunning array of mechanistic pathways, including radical,[2–6] nucleophilic[7,8] and metal-mediated processes.[9–12] In general, however, these reactions can be grouped into two classes: those that activate the alkyne substrate and those that activate the thiol. For non-metal-mediated catalysis, the products of hydrothiolation are the anti-Markovnikov species shown in Scheme 4.1 (left). The ratio of the *cis* and *trans* olefins is dependent on the substituents (R, Ar) and the reaction conditions.[13] Interestingly, for metal-mediated transformations a change in the regioselectivity of the thiol addition can occur and α-vinyl sulfides can be obtained with varying degrees of selectivity (Scheme 4.1, right). In the presence of some transition-metal catalysts, the desired α-vinyl sulfide isomerizes to a mixture of *cis* and *trans* olefins.[14,15]

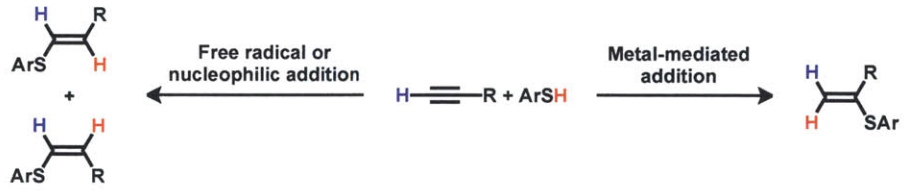

Scheme 4.1 Hydrothiolation pathways for (*left*) radical or nucleophilic addition and (*right*) metal-mediated addition of thiols to alkynes.

Thiol S−H bonds can be activated by transition metals either through an acid/base reaction to generate a metal thiolate complex or by oxidative addition of the S−H bond to yield a metal hydride thiolate species.[13] The acid/base activation pathway is typically observed for transition-metal catalysts containing palladium and nickel,[15–18] while the oxidative addition route is usually observed for rhodium-based catalysts.[14,19–21] The oxidative addition pathway is particularly intriguing, as the formation of a metal hydride thiolate complex may allow for ligand-based control of the alkyne insertion into either the M−S or M−H

bonds, thereby determining the regioselectivity of the reaction.[13] This principle is illustrated in Scheme 4.2. The electronically and sterically preferred 1,2-insertion (rather than 2,1-insertion) of an alkyne into the M−H bond gives rise to linear thioether products, while insertion into the M−S bond yields the Markovnikov vinyl sulfide. A non-precious-metal catalyst that could selectively direct alkyne insertion into the M−S bond rather than the M−H bond would therefore be an important advance in the preparation of branched vinyl sulfides.

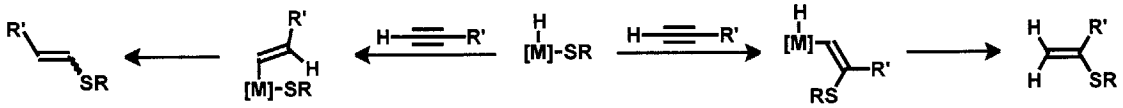

Scheme 4.2 (*left*) Alkyne insertion into the M−H bond results in the formation of linear thioether products. (*right*) Insertion into the M−S bond forms branched Markovnikov vinyl sulfide compounds.

Nickel-based catalysts have recently emerged as more economic alternatives to traditional palladium hydrothiolation catalysts. For example, $NiCl_2$ catalyzes the addition of thiophenol to 1-heptyne; the addition of NEt_3 dramatically increased the yield of the Markovnikov addition product (15% vs 84%).[18] During hydrothiolation with a number of nickel-based catalysts, there is evidence for the formation of polymeric (and potentially insoluble) nickel thiolate species (e.g., $[Ni(SPh)_2]_n$).[13] In response to this concern, Nolan introduced the use of a series of complexes of the form [CpNi(NHC)Cl] (NHC = N-heterocyclic carbene) as strictly homogeneous catalysts and mechanistic studies have invoked the formation of a monothiolate organonickel species as an intermediate along the catalytic pathway.[1] From these examples, it is clear that while significant advances in nickel-catalyzed hydrothiolation are being made, this chemistry is dominated by acid/base chemistry (i.e., necessity of NEt_3, formation of thiolate complexes) and so the preparation of isolable nickel hydride thiolate complexes derived directly from S−H oxidative addition is a worthwhile pursuit of fundamental interest.

Nickel thiolate complexes are also important in biological catalysis. Eight nickel-containing enzymes have been identified that perform a variety of important transformation;[22,23] four of these eight enzymes contain nickel thiolate bonds in their active sites. Nickel superoxide dismustate (Ni-SOD) catalyzes the disproportionation of superoxide into

O_2 and hydrogen peroxide.[24] NiFe hydrogenase reversibly reduces protons to H_2.[25] CO dehydrogenase (CODH) reversibly interconverts CO and CO_2.[26,27] Acetyl-CoA synthetase produces acetyl-coenzyme A (acetyl-CoA) from CO, CoA and a methyl group.[28,29] For each of these systems, the nickel sites are flexible in both their coordination number and redox chemistry, with the nickel(I), nickel(II) and nickel(III) oxidation states implicated in several catalytically relevant species.[30–32]

As described in Chapter 3, the bis(phosphine)borane nickel complex [^{Mes}DPB^{Ph}]Ni (**3.1**) activates Si−H bonds under ambient conditions to generate isolable nickel borohydridosilyl species. Having demonstrated facile E−H bond activation, we sought to broaden the scope of these reactions to include other substrates, such as N−H, O−H and S−H bonds. While we were unable to effect either N−H or O−H bond activation, the S−H bonds of arylthiols were easily activated. Described in this chapter are the preparation of a series of well-defined nickel borohydridothiolate complexes and the isolation of a rare nickel(I) borohydridothiolate species. Catalytic functionalization reactions incorporating S−H bond activation by [^{Mes}DPB^{Ph}]Ni have yet to be realized, however the chemistry describe herein provides a starting point for their development.

4.2 Isolation of a Nickel(II) Borohydridothiolate Complex

Treatment of a C_6H_6 solution of **3.1** with 1 equiv HSPh resulted in an immediate color change from dark brown to emerald green. Analysis of the crude reaction mixture after 2 hr by ^{1}H and ^{31}P$\{^1$H$\}$ NMR spectroscopy indicated the quantitative consumption of **3.1** and the formation of a new diamagnetic product, [^{Mes}DPB^{Ph}](H)Ni(SPh) (**4.1**, Scheme 4.3). After workup, **4.1** was obtained as a dark green powder in ca. 85% yield. The ^{1}H NMR spectrum of **4.1** features resonances from 8 to −13 ppm; a broad triplet centered at −12.23 ppm integrates to one proton and is attributed to the bridging borohydride ligand. The triplet pattern arises from the coupling of the proton to two equivalent phosphorus nuclei ($^2J_{HP}$ = 26.1 Hz). Interesting to note is that for the related nickel borohydridosilyl and borohydridogermyl complexes discussed in Chapter 3 and the borohydridohydride species previously reported,[33] no coupling of the bridging borohydride resonance to phosphorus

could be resolved in the ^{1}H NMR spectrum, even upon cooling to -60 °C. The $^{31}P\{^{1}H\}$ NMR spectrum of **4.1** features a singlet at 37.9 ppm. At -80 °C, the phosphorus nuclei are inequivalent and split into two doublets centered at 50.7 ppm ($^{1}J_{PP}$ = 280.4 Hz) and 39.4 ppm ($^{1}J_{PP}$ = 280.7 Hz).

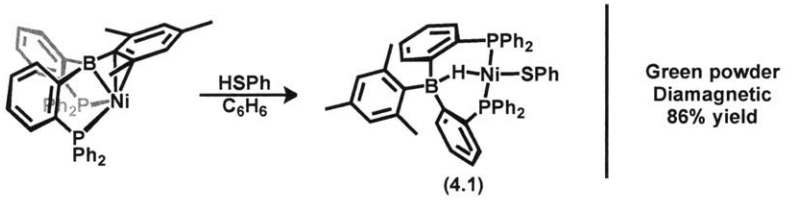

Scheme 4.3 Treatment of **3.1** with 1 equiv HSPh yields the green borohydridothiolate complex **4.1**.

Complex **4.1** is soluble in THF, OEt_2, C_6H_6 and pentane. Single crystals were obtained by vapor diffusion of $O(SiMe_3)_2$ into a concentrated toluene solution of **4.1**. Complex **4.1** crystallizes in the monoclinic space group $P2_1$ with one molecule per asymmetric unit. The geometry at nickel is distorted square planar with two *trans*-disposed phosphine donors, a terminal thiolate group and a hydride bridging the nickel and boron centers (Figure 4.1). Consistent with a distorted square planar geometry is the observation that the P1–Ni–P2 and S–Ni–H100 angles are non-linear (160.16(1)° and 165.1(6)°, respectively) and that the nickel center lies slightly outside the P1–S–P2 plane (0.308 Å). The average Ni–P bond length of 2.1804(3) Å falls within the range (2.10 – 2.27 Å) for other structurally characterized, four-coordinate nickel bis(phosphine) complexes. This Ni–S distance of 2.1782(3) Å is also typical of other four-coordinate mononuclear nickel complexes containing monodentate thiolate ligands (2.12 – 2.34 Å).

While the formation of hydride thiolate complexes via oxidative addition of an S–H bond of H_2S is well-documented, the analogous reaction with thiols is rare. To our knowledge, **4.1** is the second structurally characterized nickel hydride thiolate complex, the first being the N-heterocyclic carbene (NHC) supported complex, $Ni(^{i}Pr_2Im)_2(H)(S^{t}Bu)$ ($^{i}Pr_2Im$ = 1,3-diisopropyl-imidazol-2-ylidene), reported by Radius.[34] The solid-state structure of this species is similar to **4.1** and features a nickel center with two *trans*-disposed NHC ligands, an alkylthiolate moiety and a terminal hydride. The bond angles around nickel are distorted from ideal square planar geometry due to the steric interaction of

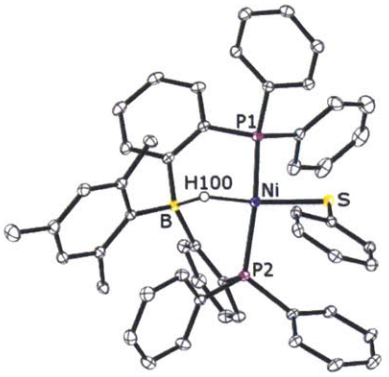

Selected Bond Lengths (Å) and Angles (°)
Ni–P1 = 2.1585(3)
Ni–P2 = 2.2023(3)
Ni–S = 2.1782(3)
Ni–H100 = 1.50(1)
Ni–B = 2.511(1)
B–H100 = 1.35(2)
P1–Ni–P2 = 160.16(6)
S–Ni–H100 = 165.1(6)

Figure 4.1 Solid-state structure of **4.1**. Thermal ellipsoids are drawn at 40% probability. Hydrogen atoms except for the bridging borohydride (H100) are omitted for clarity.

the NHC ligands and the alkylthiolate ligand (C19–Ni–H = 86.57(2)°, C1–Ni–H = 75.82(2)°, C19–Ni–S = 89.7(1)° and C1–Ni–S = 107.8(1)°). Complex **4.1** is not as distorted (P1–Ni–H = 89.0(6)°, P2–Ni–H = 86.8(6)°, P1–Ni–S = 91.32(1)° and P2–Ni–S = 97.55(1)°). In this case, the phenyl group of the thiolate rotates such that it is perpendicular to the P1–S–P2 plane (88.32°), thereby alleviating the need for a more distorted geometry. The structural parameters of these two species are compared in Figure 4.2.

C1–Ni–H = 75.82(2)°
C19–Ni–H = 86.57(2)°
C1–Ni–S = 107.8(1)°
C19–Ni–S = 89.7(1)°

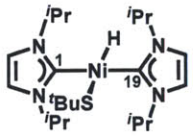

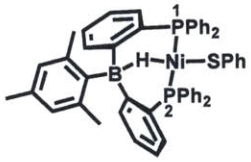

P1–Ni–H = 89.0(6)°
P2–Ni–H = 86.8(6)°
P1–Ni–S = 91.32(1)°
P2–Ni–S = 97.55(1)°

Figure 4.2 Comparison of an NHC-supported nickel hydride thiolate complex (*left*) and the bis(phosphine)borane complex **4.1** (*right*).

4.3 Substituent Effects on S–H Bond Activation

Having established facile S–H bond activation of HSPh with **3.1**, the activation of *para*-substituted thiophenols was investigated. Treatment of a C_6H_6 solution **3.1** with 1 equiv of *p*-X-thiophenol (X = NH_2, (**4.2**); Cl, (**4.3**); F, (**4.4**); CF_3, (**4.5**); OMe, (**4.6**)) yielded the corresponding nickel borohydridothiolate complex (Scheme 4.4). The $^{31}P\{^1H\}$ NMR spectra of all the borohydridothiolate complexes feature a singlet between 37 and 42 ppm. The ^1H

NMR spectra are also very similar; each spectrum contains a broad triplet centered between -12 and -13 ppm that corresponds to the bridging borohydride ligand. The $^{2}J_{HP}$ coupling could not be resolved for **4.2** and a broad singlet rather than a triplet was observed. The $^{11}B\{^{1}H\}$ NMR spectra each display a singlet centered at ca. 5 ppm. The lack of change between the various NMR spectra for **4.2** – **4.6** suggests that their ground state solution structures are similar. The NMR spectroscopic features of the nickel borohydridothiolate complexes are summarized in Table 4.1.

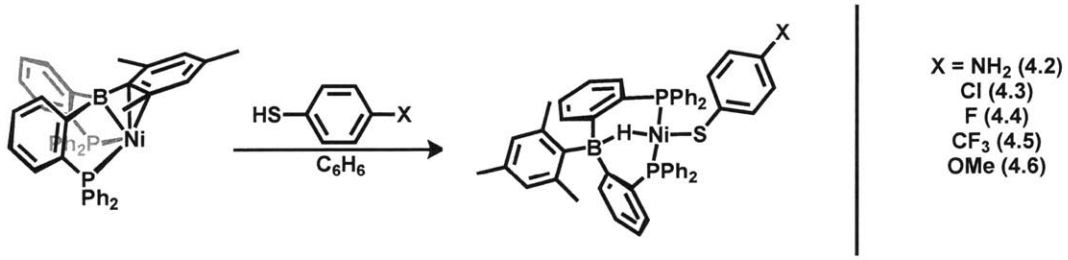

Scheme 4.4 Preparation of *para*-substituted thiolate complexes **4.2** – **4.6**.

	X	^{1}H ppm (m)	$^{31}P\{^{1}H\}$ ppm (m)	$^{11}B\{^{1}H\}$ ppm (m)
4.1	H	-12.23 (t, $^{2}J_{HP}$ = 26.1 Hz)	37.9	4.8
4.2	NH_2	-12.31 (s)	37.7	3.4
4.3	Cl	-12.34 (t, $^{2}J_{HP}$ = 26.4 Hz)	38.4	5.1
4.4	F	-12.36 (t, $^{2}J_{HP}$ = 26.2 Hz)	39.3	4.8
4.5	CF_3	-12.23 (t, $^{2}J_{HP}$ = 26.3 Hz)	40.8	5.8
4.6	OMe	-12.29 (t, $^{2}J_{HP}$ = 26.2 Hz)	37.9	4.9

Table 4.1 Comparison of the signature NMR resonances of borohydridothiolate complexes.

Single crystals of **4.4** and **4.6** were obtained and their solid-state structures determined by X-ray crystallographic analysis. Complex **4.4** crystallizes in the monoclinic space group *C*2/*c* with one molecule in the asymmetric unit; complex **4.6** crystallizes in the triclinic space group $P\bar{1}$ with one molecule in the asymmetric unit (Figure 4.3). Each complex features a nickel center in a distorted square planar geometry, with two *trans*-phosphines, a terminal thiolate ligand and a hydride bridging the nickel and boron centers. Overall, the structural parameters of **4.4** and **4.6** are very similar to those of **4.1** and are summarized in

Table 4.2. The largest structural changes are those observed for the Ni−S and Ni−B distances and for the P1−Ni−P2 angles. Upon moving to a more electron-withdrawing substituent on the thiolate ligand, the Ni−S distance increases (2.1856(3) Å vs 2.2023(3) Å vs 2.1524(6) Å for **4.6**, **4.1** and **4.4**, respectively) and the Ni−B distance decreases (2.551(1) Å vs 2.511(1) Å vs 2.488(2) Å for **4.6**, **4.1** and **4.4**, respectively). The P1−Ni−P2 angles expand slightly upon moving from a more electron-donating to electron-withdrawing substituent with angles of 159.56(1)°, 160.16(1)° and 165.60(2)° for **4.6**, **4.1** and **4.4**, respectively.

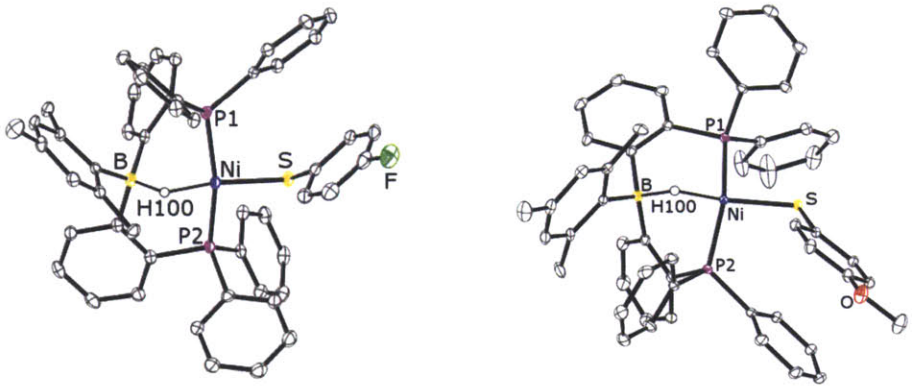

Figure 4.3 Solid-state structures of **4.4** (*left*) and **4.6** (*right*). Thermal ellipsoids are drawn at 40% probability. Solvent molecules and hydrogen atoms except for the bridging borohydride (H100) are omitted for clarity.

Distance (Å)	**4.6**	**4.1**	**4.4**	**Angle (°)**	**4.6**	**4.1**	**4.4**
Ni−P_{avg}	2.1615(3)	2.1804(3)	2.1755(6)	P1−Ni−P2	159.56(1)	160.16(1)	165.60(2)
Ni−S	2.1567(3)	2.1782(3)	2.1858(6)	P1−Ni−H100	88.59(6)	89.08(6)	87.36(6)
Ni−H100	1.549(6)	1.504(6)	1.592(6)	P2−Ni−H100	84.49(6)	86.87(6)	84.78(6)
Ni−B	2.551(1)	2.511(1)	2.488(2)	P1−Ni−S	90.81(1)	91.32(1)	98.82(2)
B−H100	1.254(6)	1.356(6)	1.257(6)	P2−Ni−S	99.02(1)	97.55(1)	90.57(2)

Table 4.2 Comparison of selected bond lengths (Å) and angles (°) for **4.6**, **4.1** and **4.4**.

The UV-vis spectra of the borohydridothiolate complexes were recorded in C_6H_6 at room temperature and are summarized in Table 4.3. All seven spectra yielded similar charge transfer bands between 600 and 650 nm and exhibit only a slight red-shift upon

moving to more electron-withdrawing substituents in the para position of the thiolate. The order parallels the relative electron-rich character of the aryl π system, consistent with S−Ni (p)π-(d)π^* LMCT character. The small red-shift in the charge transfer band suggests, as did the similar NMR spectroscopic features, that the borohydridothiolate complexes share a common ground state structure.

	R	λ_{max} (nm)
4.1	H	630
4.2	NH_2	659
4.3	Cl	610
4.4	F	615
4.5	CF_3	600
4.6	OMe	635

Table 4.3 Maximum absorption wavelengths in the UV-vis spectra of the nickel borohydrido-thiolate complexes in C_6H_6 **4.1** – **4.6**.

The distinct LMCT band for each complex offers a spectroscopic handle and the opportunity to monitor the kinetics of S−H bond activation by UV-vis spectroscopy. However, cleavage of the S−H bond to yield the borohydridothiolate complex is extremely rapid, even at −80 °C, precluding a kinetics analysis.

4.4 Isolation of a Nickel(I) Borohydridothiolate Complex

A large number of square planar nickel(II) dithiolate/thioether compounds with S, (N,S), (P,S) and (O, S) donor ligands have been described and their structural, electronic and redox properties studied in depth (Figure 4.4).[30] Such complexes generally have rich electrochemistry, and both nickel(I) and nickel(III) species have been prepared in situ and studied by EPR spectroscopy.[30–32,35] The cyclic voltammograms of the complexes shown in Figure 4.4 each feature reversible or quasi-reversible reduction features assigned as a reduction from nickel(II) to nickel(I) (A: −1.50 V; B: −1.59 V; C: −1.56 V; D: ca. −1.60 V; vs Fc/Fc^+).[36–39] EPR spectroscopic analysis confirms the assignment of the metal-based reduction, as the spectra each exhibit feature anisotropic g-values and g_{iso} values greater

than 2. In addition, $g_{\|} > g_{\perp}$, similar to most other $S = 1/2$ nickel(I) complexes. None of these species have been structurally characterized, as synthetic nickel(I) thiolate complexes tend to be unstable with respect to disproportionation to nickel(II) and nickel(0) species.[40]

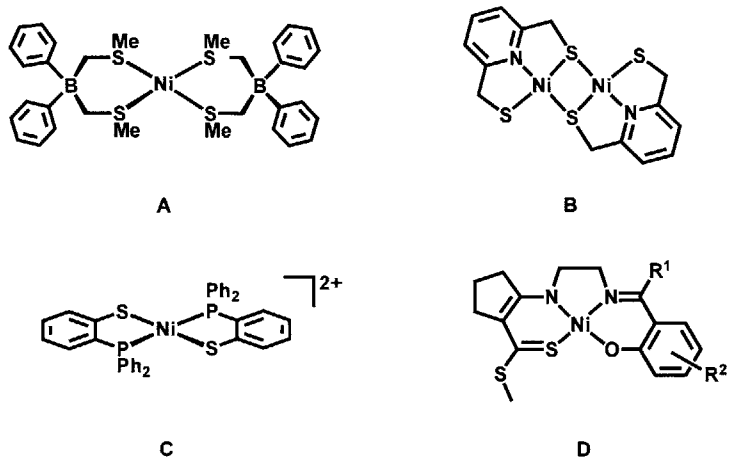

Figure 4.4 Examples of square-planar nickel(II) dithiolate/thioether complexes with various donors in the coordination sphere: S_4 (**A**);[36] NS_3 (**B**);[37] P_2S_2 (**C**);[38] ON_2S (**D**).[39]

The cyclic voltammogram of **4.1** in THF exhibits two redox features: a quasi-reversible event centered at -1.61 V vs Fc/Fc^+ and a second, irreversible event centered at ca. -2.60 V vs Fc/Fc^+. The quasi-reversible feature, assigned as the reduction of **4.1** from Ni(II) to Ni(I), is shown in Figure 4.5. At 100 mV/s, $\Delta E_P \approx 200$ mV and increases with decreasing scan rate. Even though a plot of i_P vs $v^{1/2}$ is linear, i_{Pc}/i_{Pa} is not equal to 1, further illustrating that this redox event is not a reversible feature. The Ni(II)/Ni(I) reduction potential observed here is similar to other square planar nickel complexes ligated by sulfur-containing ligands.[35] For example, the dinuclear (pyridine-2,6-dimethanethiolato)nickel(II) complex $[Ni(pmt)]_2$ reported by Holm is reduced at -1.21 V vs SCE in DMF (-1.59 V vs Fc/Fc^+).[37] In contrast, the Ni(II)/Ni(I) couple of the related pseudotetrahedral tris(phosphine)borate complex $[PhBP_3^{Ph}]Ni(S\text{-}p\text{-}^tBuPh)$ reported by Peters is shifted ca. 500 mV anodically, at -1.12 V vs Fc/Fc^+.[41] The irreversible Ni(II)/Ni(I) couple of [NiL] (L^{2-} = 2,2'-(2,2'-bipyridine-6,6'-diyl)bis(1,1-diphenylethanethiolate)) reported by Collomb is shifted 300 mV cathodically, at -1.91 V vs Fc/Fc^+.[42]

The reduced complex, $[[^{Mes}DPB^{Ph}](H)Ni(SPh)][CoCp_2^*]$ (**4.7**), was accessed by reduction of a toluene solution of **4.1** with 1.1 equiv $CoCp_2^*$, as shown in Figure 4.5. This brown,

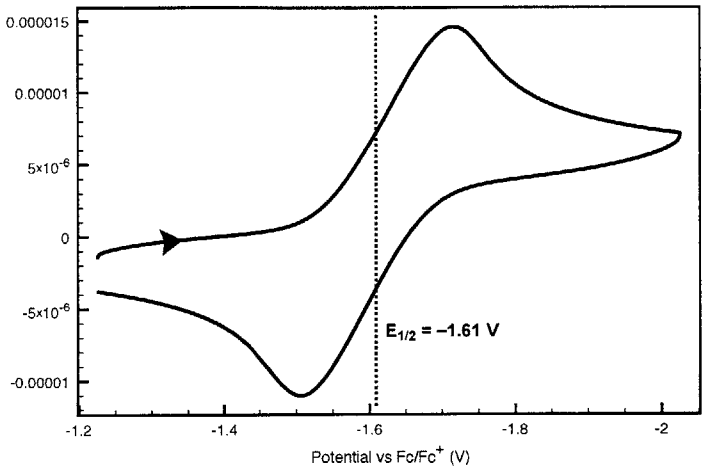

Figure 4.5 Cyclic voltammogram of neutral nickel borohydridothiolate complex **4.1** (0.4 M $[^nBu_4N][PF_6]$, THF, scan rate = 100 mV/s).

paramagnetic species features broad ^1H NMR resonances from 13 to 0 ppm. The IR spectrum of **4.7** displays a broad feature at 1954 cm^{-1} corresponding to the B–H stretch. As mentioned above, nickel(I) thiolate complexes are generally unstable, disproportionating to a mixture of nickel(II) and nickel(0) species.[35] In marked contrast, **4.7** is stable at room temperature in THF solution for at least 3 days.

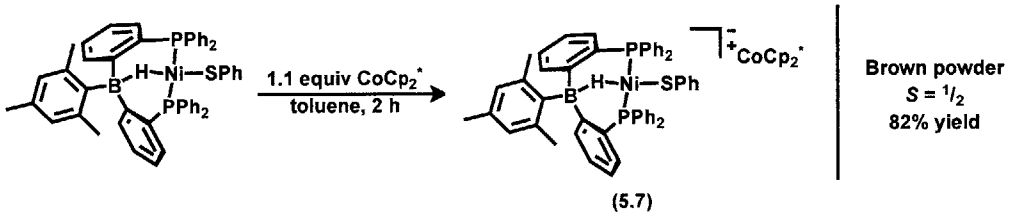

Scheme 4.5 Preparation of the anionic nickel(I) borohydridothiolate complex **4.7**.

Complex **4.7** crystallizes in the orthorhombic space group $P2_12_12_1$, with one molecule in the asymmetric unit (Figure 4.6). In comparison to **4.1**, the nickel center of **4.7** is much more distorted from ideal square planar geometry, with a P1–Ni–P2 of 119.97(3)° and S–Ni–H100 angle of 136.79(3)°. The nickel center lies 0.397 Å outside the P1–S–P2 plane. The geometry at nickel is best described as intermediate between tetrahedral and trigonal pyramidal, with a τ value of 0.54, where τ = 0 or 1 for a tetrahedron or trigonal pyramid, respectively.[43] The average Ni–P distance is 2.1990(7) Å, consistent with

other structurally characterized, four-coordinate nickel(I) phosphine complexes (2.20 – 2.28 Å).[41,44–48] The Ni–S distance lengthens ca. 0.03 Å (2.1782(3) Å vs 2.2083(8) Å) and the Ni–S–C angle expands ca. 20° (99.77(3)° vs 117.8(1)°) upon reduction of **4.1** to **4.7**. Reported in 2009 by Tatsumi, Ni(S-2,6-dimesitylphenyl)(PPh_3) is the only other structurally characterized example of a mononuclear nickel(I) thiolate complex.[49] In the solid-state structure of Ni(S-2,6-dimesitylphenyl)(PPh_3), the nickel is in a distorted square planar geometry and is coordinated by PPh_3 and the thiolate. There is also an η^2-mesityl interaction with one of the mesityl groups. The Ni–S distance is 2.2378(7) Å and is ca. 0.03 Å longer than that observed for **4.7**.

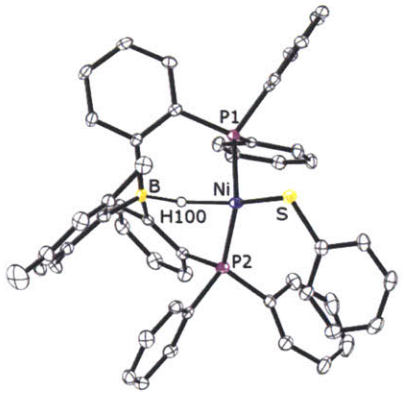

Selected Bond Lengths (Å) and Angles(°)
Ni–P1 = 2.1927(7)
Ni–P2 = 2.2052(7)
Ni–S = 2.2083(8)
Ni–H100 = 1.50(1)
Ni–B = 2.511(1)
B–H100 = 1.36(2)
P1–Ni–P2 = 160.16(1)
S–Ni–H100 = 165.1(6)

Figure 4.6 Solid-state structure of **4.7**. Thermal ellipsoids are drawn at 40% probability. Counterion and hydrogen atoms except for the bridging borohydride (H100) are omitted for clarity.

The X-band EPR spectrum of a dilute sample of **4.7**, recorded in 2-MeTHF at 10 K, is shown in Figure 4.7 (left). The EPR signal is rhombic, with *g*-values of 2.262, 2.245 an 1.995 (g_{iso} = 2.17). These values are consistent with other Ni(I) complexes having an S = 1/2 ground state with an unpaired electron occupying a predominantly $d_{x^2-y^2}$ orbital.[50–58] The anisotropy of the *g*-values in the spectrum of **4.7** (Δg = 0.27) and the g_{iso} value of 2.17 indicate significant metalloradical character, as opposed to ligand radical character. A single point energy calculation on **4.7** supports this interpretation, with a Mulliken spin density of 0.83 on nickel, 0.13 on boron and 0.07 on sulfur. (Figure 4.7, right).

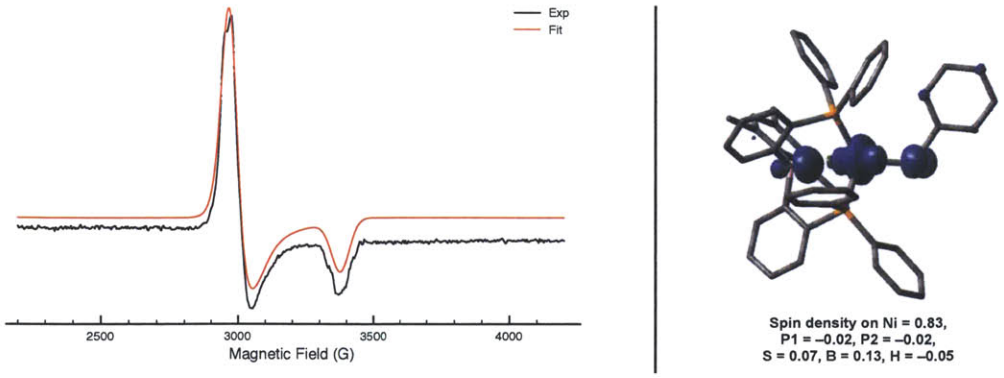

Figure 4.7 (*left*) Experimental (black) and simulated (red) X-band EPR spectrum of **4.7** (2-MeTHF at 10 K). Simulated parameters: $g_1 = 2.262$, $g_2 = 2.245$, $g_3 = 1.995$; $\sigma_{g_1} = 0.045$, $\sigma_{g_2} = 0.089$, $\sigma_{g_3} = 0.046$. (*right*) Spin density surface calculated for **4.7** (DFT, Gaussian 09, M06L/6-311+G(d,p), isovalue = 0.002).

4.5 Ni K-Edge XAS Studies

Seeking to gather more information about the unusual nickel(I) borohydridothiolate species **4.7**, Ni K-edge XAS spectra were collected in collaboration with Professor Kyle Lancaster (Cornell University). Figure 4.8 shows the normalized Ni K-edge XAS spectra obtained for **4.1** and **4.7**. The edge energy for the **4.1** spectrum is 8339.2(2) eV, which is similar to other nickel(II) species bound to ligands containing one or two sulfur-donor atoms.[59–61] The intense pre-edge peak at 8334.9 eV is assigned to the 1s→4p$_z$ transition and is characteristic of four-coordinate planar nickel complexes.[61,62] Spectra obtained for planar nickel complexes tend to exhibit a weak 1s→3d transition at ca. 8330 eV. However, combination of the weak 1s→3d absorption and the low edge energy associated with planar nickel complexes with S-donor ligands frequently obscures the pre-edge peak attributed to this transition.[61] Accordingly, the Ni K-edge spectrum of **4.1** does not feature a resolved maximum for the 1s→3d transition. Upon reduction of **4.1** to **4.7**, the edge energy shifts ca. 0.5 eV to 8338.7(2) eV. The pre-edge peak corresponding to the 1s→4p$_z$ transition is diminished relative to that of **4.1**, indicative of a deviation from a planar geometry toward a non-planar configuration.[61,62] This geometric distortion is consistent with the changes observed in the solid-state structures of **4.1** and **4.7** (vide supra). A very small shoulder at ca.

8332 eV is present in the spectrum of **4.7** that could correspond to the 1s→3d transition, however resolution of this peak is complicated by its proximity to the more intense, low energy pre-edge feature. The Ni K-edge energy has been shown to vary systematically with the charge residing on the nickel center.[61–63] That the energy obtained for **4.7** is 0.5 eV less than that measured for **4.1** indicates that the nickel center in **4.7** is more electron-rich than in **4.1**, consistent with the assignment of **4.7** as a formally nickel(I) borohydridothiolate complex.[63]

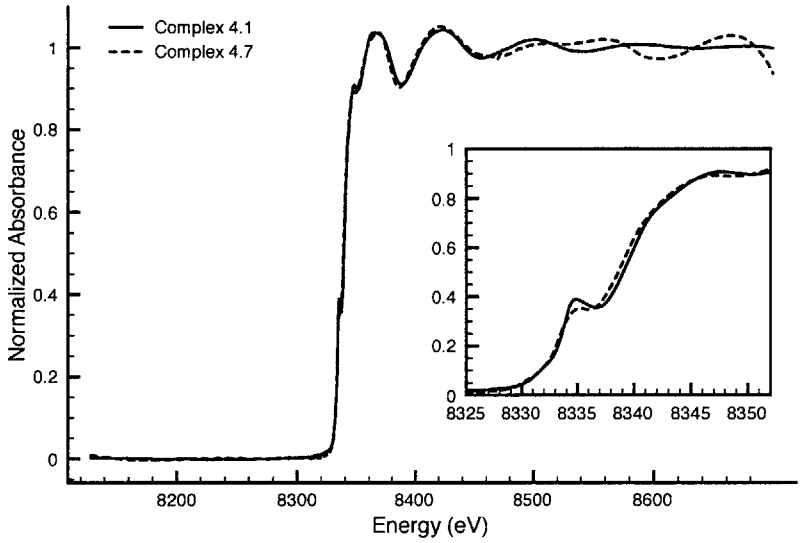

Figure 4.8 Normalized Ni K-edge XAS spectra obtained for **4.1** (solid line) and **4.7** (dashed line). The inset shows the edge region between 8325 and 8350 eV.

4.6 Conclusions and Future Work

In this chapter, the preparation of a series of nickel borohydridothiolate complexes by S–H bond activation of arylthiols was described. Such species are rare; accordingly, there are only two nickel hydride thiolate complexes characterized by X-ray crystallographic analysis reported in the literature. The complexes communicated in this chapter comprise the only other examples of structurally characterized nickel hydride thiolate complexes. The UV-vis spectra of the borohydridothiolate complexes each exhibit a charge transfer band that shifts to slightly lower energy upon moving from electron-withdrawing to electron-

donating substituents in the *para* position of the thiolate ligand. This observation is consistent with S–Ni (p)π-(d)$\pi^{\star}$ character.

A formally nickel(I) borohydridothiolate complex was accessed by reduction of the nickel(II) borohydridothiolate with $CoCp_2^{\star}$. The EPR spectrum of this anionic species is consistent with an S = 1/2 ground state complex and an unpaired electron residing in the $d_{x^2-y^2}$ orbital. Although a number of examples of nickel(I) thiolate complexes have been prepared by in situ reduction, they are unstable to decomposition by comproportionation. In marked contrast, the nickel(I) borohydridothiolate species described in this chapter is isolable and is the second example of a structurally characterized nickel(I) thiolate complex.

As EPR spectroscopy has been an important tool in the identification of odd-electron enzyme intermediates, a logical advance would be the preparation of discrete nickel thiolate complexes with odd-electron nickel(I) or nickel(III) oxidation states for comparison. The nickel(I) borohydridothiolate complex described in this chapter is a rare example of a well-defined nickel(I) thiolate species and, within the context of odd-electron enzymatic intermediate characterization, would be of obvious interest to study in depth by various spectroscopic techniques. Sulfur K-edge X-ray absorption spectroscopy (XAS) in particular will be an important experiment, as this technique is a direct probe of ligand-metal bond covalency.[64] In addition to spectroscopic studies, the reactivity of the reduced nickel thiolate complex with biologically relevant small molecule substrates should prove to be a rich avenue of research, as the [^{Mes}DPB^{Ph}]Ni core has a demonstrated ability to mediate catalytic reactions (see Chapter 3).

4.7 Experimental Methods

4.7.1 General Considerations

All manipulations were carried out using standard Schlenk or glovebox techniques under a dinitrogen atmosphere. Unless otherwise noted, solvents were dried and deoxygenated by sparging with argon and passing through activated alumina in a solvent purification system

from SG Waters USA, LLC (Nashua, NH). Non-halogenated solvents were tested with a standard purple solution of sodium benzophenone ketyl in tetrahydrofuran in order to confirm effective oxygen and moisture removal. **3.1**[33] was prepared according to literature methods. All other reagents were purchased from commercial suppliers and used without further purification. Elemental analyses were performed by Midwest Microlab, LLC (Indianapolis, IN) and Robertson Microlit Laboratories, Inc (Ledgewood, NJ). Deuterated solvents were purchased from Cambridge Isotope Laboratories, Inc., degassed, and dried over activated 3-Å molecular sieves prior to use.

4.7.2 Spectroscopic Measurements

Varian 300, 400 and 500 MHz spectrometers were used to record ^{1}H, ^{13}C, ^{31}P and ^{11}B NMR spectra at room temperature, unless otherwise noted. ^{1}H and ^{13}C NMR chemical shifts were referenced to the residual solvent peaks. ^{31}P NMR chemical shifts were referenced to external 85% phosphoric acid (δ = 0 ppm). ^{11}B NMR chemical shifts were referenced to external $BF_3 \cdot Et_2O$ (δ = 0 ppm). Optical spectroscopy measurements were taken on a Cary 50 UV-vis spectrophotometer using a 1 cm two-window quartz cell sealed with a closed cap (Starna Cells, Inc, Altascadero, CA). Infrared measurements were obtained in thin films using a Bruker ALPHA FT-IR spectrometer equipped with a diamond ATR probe and OPUS/Mentor software. X-band EPR spectra were recorded using a Bruker EMX spectrometer at 77 K in 2-MeTHF glasses. EPR samples were prepared in a glovebox under an N_2 atmosphere in quartz EPR tubes equipped with J. Young caps. EPR spectra were simulated using EasySpin.[65]

4.7.3 Electrochemistry

Electrochemical measurements were carried out in a glovebox under a dinitrogen atmosphere in a one-compartment cell using a CH Instruments 630-C Electrochemistry Analyzer with CHI Version 8.09 software package. A glassy carbon electrode and platinum wire were used as the working and auxiliary electrodes, respectively. The reference electrode was $Ag/AgNO_3$ in THF. Solutions of electrolyte (0.4 M $[^{n}Bu_4N][PF_6]$) and analyte

were prepared in a glovebox. Experiments were conducted at room temperature. The ferrocene couple Fc/Fc^+ was used as an external reference.

4.7.4 X-ray Spectroscopy

Ni K-edge XAS was measured at the Stanford Synchrotron Radiation Lightsource at beam line 7-3 under ring conditions of 3 GeV and 500 mA. A Si(220) double-crystal monochromator was used for energy selection and a Rh-coated mirror (set to an energy cutoff of 13 keV) was used for harmonic rejection. Internal energy calibration was performed by assigning the first inflection point of a Ni foil spectrum to 8333 eV. Data were collected in transmission mode (using N_2-filled ionization chambers placed immediately up and downstream of the sample) on powdered samples suspended in boron nitride with the sample maintained at 10 K in an Oxford liquid helium flow cryostat. Scans were averaged and processed using the MAVE and PROCESS modules of the EXAFSPAK[66] software package.

4.7.5 DFT Calculations

Calculations for **4.7** were performed using the Gaussian09 suite of programs.[67] Single point calculations were performed with the M06L functional[68] and the 6-311+G(d,p) basis set for all atoms. The Mulliken spin densities calculated for **4.7** are summarized in Table 4.4.

Atom	Value	Atom	Value
Ni	0.830088	P	−0.015337
B	0.134412	P	−0.018661
S	0.069245	–	–

Table 4.4 Mulliken spin densities calculated for **4.7**. For clarity, only the values for the heteroatoms are shown.

4.7.6 Preparation of [^{Mes}DPB^{Ph}](H)Ni(SPh) (4.1)

To a solution of **3.1** (42.4 mg, 59.6 μmol) in C_6H_6 (1 mL) was added neat HSPh (7.8 μL, 76.3 μmol). The resulting green solution was stirred 6 h at room temperature, frozen

and lyophilized. Crystalline material was obtained by vapor diffusion of $O(SiMe_3)_2$ into a concentrated toluene solution. The crystals were separated from the mother liquor, washed with $O(SiMe_3)_2$ and dried in vacuo (42.2 mg, 86%). Crystals suitable for X-ray analysis were grown by the same method. ^{1}H NMR (400 MHz, C_6D_6) δ 7.80 (s, 4H), 7.47 (dd, J = 7.6, 1.8 Hz, 2H), 7.41 (dd, J = 7.2, 1.5 Hz, 2H), 7.36 – 7.17 (m, 4H), 7.17 – 7.05 (m, 5H), 7.05 – 6.80 (m, 8H), 6.76 (t, J = 7.5 Hz, 4H), 6.61 – 6.50 (m, 2H), 6.45 (dd, J = 8.2, 6.9 Hz, 2H), 6.32 (s, 2H), 2.05 (d, J = 15.5 Hz, 3H), 1.81 (s, 6H), −12.23 (t, J = 26.1 Hz, 1H). $^{13}C\{^1H\}$ NMR (101 MHz, C_6D_6) δ 146.7, 146.6, 146.5, 140.9, 134.8, 134.7, 134.7, 134.3, 134.2, 133.8, 133.6, 133.5, 133.5, 132.7, 131.7, 130.0, 129.8, 129.4, 129.2, 128.9, 126.4, 126.4, 126.3, 126.3, 122.3, 25.4, 20.5. $^{31}P\{^1H\}$ NMR (162 MHz, C_6D_6) δ 37.9 (s). $^{11}B\{^1H\}$ NMR (128 MHz, C_6D_6) δ 4.8. UV-Vis (ε, THF, nm $cm^{-1}M^{-1}$): 630 {333}. Anal. Calcd for $C_{51}H_{45}BNiP_2S$: C, 74.57; H, 5.52. Found: C, 74.35; H, 5.47.

4.7.7 In situ Preparation of a Series of Borohydridothiolate Complexes (4.2 – 4.6)

For each reaction, 1.2 equiv of the appropriate thiol was added to a room temperature C_6H_6 solution (2 mL) of **3.1**. The resulting solution was stirred for 2 h, frozen and lyophilized. Characterization data for each are outlined below:

[^{Mes}DPB^{Ph}](H)NiS(*p*-$NH_2C_6H_4$) (**4.2**): ^{1}H NMR (400 MHz, C_6D_6) δ 10.40 (br s, 2H), 7.95 (s, 4H), 7.52 (d, J = 7.5 Hz, 2H), 7.41 (s, J = 5.9 Hz, 6H), 7.27 (s, 4H), 7.10 – 6.90 (m, 10H), 6.90 – 6.84 (m, 4H), 6.38 (s, 2H), 5.72 (d, J = 7.8 Hz, 2H), 2.09 (s, 3H), 1.90 (s, 6H), −12.31 (s, 1H). $^{13}C\{^1H\}$ NMR (101 MHz, C_6D_6) δ 163.1, 145.7, 143.8, 142.9, 141.0, 137.6, 134.7, 134.2, 133.9, 133.7, 133.1, 131.7, 129.8, 129.7, 129.4, 129.2, 129.1, 128.2, 126.3, 115.3, 115.2, 113.7, 25.6, 25.5. $^{31}P\{^1H\}$ NMR (162 MHz, C_6D_6) δ 37.7 (s). $^{11}B\{^1H\}$ NMR (128 MHz, C_6D_6) δ 3.4. UV-Vis (ε, THF, nm): λ_{max} = 659.

[^{Mes}DPB^{Ph}](H)NiS(*p*-ClC_6H_4) (**4.3**): ^{1}H NMR (400 MHz, C_6D_6) δ 7.88 (s, 4H), 7.53 – 7.45 (m, 2H), 7.25 (dd, J = 11.7, 8.0 Hz, 8H), 7.13 (s, 2H), 7.07 – 6.82 (m, 10H), 6.79 (d, J = 7.5 Hz, 4H), 6.46 (d, J = 8.3 Hz, 2H), 6.35 (s, 2H), 2.07 (s, 3H), 1.81 (s, 6H), −12.34 (t, J = 26.4 Hz, 1H). $^{13}C\{^1H\}$ NMR (101 MHz, C_6D_6) δ 162.8, 145.4, 140.9, 134.7, 134.5,

134.3, 134.1, 133.8, 133.7, 133.6, 133.5, 133.5, 131.6, 130.1, 130.0, 129.6, 129.3, 129.2, 128.4, 128.2, 128.1, 127.9, 127.7, 127.4, 126.5, 126.3, 126.2, 25.4, 20.6. $^{31}P\{^{1}H\}$ NMR (162 MHz, C_6D_6) δ 38.4 (s). $^{11}B\{^{1}H\}$ NMR (128 MHz, C_6D_6) δ 5.1. UV-Vis (ε, C_6H_6, nm): $\lambda_{max} = 610$.

[^{Mes}DPB^{Ph}](H)NiS(*p*-FC_6H_4) (**4.4**): X-ray quality crystals were grown by vapor diffusion of $O(SiMe_3)_2$ into a concentrated toluene solution at −35 °C. ^{1}H NMR (400 MHz, C_6D_6) δ 7.89 (s, 4H), 7.54 – 7.46 (m, 2H), 7.24 (dd, J = 8.4, 5.5 Hz, 8H), 7.13 (s, 1H), 7.06 – 6.90 (m, 9H), 6.90 – 6.73 (m, 6H), 6.36 (s, 2H), 6.19 (t, J = 8.7 Hz, 2H), 2.07 (s, 3H), 1.84 (s, 6H), −12.36 (t, J = 26.2 Hz, 1H). $^{13}C\{^{1}H\}$ NMR (75 MHz, C_6D_6) δ 162.7, 140.6, 134.2, 133.4, 133.3, 133.3, 133.2, 129.8, 129.7, 129.3, 129.0, 127.9, 127.9, 127.8, 127.7, 127.39, 127.2, 127.1, 126.2, 113.0, 112.7, 25.2, 20.3. $^{31}P\{^{1}H\}$ NMR (121 MHz, C_6D_6) δ 39.3 (s). $^{11}B\{^{1}H\}$ NMR (128 MHz, C_6D_6) δ 4.8. UV-Vis (ε, C_6H_6, nm): λ_{max} = 615.

[^{Mes}DPB^{Ph}](H)NiS(*p*-$CF_3C_6H_4$) (**4.5**): ^{1}H NMR (400 MHz, C_6D_6) δ 7.86 (s, 3H), 7.48 (s, 2H), 7.35 (s, 3H) 7.25 (s, 5H), 7.07 – 6.86 (m, 10H), 6.76 (s, 7H), 6.64 (s, 3H), 6.35 (s, 2H), 2.06 (s, 3H), 1.81 (s, 5H), −12.23 (t, J = 26.3 Hz, 1H). $^{13}C\{^{1}H\}$ NMR (75 MHz, C_6D_6) δ 163.3, 141.5, 136.1, 135.1, 134.8, 133.5, 133.2, 131.8, 131.5, 129.6, 129.3, 127.2, 124.2, 25.3, 21.74. $^{31}P\{^{1}H\}$ NMR (121 MHz, C_6D_6) δ 40.8 (s). $^{19}F\{^{1}H\}$ NMR (376 MHz, C_6D_6) δ −61.0. $^{11}B\{^{1}H\}$ NMR (128 MHz, C_6D_6) δ 5.8. UV-Vis (ε, C_6H_6, nm): $\lambda_{max} = 600$.

[^{Mes}DPB^{Ph}](H)NiS(*p*-$OMeC_6H_4$) (**4.6**): X-ray quality crystals were grown by vapor diffusion of $O(SiMe_3)_2$ into a concentrated toluene solution at −35 °C. ^{1}H NMR (400 MHz, C_6D_6) δ 7.94 (s, 4H), 7.57 – 7.48 (m, 2H), 7.37 (d, J = 6.4 Hz, 4H), 7.32 – 7.23 (m, 4H), 7.14 – 7.10 (m, 2H), 7.06 – 6.86 (m, 10H), 6.83 (t, J = 7.5 Hz, 4H), 6.37 (s, 2H), 6.14 (d, J = 8.6 Hz, 2H), 3.16 (s, 3H), 2.08 (s, 3H), 1.89 (s, 6H), −12.29 (t, J = 26.2 Hz, 1H). $^{13}C\{^{1}H\}$ NMR (101 MHz, C_6D_6) δ 156.6, 140.9, 136.6, 134.7, 134.4, 134.3, 133.8, 131.7, 129.9, 129.8, 129.5, 129.2, 129.1, 128.2, 128.0, 128.0, 127.9, 127.7, 127.5, 127.4, 126.3, 112.5, 112.4, 54.4, 54.4, 25.5, 20.6, 20.5. $^{31}P\{^{1}H\}$ NMR (162 MHz, C_6D_6) δ 37.9 (s). $^{11}B\{^{1}H\}$ NMR (128 MHz, C_6D_6) δ 4.9. UV-Vis (ε, C_6H_6, nm): λ_{max} = 635.

4.7.8 Preparation of [[^{Mes}DPB^{Ph}](H)Ni(SPh)][$CoCp_2^*$] (4.7)

To a solution of **4.1** (69.9 mg, 85.10 μmol) in toluene (1 mL) was added a toluene slurry of $CoCp_2^*$ (28.1 mg, 85.31 μmol). The resulting brown slurry was stirred for 4 hr at room temperature and then filtered to collect the brown solids. The solids were dissolved in THF and filtered through Celite to remove a small amount of black solids. Crystalline material was obtained by vapor diffusion of pentane into a concentrated THF solution. The crystals were separated from the mother liquor, washed with pentane and dried in vacuo (80.3 mg, 82%). Crystals suitable for X-ray analysis were grown by the same method. ^{1}H NMR (400 MHz, THF-d_8) δ 11.9, 10.0, 7.5, 5.9, 2.1, 1.2. Anal. Calcd for $C_{71}H_{75}BCoNiP_2S \cdot 2\,THF$: C, 73.27; H, 7.08. Found: C, 72.76; H, 6.75. IR (ATR, THF film, cm^{-1}): 1954.

4.7.9 X-ray Crystallographic Details

Single crystals of **4.1**, **4.4** and **4.6** were obtained by vapor diffusion of $O(SiMe_3)_2$ into a concentrated toluene solution either at room temperature or -35 °C, crystals of **4.7** were grown by vapor diffusion of pentane into a concentrated THF solution. Low-temperature single crystal X-ray diffraction studies were carried out at the Beckman Institute Crystallography Facility on a Bruker Kappa Apex II diffractometer with Mo Kα radiation (λ = 0.71073 Å). Crystals were coated with Paratone-N oil and mounted on glass fibers. Structures were solved by direct or Patterson methods using SHELXS[69] and refined against F2 on all data by full-matrix least squares with SHELXL-97[70] using established refinement techniques.[71] All non-hydrogen atoms were refined anisotropically. All hydrogen atoms (except the hydrogen atoms bound to heteroatoms in **4.1** – **4.7**) were included into the model at geometrically calculated positions and refined using a riding model. The isotropic displacement parameters of all calculated hydrogen atoms were fixed to 1.2 times the U values of the atoms they are linked to (1.5 times for methyl groups). Thermal ellipsoid diagrams were created using Olex2.[72] In the structure of **4.6**, there is a disordered half molecule of toluene. The crystallographic details for **4.1** – **4.7** are summarized in Tables 4.5 and 4.6.

	4.1	**4.4** · C_7H_8
Formula	$C_{51}H_{45}BNiP_2S$	$C_{58}H_{52}BFNiP_2S$
Formula Weight	821.39	941.08
Temperature/K	100(2)	100(2)
Crystal syst.	Monoclinic	Monoclinic
Space group	$P2_1$	$C2/c$
Color	Green	Green
a/Å	11.9606(7)	38.8257(14)
b/Å	12.8325(8)	11.6103(4)
c/Å	14.1437(8)	22.1039(8)
α/°	90	90
β/°	107.586(3)	111.914(2)
γ/°	90	90
V/^{3}	2069.4(2)	9244.0(6)
ρ (calc.)/(gcm^{-1})	1.318	1.339
Z	2	8
No. refl.	90165	115114
No. unique refl.	12684	14125
R_{int}	0.0353	0.0785
R_1 (all data)[a]	0.0209	0.0779
wR_2 (all data)[b]	0.0516	0.1308
R_1 [(I >2σ)]	0.0200	0.0477
wR_2 [(I >2σ)]	0.0510	0.1153
GOF[c]	1.048	1.031
Flack param.	0.146(4)	–

Table 4.5 Crystallographic summary for **4.1** and **4.4**. [a]$R_1 = \Sigma||F_0 - |F_e||/\Sigma|F_0|$. [b]$wR_2 = (\Sigma[w(F_0^2 - F_e^2)^2]/\Sigma[w(F_0^2)^2])^{1/2}$. [c]$GOF = (\Sigma[w(F_0^2 - F_e^2)^2]/(n-p))^{1/2}$ where n is the number of data and p is the number of parameters refined.

	4.6 · 0.5 C_7H_8	**4.7**
Formula	$C_{55.50}H_{51}BNiOP_2S$	$C_{71}H_{75}BCoNiP_2S$
Formula Weight	897.48	1150.76
Temperature/K	100(2)	100(2)
Crystal syst.	Triclinic	Orthorhombic
Space group	$P\bar{1}$	$P2_12_12_1$
Color	Green	Brown
a/Å	10.9476(5)	12.8818(8)
b/Å	11.5830(6)	17.1316(9)
c/Å	19.4711(10)	27.2404(19)
α/°	74.660(2)	90
β/°	77.634(2)	90
γ/°	72.866(2)	90
V/^{3}	2250.42(19)	6011.6(6)
ρ (calc.)/(gcm^{-1})	1.324	1.271
Z	2	4
No. refl.	126044	14971
No. unique refl.	25464	12378
R_{int}	0.0380	0.0636
R_1 (all data)[a]	0.0479	0.0.0589
wR_2 (all data)[b]	0.0956	0.0828
R_1 [(I >2σ)]	0.0350	0.0407
wR_2 [(I >2σ)]	0.0889	0.0760
GOF[c]	1.036	1.020

Table 4.6 Crystallographic summary for **4.6** and **4.7**. [a]$R_1 = \Sigma||F_0 - |F_e||/\Sigma|F_0|$. [b]$wR_2 = (\Sigma[w(F_0^2 - F_e^2)^2]/\Sigma[w(F_0^2)^2])^{1/2}$. [c]$GOF = (\Sigma[w(F_0^2 - F_e^2)^2]/(n-p))^{1/2}$ where n is the number of data and p is the number of parameters refined.

4.8 Bibliography

[1] Malyshev, D. A.; Scott, N. M.; Marion, N.; Stevens, E. D.; Ananikov, V. P.; Beletskaya, I. P.; Nolan, S. P. *Organometallics* **2006**, *25*, 4462–4470.

[2] Back, T. G.; Krishna, M. V. *J. Org. Chem.* **1988**, *53*, 2533–2536.

[3] Ichinose, Y.; Wakamatsu, K.; Nozaki, K.; Birbaum, J.-L.; Oshima, K.; Utimoto, K. *Chem. Lett.* **1987**, 1647–1650.

[4] Griesbaum, K. *Angew. Chem. Int. Ed.* **1970**, *9*, 273–287.

[5] Truce, W. E.; Heine, R. F. *J. Am. Chem. Soc.* **1957**, *79*, 5311–5313.

[6] Truce, W. E.; Simms, J. A. *J. Am. Chem. Soc.* **1956**, *78*, 2756–2759.

[7] Metzner, P.; Thuiller, A. *Sulfur Reagents in Organic Synthesis*; Academic Press: London, 1994.

[8] Zwanenburg, B., Klunder, A. J. H., Eds. *Perspectives in the Organic Chemistry of Sulfur*; Elsevier: Amsterdam, 1987.

[9] Beller, M.; Seayad, J.; Tillack, A.; Jiao, H. *Angew. Chem. Int. Ed.* **2004**, *43*, 3368–3398.

[10] Alonso, F.; Beletskaya, I. P.; Yus, M. *Chem. Rev.* **2004**, *104*, 3079–3159.

[11] Ogawa, A. *J. Organomet. Chem.* **2000**, *611*, 463–474.

[12] Kondo, T.; Mitsudo, T. *Chem. Rev.* **2000**, *100*, 3205–3220.

[13] Castarlenas, R.; Di Giuseppe, A.; Pérez-Torrente, J. J.; Oro, L. A. *Angew. Chem. Int. Ed.* **2013**, *52*, 211–222.

[14] Ogawa, A.; Ikeda, T.; Kimura, K.; Hirao, T. *J. Am. Chem. Soc.* **1999**, *121*, 5108–5114.

[15] Kuniyasu, H.; Ogawa, A.; Sato, K.-I.; Ryu, I.; Kambe, N.; Sonoda, N. *J. Am. Chem. Soc.* **1992**, *114*, 5902–5903.

[16] Ananikov, V. P.; Orlov, N. V.; Beletskaya, I. P.; Khrustalev, V. N.; Antipin, M. Y.; Timofeeva, T. V. *J. Am. Chem. Soc.* **2007**, *129*, 7252–7253.

[17] Ananikov, V. P.; Orlov, N. V.; Beletskaya, I. P. *Organometallics* **2006**, *25*, 1970–1977.

[18] Ananikov, V. P.; Malyshev, D. A.; Beletskaya, I. P.; Aleksandrov, G. G.; Eremenko, I. L. *Adv. Synth. Catal.* **2005**, *347*, 1993–2001.

[19] Di Giuseppe, A.; Castarlenas, R.; Pérez-Torrente, J. J.; Crucianelli, M.; Polo, V.; Sancho, R.; Lahoz, F. J.; Oro, L. A. *J. Am. Chem. Soc.* **2012**, *134*, 8171–8183.

[20] Shoai, S.; Bichler, P.; Kang, B.; Buckley, H.; Love, J. A. *Organometallics* **2007**, *26*, 5778–5781.

[21] Cao, C.; Fraser, L. R.; Love, J. A. *J. Am. Chem. Soc.* **2005**, *127*, 17614–17615.

[22] Ragsdale, S. W. *J. Biol. Chem.* **2009**, *284*, 18571–18575.

[23] Sigel, A., Sigel, H., Sigel, R. K. O., Eds. *Nickel and Its Surprising Impact in Nature*; John Wiley & Sons, Ltd: Chichester, UK, 2007; Vol. 2.

[24] Barondeau, D. P.; Kassmann, C. J.; Bruns, C. K.; Tainer, J. A.; Getzoff, E. D. *Biochemistry* **2004**, *43*, 8038–8047.

[25] Vignais, P. M.; Billoud, B. *Chem. Rev.* **2007**, *107*, 4206–4272.

[26] Ragsdale, S. W.; Pierce, E. *Biochim. Biophys. Acta* **2008**, *1784*, 1873–1898.

[27] Dobbek, H.; Svetlitchnyi, V.; Gremer, L.; Huber, R.; Meyer, O. *Science* **2001**, *293*, 1281–1285.

[28] Doukov, T. I.; Blasiak, L. C.; Seravalli, J.; Ragsdale, S. W.; Drennan, C. L. *Biochemistry* **2008**, *47*, 3474–3483.

[29] Doukov, T. I.; Iverson, T. M.; Seravalli, J.; Ragsdale, S. W.; Drennan, C. L. *Science* **2002**, *298*, 567–572.

[30] Bouwman, E.; Reedijk, J. *Coord. Chem. Rev.* **2005**, *249*, 1555–1581.

[31] Evans, D. J. *Coord. Chem. Rev.* **2005**, *249*, 1582–1595.

[32] Harrop, T. C.; Mascharak, P. K. *Coord. Chem. Rev.* **2005**, *249*, 3007–3024.

[33] Harman, W. H.; Peters, J. C. *J. Am. Chem. Soc.* **2012**, *134*, 5080–5082.

[34] Schaub, T.; Backes, M.; Plietzsch, O.; Radius, U. *Dalton Trans.* **2009**, 7071–7079.

[35] Nag, K.; Chakravorty, A. *Coord. Chem. Rev.* **1980**, *33*, 87–147.

[36] Ge, P.; Riordan, C. G.; Yap, G. P.; Rheingold, A. L. *Inorg. Chem.* **1996**, *35*, 5408–5409.

[37] Krüger, H. J.; Holm, R. H. *Inorg. Chem.* **1989**, *28*, 1148–1155.

[38] Kim, J. S.; Reibenspies, J. H.; Darensbourg, M. Y. *J. Am. Chem. Soc.* **1996**, *118*, 4115–4123.

[39] Pereira, E.; Gomes, L.; de Castro, B. *Inorg. Chim. Acta* **1998**, *271*, 83–92.

[40] Rosen, W.; Busch, D. H. *J. Am. Chem. Soc.* **1969**, *91*, 4694–4697.

[41] MacBeth, C. E.; Thomas, J. C.; Betley, T. A.; Peters, J. C. *Inorg. Chem.* **2004**, *43*, 4645–4662.

[42] Gennari, M.; Orio, M.; Pécaut, J.; Bothe, E.; Neese, F.; Collomb, M.-N.; Duboc, C. *Inorg. Chem.* **2011**, *50*, 3707–3716.

[43] Addison, A. W.; Rao, T. N.; Reedijk, J.; van Rijn, J.; Verschoor, G. C. *J. Chem. Soc., Dalton Trans.* **1984**, 1349–1356.

[44] Beck, R.; Shoshani, M.; Krasinkiewicz, J.; Hatnean, J. A.; Johnson, S. A. *Dalton Trans.* **2013**, *42*, 1461–1475.

[45] Mindiola, D. J.; Hillhouse, G. L. *J. Am. Chem. Soc.* **2001**, *123*, 4623–4624.

[46] Bianchini, C.; Masi, D.; Mealli, C.; Meli, A. *Cryst. Struct. Commun.* **1982**, *11*, 1475–1480.

[47] Gleizes, A.; Dartiguenave, M.; Dartiguenave, Y.; Galy, J.; Klein, H. F. *J. Am. Chem. Soc.* **1977**, *99*, 5187–5189.

[48] Dapporto, P.; Fallani, G.; Sacconi, L. *Inorg. Chem.* **1974**, *13*, 2847–2850.

[49] Ito, M.; Matsumoto, T.; Tatsumi, K. *Inorg. Chem.* **2009**, *48*, 2215–2223.

[50] Saraev, V. V.; Kraikivskii, P. B.; Matveev, D. A.; Kuzakov, A. S.; Vilms, A. I.; Fedonina, A. A. *Russ. J. Coord. Chem.* **2008**, *34*, 438–442.

[51] Saraev, V. V.; Kraikivskii, P. B.; Vilms, A. I.; Zelinskii, S. N.; Yunda, A. Y.; Danilovtseva, E. N.; Kuzakov, A. S. *Kinet. Catal.* **2007**, *48*, 778–784.

[52] Suh, M. P.; Oh, K. Y.; Lee, J. W.; Bae, Y. Y. *J. Am. Chem. Soc.* **1996**, *118*, 777–783.

[53] Bowmaker, G. A.; Williams, J. P. *J. Chem. Soc., Dalton Trans.* **1994**, 1231–1236.

[54] Bowmaker, G. A.; Williams, J. P. *J. Chem. Soc., Dalton Trans.* **1993**, 3593–3600.

[55] Suh, M. P.; Kim, H. K.; Kim, M. J.; Oh, K. Y. *Inorg. Chem.* **1992**, *31*, 3620–3625.

[56] Chmielewski, P.; Grzeszczuk, M.; Latos-Grażyński, L.; Lisowski, J. *Inorg. Chem.* **1989**, *28*, 3546–3552.

[57] Stolzenberg, A. M.; Stershic, M. T. *Inorg. Chem.* **1987**, *26*, 3082–3083.

[58] Gagné, R. R.; Ingle, D. M. *Inorg. Chem.* **1981**, *20*, 420–425.

[59] Gu, Z.; Dong, J.; Allan, C. B.; Choudhury, S. B.; Franco, R.; Moura, J. J. G.; Moura, I.; LeGall, J.; Przybyla, A. E.; Roseboom, W.; Albracht, S. P. J.; Milton, J. A.; Scott, R. A.; Maroney, M. J. *J. Am. Chem. Soc.* **1996**, *118*, 11155–11165.

[60] Bagyinka, C.; Whitehead, J. P.; Maroney, M. J. *J. Am. Chem. Soc.* **1993**, *115*, 3576–3585.

[61] Colpas, G. J.; Maroney, M. J.; Bagyinka, C.; Kumar, M.; Willis, W. S.; Suib, S. L.; Baidya, N.; Mascharak, P. K. *Inorg. Chem.* **1991**, *30*, 920–928.

[62] Furenlid, L. R.; Renner, M. W.; Fujita, E. *Phys. B* **1995**, *208*, 739–742.

[63] Tang, Q.; Carrington, P. E.; Horng, Y.-C.; Maroney, M. J.; Ragsdale, S. W.; Bocian, D. F. *J. Am. Chem. Soc.* **2002**, *124*, 13242–13256.

[64] Glaser, T.; Hedman, B.; Hodgson, K. O.; Solomon, E. I. *Acc. Chem. Res.* **2000**, *33*, 859–868.

[65] Stoll, S.; Schweiger, A. *J. Magn. Reson.* **2006**, *178*, 42–55.

[66] George, G. N. EXAFSPAK. Stanford Synchrotron Radiation Laboratory, Stanford Linear Accelerator Center, Stanford University.

[67] Frisch, M. J. et al. Gaussian 09, Revision B.01. Gaussian, Inc., Wallingford, CT, 2010.

[68] Zhao, Y.; Truhlar, D. G. *Theor. Chem. Acc.* **2008**, *120*, 215–241.

[69] Sheldrick, G. M. *Acta Cryst.* **1990**, *A46*, 467–473.

[70] Sheldrick, G. M. SHELXL-97: Program for Crystal Structure Refinement. University of Göttingen, Göttingen, Germany, 1997.

[71] Müller, P. *Crystallogr. Rev.* **2009**, *15*, 57–83.

[72] Dolomanov, O. V.; Bourhis, L. J.; Gildea, R. J.; Howard, J. A. K.; Puschmann, H. *J. Appl. Cryst.* **2009**, *42*, 339–341.

5 Preparation of Low-Valent Iron Complexes Supported by Tris(phosphine)borate and Bis(phosphine)borate Ligands

Contents

5.1 Introduction

Organometallic chemists have long recognized the importance of transition-metal hydride complexes, particularly within the context of reduction processes.[1] The past 15 years have witnessed a surge of studies implicating transition-metal hydride species as intermediates along biocatalytic pathways. For example, the molybdenum–iron nitrogenase cofactor, FeMoco, is able to reduce unsaturated substrates[2–4] such as N_2, CO_2 and $H_2C{=}CH_2$ by the addition of multiple equivalents of protons and electrons, a chemical process in which hydride complexes may be formed.[5,6] In 2005, Dean, Seefeldt and Hoffman provided the first strong evidence for the presence of Fe−H bonds in nitrogenase intermediates via electron–nuclear double resonance (ENDOR) studies of nitrogenase variants freeze-trapped during substrate turnover.[7] Iron hydride complexes have also been proposed as intermediates in hydrogenases.[8,9]

Although their preparation is a burgeoning area of research,[10] there are surprisingly few examples of well-defined synthetic iron hydride complexes that are reported to catalytically reduce olefins under ambient temperature and pressure.[11] Moreover, although paramagnetic hydride species have been proposed as catalytic intermediates of hydrogenase and nitrogenase enzymes, the majority of synthetic transition metal hydride complexes are diamagnetic, closed-shell species. Iron pentacarbonyl is able to hydrogenate 1-hexene, however temperatures in excess of 200 °C and pressures between 200 and 250 atm are required for catalytic activity.[12,13] Wrighton subsequently developed a photocatalytic method for olefin hydrogenation using iron pentacarbonyl that operates efficiently at room temperature and ambient pressure; to achieve catalytic turnover, however, continuous irradiation with 366 nm light was required.[14,15] It was not until 1992 that Bianchini demonstrated the catalytic reduction of alkynes to alkenes under mild conditions (20 °C, 1 atm H_2) using the well-defined, cationic complex $[[PP_3]Fe(H)(L)][BPh_4]$ ($[PP_3] = P(CH_2CH_2PPh_2)_3$, $L = N_2$ or H_2).[16] Despite this success, further conversion of alkenes to alkanes by the Bianchini system was not observed. Holland recently provided examples of dimeric iron(II) hydride and monomeric iron(I) hydride complexes supported by bulky β-diketiminate ligands.[17,18] The reactivity of these complexes with olefins is largely unexplored. The dimeric hydride complexes react with olefins to give iron(II) alkyl species, but no further chemistry was pursued.[18]

In 2004, Chirik and Peters independently reported structurally distinct, well-defined iron complexes capable of catalytically hydrogenating unsaturated hydrocarbon substrates under relatively mild conditions (Figure 5.1). The pyridinediimine (PDI) precatalyst reported by Chirik is particularly active, hydrogenating 1-hexene under 4 atm of H_2 at room temperature with catalyst loadings as low as 0.3 mol %.[19] Notably, this iron system outperforms precious metal catalysts under these conditions, reaching a turnover frequency (TOF) of 1814 h^{-1} compared to 366 h^{-1} for 10% Pd/C, 10 h^{-1} for $(PPh_3)_3RhCl$ and 75 h^{-1} for $[(cod)Ir(PCy_3)(py)][PF_6]$. Mechanistic investigations on the pyridinediimine system suggest a catalytic cycle in which both N_2 ligands are lost, forming an unsaturated 14-electron iron(0) pyridinediimine complex that coordinates olefin. Subsequent oxidative addition of H_2 and insertion of the olefin into the iron(II) hydride bond yields the corre-

sponding iron(II) alkyl complex. Reductive elimination of alkane regenerates the starting low-valent fragment. Although this mechanistic proposal was not formally disclosed, subsequent studies of C−C bond forming reactions catalyzed by the iron PDI complex suggest that the PDI ligand is redox noninnocent and that the iron(II) oxidation state is maintained throughout catalysis.[20]

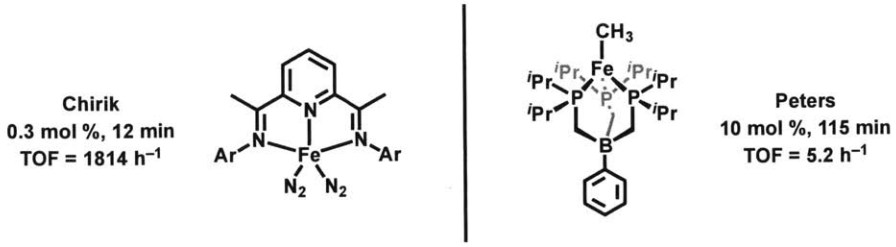

Figure 5.1 Iron precatalysts reported by (*left*) Chirik and (*right*) Peters. Both species are active for the hydrogenation of 1-hexene under mild conditions, with TOFs of 1814 and 5.2 h^{-1}, respectively.

The 14-electron tris(phosphine)borate complex, [$PhBP^{iPr}_3$]FeMe, reported by Peters is much less active than the Chirik system, reaching a TOF of only 5.2 h^{-1} at 10 mol % catalyst loading. However, this provided the opportunity to directly observe several plausible intermediates relevant to the overall catalytic hydrogenation cycle.[21] This system likely proceeds through an iron(II)/iron(IV) redox cycle in which H_2 addition to the iron(II) methyl complex generates an iron(IV) trihydride complex and one equivalent of methane. Loss of H_2 and concomitant olefin binding via an unobserved, four-coordinate iron(II) hydride complex, followed by olefin insertion into the Fe−H bond gives the corresponding iron(II) alkyl complex. This species goes on to react with H_2 to release alkane and regenerate the iron(IV) trihydride species.

Another report of relevance to the hydrogenation chemistry described by Peters is the observation that, in the presence of excess H_2, the Fe−N bond of the iron(III) imido complex [$PhBP^{Ph}_3$]Fe≡NAr (Ar = *p*-tolyl) is cleaved, generating *p*-tolylamine and a reactive, unobserved iron(II) hydride species.[22] In the presence of C_6H_6, insertion into the iron hydride bond occurs, slowly forming a stable iron(II) η^5-cyclohexadienyl species, as shown in Scheme 5.1. Motivated by these results, we sought to extend the hydrogenation chemistry to the [$PhBP^{Ph}_3$] system in hopes of accessing other intermediates along the hy-

drogenation pathway by virtue of the less electron-donating character of the phosphines relative to [PhBP$_3^{iPr}$]. The Peters group has previously shown that the reactivity patterns of [PhBP$_3^{Ph}$]Fe and [PhBP$_3^{iPr}$]Fe can be considerably different.[23] Described in this chapter are efforts toward that end and an exploration of the coordination chemistry of iron bis(phosphine)borate complexes in an attempt to generate a more active precatalyst for olefin hydrogenation.

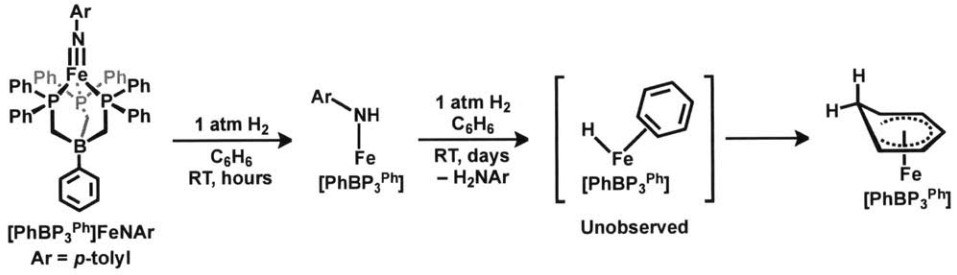

Scheme 5.1 Hydrogenolysis of [PhBP$_3^{Ph}$]Fe≡NAr. The purported iron(II) benzene adduct is not experimentally observed.

5.2 [PhBP$_3^{Ph}$]FeMe: Isolation of an Elusive Species

For the [PhBP$_3^{iPr}$] system described above, the room temperature hydrogenation of a series of iron alkyl complexes gives access to the hydrogenation reactions of interest.[21] Although it would be attractive to employ similar methods to the [PhBP$_3^{Ph}$] system, synthetic challenges have hampered isolation of [PhBP$_3^{Ph}$]FeR complexes. For example, treatment of [PhBP$_3^{iPr}$]FeCl with Grignard or alkyllithium reagents provides the corresponding [PhBP$_3^{iPr}$]FeR species; the analogous reactions with [PhBP$_3^{Ph}$]FeCl result in intractable black solids and the formation of free $PMePh_2$ as a result of B–C_{alkyl} bond cleavage (Scheme 5.2, left). Overreduction of the metal center was avoided by treatment of a C_6H_6 slurry of [PhBP$_3^{Ph}$]FeCl with 10 equiv of Me_2Mg (Scheme 5.2, right). In C_6H_6, Me_2Mg is sparingly soluble, thereby minimizing the potential for deleterious side-reactions and allowing for facile separation of the product, $MgCl_2$ and unreacted Me_2Mg. After 2 h, the 14-electron complex [PhBP$_3^{Ph}$]FeMe (**5.1**) was isolated as an amber powder in ca. 90% yield.

Complex **5.1** is paramagnetic, with broad resonances in its ^{1}H NMR spectrum rang-

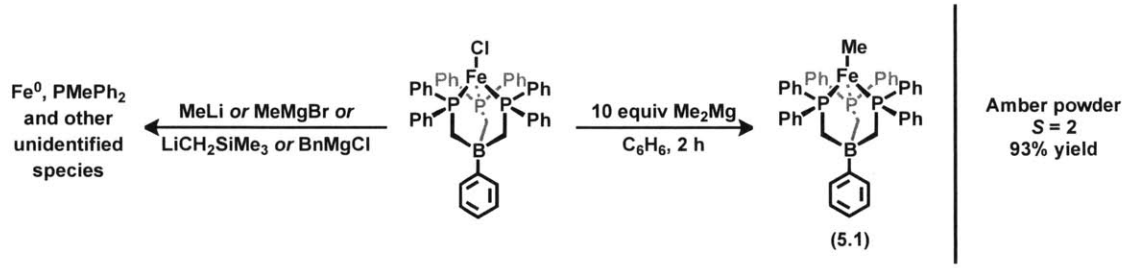

Scheme 5.2 (*left*) Treatment of $[PhBP^{Ph}_3]FeCl$ with alkyllithium and Grignard reagents leads to overreduction of the metal center. (*right*) Overreduction can be avoided using Me_2Mg.

ing from 50 to −110 ppm. The Evans method solution magnetic moment (μ_{eff} = 5.0 μ_B, C_6D_6, 25 °C) indicates an S = 2 ground state and is consistent with that observed for $[PhBP^{iPr}_3]FeMe$. Complex **5.1** crystallizes in the monoclinic space group $C2/c$, with one molecule in the asymmetric unit (Figure 5.2). The geometry at iron is best described as pseudotetrahedral, with an average P−Fe−P angle of 90.79(2)°. The Fe−P distances are slightly asymmetric (2.4089(6), 2.4330(6) and 2.4350(6) Å), however their average (2.4256 Å) is consistent with other mononuclear, high-spin $[PhBP^{Ph}_3]FeX$ complexes (2.34 − 2.452 Å).[22,24] The P−Fe−C46 angles are also distorted (B···Fe−C46 = 175.88°); this observation can be attributed in part to the steric demands of the $[PhBP^{Ph}_3]$ ligand. Five of the six phosphorus-bound phenyl groups lie perpendicular to the P_3 plane, effectively pushing the apical methyl group into a slightly asymmetric configuration. This distortion is also observed for $[PhBP^{Ph}_3]FeCl$ (B···Fe−C46 = 166.54°). In contrast, the related but structurally rigid $[PhBP^{iPr}_3]FeX$ complexes do not display this distortion (B···Fe−X = 179.16° and 179.79° for X = Me and Cl, respectively).[21,25] The Fe−C distance of **5.1** (2.051(2) Å) is ca. 0.04 Å longer than for $[PhBP^{iPr}_3]FeMe$ (2.013(3) Å) and ca. 0.02 Å shorter than $[PhBP^{iPr}_3]FeCH_2Ph$ (2.068(2) Å). Structurally characterized L_3Fe alkyl species are uncommon and the Fe−C distances are summarized in Table 5.1.

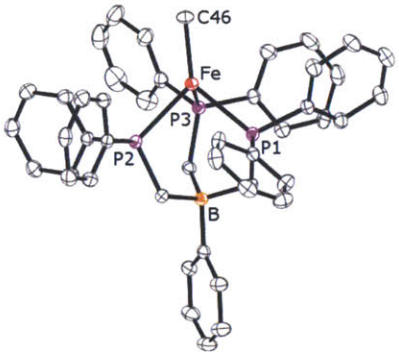

Selected Bond Lengths (Å) and Angles (°)
Fe–C46 = 2.051(2)
Fe–P1 = 2.4350 (6)
Fe–P2 = 2.4330(6)
Fe–P3 = 2.4089(6)
P1–Fe–P2 = 93.11(2)
P1–Fe–P3 = 89.33(2)
P2–Fe–P3 = 89.94(2)
B···Fe–C46 = 175.88

Figure 5.2 Solid-state structure of **5.1**. Thermal ellipsoids are drawn at 40% probability. Hydrogen atoms are omitted for clarity.

Complex	Fe–C (Å)	Complex	Fe–C (Å)
5.1	2.051(2)	$[HTp^{iPr,iPr}]FeCH_2(HC{=}CH_2)$[26]	2.04(1)
$[PhBP_3^{iPr}]FeMe$[21]	2.013(3)	$[HTp^{iPr,iPr}]Fe(p\text{-tolyl})$[26]	2.05(1)
$[PhBP_3^{iPr}]FeCH_2Ph$[21]	2.068(2)	$[^{Et}PDI]FeCH_2(CH_3)_3$[27]	2.036(4)
$[PhTt^{tBu}]FeMe$[28]	2.034(3)	$[^{Et}PDI]FeCH_2Si(CH_3)_3$[27]	2.034(1)
$[PhTp^{tBu,tBu}]FeMe$[29]	2.079(3)	$[^{iPr}PDI]FeCH_3$[30]	2.001(6)
$[HTp^{tBu,Me}]FeMe$[31]	2.052(3)	$[[^{iPr}PDI]FeCH_3][Li(THF)_4]$[32]	2.015(8)
$[HTp^{tBu,Me}]FeCH_2CH_3$[31]	2.069(3)		

Table 5.1 Comparison of Fe–C distances of structurally characterized L_3Fe alkyl species. $[RTp^{R',R''}]$ = R-tris(3-R'-5-R''-pyrazolyl)borate; $[^{R}PDI]$ = 2,6-((2,6-$R_2C_6H_3N{=}CMe)_2C_5H_3N$); $[PhTt^{tBu}] = C_6H_5B(CH_2SC(CH_3)_3)_3$.

5.3 Hydrogenation Studies Employing $[PhBP_3^{Ph}]FeMe$

Relatively little is known about the reactivity patterns of electron-deficient iron alkyl species.[21,29,33–41] To assess the ability of **5.1** to act as a competent hydrogenation precatalyst, **5.1** was treated with 10 equiv of 1-hexene and 1 atm of H_2 at room temperature (Scheme 5.3). While conversion to hexane is observed, the reaction is very slow, reach-

ing 95% conversion at 180 min with a TOF of 3.3 h^{-1}. Under identical conditions, the related [$PhBP_3^{iPr}$]FeMe precatalyst reaches 95% conversion at 115 min with a TOF of 5.2 h^{-1}.[21] In C_6H_6 solution, the final iron-containing product is the previously reported iron η^5-cyclohexadienyl species (Scheme 5.1).[22] Given the slow hydrogenation of 1-hexene by **5.1**, we reasoned that intermediates along the catalytic cycle might be isolated or at least observed, thereby adding to our understanding of the mechanism of hydrogenation by low-valent, low-coordinate iron tris(phosphine)borate complexes.

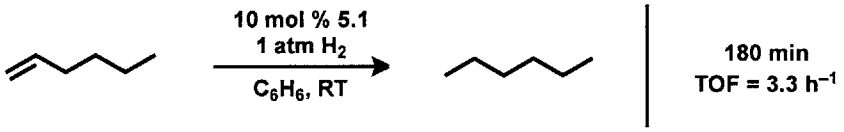

Scheme 5.3 Catalytic hydrogenation of 1-hexene by 10 mol % of **5.1**.

Treatment of a C_6H_6 solution of **5.1** with 1 atm of H_2 at room temperature yielded the iron η^5-cyclohexadienyl complex within 15 min; the addition of PMe_3, PPh_3 or PMe_2Ph prior to H_2 addition did not prevent its formation. Notably, [$PhBP_3^{iPr}$]FeMe does not activate C_6H_6 and hydrogenation reactions with this system may be carried out in C_6H_6 solution without forming the stable, 18-electron η^5-cyclohexadienyl species. In contrast, exposure of a room temperature THF-d_8 solution of **5.1** to 1 atm H_2 in a J. Young NMR tube resulted in a color change from light yellow to dark green within minutes of the addition (Scheme 5.4). In the ^1H NMR spectrum, complete consumption of **5.1** was observed, concomitant with the release of CH_4 and the formation of a new, paramagnetic species. The $^{31}P\{^1H\}$ NMR spectrum has no discernible features, suggesting that all three phosphines of the ligand are coordinated to the paramagnetic metal center. The solution IR spectrum (KBr, THF) showed a band at 1960 cm^{-1}, consistent with the presence of a hydride moiety. This in situ generated green species decomposes over a period of days under an H_2 atmosphere to give an intractable black solid and free $PMePh_2$; it is unstable to vacuum and also to replacement of the H_2 atmosphere with N_2. Attempts to crystallize the green species under 1 atm H_2 have, to date, been unsuccessful, precluding definitive assignment. Despite this, the green species is proposed to contain an Fe–H unit on the basis of its IR spectrum (1960 cm^{-1}) and subsequent reactivity. For example, addition of 1 drop of C_6H_6

to the green solution results in the formation of the expected η^5-cyclohexadienyl complex. Alternatively, exposure of the green solution to 1 atm of CO results in an immediate color change to yellow. The yellow powder isolated was identified as the previously reported diamagnetic bis(carbonyl) hydride complex, $[PhBP^{Ph}_3]Fe(CO)_2(H)$, on the basis of ^1H and $^{31}P\{^1H\}$ NMR and IR spectroscopies (ν_{CO} = 1951, 2004 cm^{-1}).[42] These results suggest that the green species formed is an iron hydride; whether the complex also contains other ligands, such as solvent or H_2, or is polymeric, is unknown.

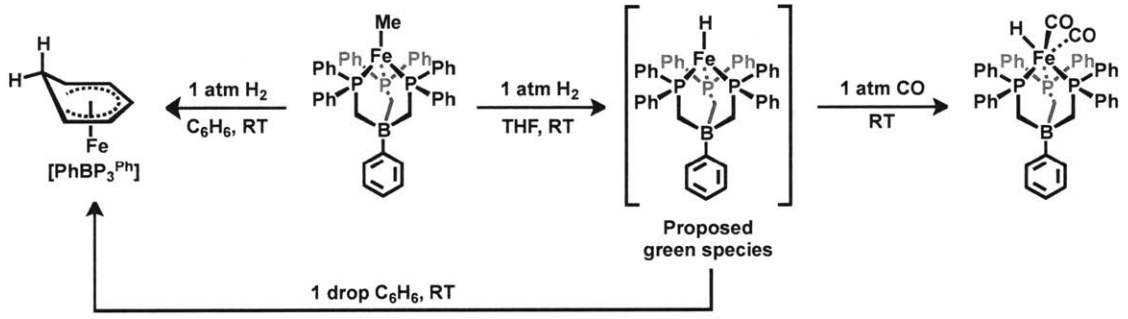

Scheme 5.4 Hydrogenolysis of **5.1** in C_6H_6 forms the stable, η^5-cyclohexadienyl complex (*left*), while in THF results in a bright green solution. This solution is proposed to contain an Fe−H unit on the basis of subsequent reactivity with CO (*right*) and C_6H_6 (*bottom*).

Although the presence of a hydride was implied by the formation of the η^5-cyclohexadienyl complex and $[PhBP^{Ph}_3]Fe(CO)_2(H)$ from the green species, a more definitive assignment of the intermediate species was desired. Seeking to stabilize the intermediate hydride product, the hydrogenation reactions were repeated in the presence of a trapping phosphine. Treatment of a THF-d_8 solution of **5.1** in a J. Young NMR tube with 1 equiv PMe_2Ph did not change the color of the reaction mixture, nor was there any indication of phosphine binding at room temperature: the $^{31}P\{^1H\}$ NMR resonance corresponding to free PMe_2Ph remained sharp over a period of days. In contrast to the reactions without added phosphine, the addition of 1 atm H_2 to this mixture resulted in an immediate color change from light yellow to orange. The ^1H NMR spectrum of the crude reaction mixture showed quantitative consumption of both **5.1** and PMe_2Ph, along with the formation of CH_4 and a new, diamagnetic species. The crude $^{31}P\{^1H\}$ NMR spectrum features two singlets at 30.8 and 60.2 ppm, corresponding to bound PMe_2Ph and bound $[PhBP^{Ph}_3]$, respectively. Accordingly, these singlets integrate in a 1:3 ratio. In the ^1H NMR spectrum, a somewhat broad

peak appears at −9.8 ppm (w_h = 57 Hz) consistent with the presence of a hydride moiety.[43] This peak corresponds to *three* protons, as determined by integration.

Hydrogenation of the related [$PhBP_3^{iPr}$]FeMe complex in the presence of PMe_3 yields the iron(IV) trihydride complex, [$PhBP_3^{iPr}$]$Fe(H)_3(PMe_3)$, assigned on the basis of NMR studies and a solid-state structure.[21] The crude spectral features observed for this system and for the product of the hydrogenation of **5.1** in the presence of PMe_2Ph are very similar. The $^{31}P\{^1H\}$ NMR spectrum of [$PhBP_3^{iPr}$]$Fe(H)_3(PMe_3)$ features two singlets at 28.8 and 70.8 ppm, corresponding to the PMe_3 ligand and the [$PhBP_3^{iPr}$] phosphines, respectively. The ^1H NMR spectrum shows a single resonance in the hydride region at −13.6 ppm, corresponding to three protons by integration. Despite their similarities, there are a few important distinctions that set the two complexes apart. For example, the hydride resonance of [$PhBP_3^{iPr}$]$Fe(H)_3(PMe_3)$ in the ^1H NMR spectrum is split into a doublet of quartets as a result of two-bond H−P coupling to the PMe_3 and [$PhBP_3^{iPr}$] ligands ($^2J_{HP}$ = 61.2 and 32.0 Hz, respectively). The hydride resonance of the orange species formed in the hydrogenation of **5.1**, however, is a broad peak at room temperature and displays no discernible coupling at this temperature. A T_1 spin-lattice relaxation measurement of the species in solution was carried out to deconvolute the hydride pattern. For this experiment, a short relaxation time (T_1 < 80 ms) indicates the presence of a dihydrogen species, due to a direct H−H interaction, while a longer relaxation time (T_1 > 100 ms) implies the presence of a hydride species[44–46] For the orange species in solution, the room temperature T_1 experiment yielded a relaxation time of 32 ms, indicating that this species is best described as an iron(II) dihydrogen hydride complex, [$PhBP_3^{Ph}$]$Fe(H_2)(H)(PMe_2Ph)$ (**5.2**). The structurally related dihydrogen adduct $[Fe(H_2)(H)(PMe_3)_4]^+$ provides a T_{1min} of 13.5 ms, while $[Fe(H)_3(PEt_3)_4]^+$ exhibits a much slower relaxation time of 177 ms.[47] In contrast to the [$PhBP_3^{Ph}$]Fe system, [$PhBP_3^{iPr}$]$Fe(H)_3(PMe_3)$ furnishes a T_{1min} of 140 ms, consistent with its formulation as a classical trihydride complex.[21]

Complex **5.2**, like the purported hydride species in the green solution described above, decomposes over a period of days under an H_2 atmosphere to give intractable black solids, $PMePh_2$ and PMe_2Ph, precluding isolation and characterization by X-ray crystallography. In addition, **5.2** is not stable to vacuum or to replacement of the H_2 atmosphere with an N_2

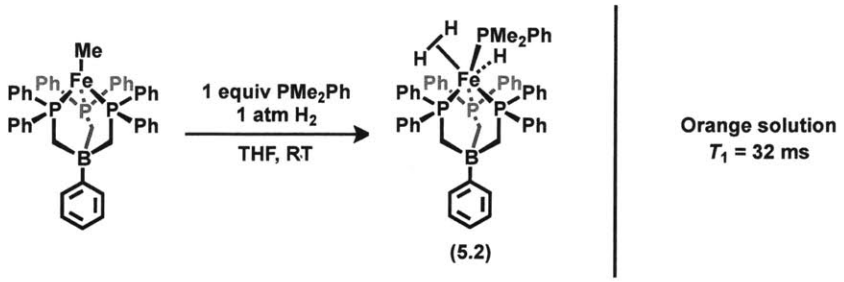

Scheme 5.5 Hydrogenation of a THF solution of **5.1** in the presence of PMe_2Ph yields the orange dihydrogen hydride species **5.2**.

atmosphere. While the decomposition of **5.2** leads to mixture of unidentified products, we could grow single crystals of one of the decomposition products. X-ray crystallographic analysis identified the species as the iron(I) complex, $[PhBP_3^{Ph}]Fe(PMe_2Ph)$ (**5.3**, Figure 5.3); complex **5.3** presumably forms by bimolecular loss of H_2 from **5.2**. Based on the mass of the crystals isolated and the mass of the residual material, $[PhBP_3^{Ph}]Fe(PMe_2Ph)$ comprises ca. 5% of the product mixture for this particular experiment. Complex **5.3** crystallizes in the monoclinic space group $P2_1/c$, with one molecule in the asymmetric unit. As with **5.1**, the geometry at iron is best described as pseudotetrahedral, with symmetric P–Fe–P angles (96.03(2), 97.60(2) and 93.62(2)°). The P–Fe–P4 angles are slightly more distorted than in **5.1**, with a B···Fe–P4 angle of 174.21°, as opposed to 175.88° for **5.1**. The Fe–P4 distance of 2.3097(9) Å is similar to that of $[PhBP_3^{Ph}]Fe(PPh_3)$ (2.2889(9) Å) and $[PhBP_3^{iPr}]FePMe_3$ (2.3220(4) Å).[21,24] The tris(phosphine)borate Fe–P distances are slightly asymmetric (2.3097(9), 2.3298(7) and 2.3388(6) Å); this structural feature is also observed for $[PhBP_3^{Ph}]Fe(PPh_3)$ (2.334(1), 2.335(1) and 2.340(1) Å) and $[PhBP_3^{iPr}]Fe(PMe_3)$ (2.3217(4), 2.3393(4) and 2.3452(4) Å). The lack of asymmetry in the crystal structure, particularly with respect to the P–Fe–P angles, indicates that there are no hydride ligands present in the complex and that the formulation of **5.3** is correct.

To address the possible presence of an unobserved hydride moiety in the crystal structure presented above, **5.3** was prepared by an independent route. Treatment of $[PhBP_3^{Ph}]$-FeCl with 1 equiv Na/Hg in the presence of 3 equiv PMe_2Ph furnishes **5.3** in ca. 65% yield (Scheme 5.6). Complex **5.3** is paramagnetic, with broad resonances in the ^1H NMR spectrum ranging from 95 to −9 ppm. The Evans method solution magnetic moment mea-

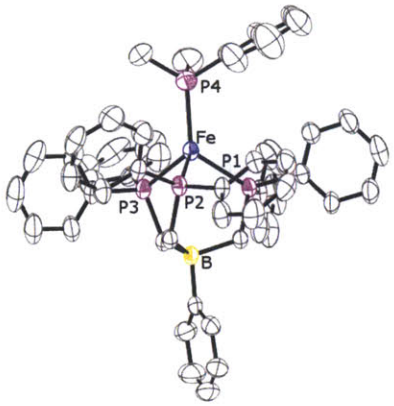

Selected Bond Lengths (Å) and Angles (°)

Fe–P1 = 2.3298(7)
Fe–P2 = 2.3388(6)
Fe–P3 = 2.3066(7)
Fe–P4 = 2.3097(9)
P1–Fe–P2 = 96.03(2)
P1–Fe–P3 = 97.60(2)
P2–Fe–P3 = 93.62(2)
B···Fe–P4 = 174.21

Figure 5.3 Solid-state structure of **5.3**. Thermal ellipsoids are drawn at 40% probability. Hydrogen atoms are omitted for clarity.

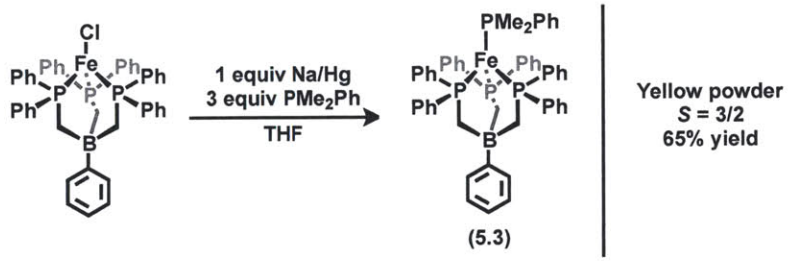

Scheme 5.6 Independent synthesis of **5.3** by reduction of [PhBP$^{Ph}_3$]FeCl with Na/Hg in the presence of excess PMe_2Ph.

surement of 4.1 μ_B in C_6D_6 is higher than the spin-only value of 3.87 μ_B for three unpaired electrons. This S = 3/2 ground state is consistent with that of [PhBP$^{Ph}_3$]Fe(PPh_3).[24] Comparison of the ^{1}H NMR spectrum of the crystals described above and of **5.3** indicates that the two materials are identical. Complex **5.3** does not bind or react with 1 atm H_2 at room temperature or upon heating to 60 °C, implying that, once formed, **5.3** cannot re-enter the catalytic cycle, supporting the lack of unobserved hydrides in the crystal structure described above. Whereas no additional information about the olefin insertion and subsequent alkane release processes beyond what had been previously reported[21] was gleaned in this study, the move to a less electron-donating tris(phosphine)borate ligand did allow for the characterization of a dihydrogen hydride species. This type of complex was invoked in the hydrogenation of olefins by [PhBP$^{iPr}_3$]FeMe, although no spectroscopic evidence for its formation could be obtained.

5.4 Accessing the Iron Chemistry of Bis(phosphine)borate Ligands

Having observed hydrogenation of 1-hexene, we sought to develop a more robust and active iron system while maintaining a similar ligand set. We reasoned that removal of a ligand arm from the [$PhBP^{Ph}_3$] framework would serve two purposes: first, a less sterically encumbering ligand could allow substrates better access to the metal center and second, decomposition via $B-C_{alkyl}$ bond cleavage could be circumvented, or at least tempered, by virtue of there being one fewer susceptible linkage. The Peters group has developed the 2nd and 3rd row metal chemistry of the bis(phosphine)borate ligand [$Ph_2BP^{Ph}_2$], primarily within the context of C–H and E–H bond activation and copolymerization catalysis (Figure 5.4).[48–50] These zwitterionic complexes complement their cationic relatives in that they (i) are soluble in non-coordinating and less polar solvents, (ii) have the potential for increased functional group tolerance relative to the cationic systems and (iii) should not exhibit the counterion effects that are sometimes observed in discrete salt systems.

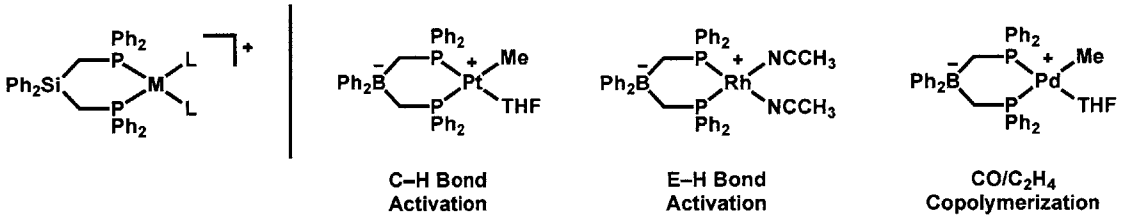

Figure 5.4 Comparison of metal complexes containing neutral bis(phosphine)silane (*left*) and anionic bis(phosphine)borate ligands (*right*).

The bis(phosphine)borate scaffold also benefits from facile modification at both the boron and phosphorus centers. Although Thomas was able to install a number of aryl groups on the boron center, he found that variation of the borate substituent had little effect on the overall electronic structure of resulting metal complex.[51] Modification of the phosphine substituents had a more pronounced effect, consistent with a description in which the borate unit is electronically insulated from the metal center. To develop the iron chemistry of bis(phosphine)borate ligands within the context of the hydrogenation chemistry presented in previous sections, two ligand frameworks were targeted. The

first, $[Ph_2BP_2^{Ph}]$, maintains the electronic character of the phosphines in $[PhBP_3^{Ph}]$ while the second, $[Ph_2BP_2^{tBu}]$, employs more electron-donating and bulkier *tert*-butyl groups on the phosphines, in an effort to lend some degree of steric protection to the metal center (Figure 5.5).

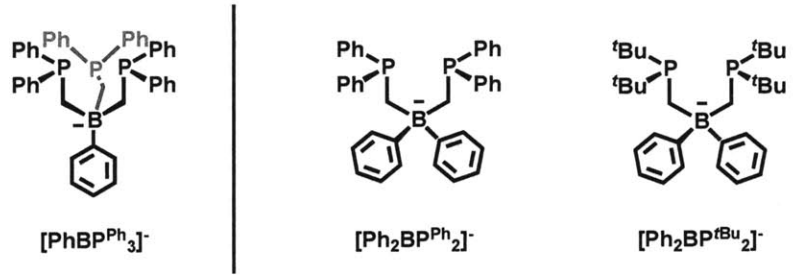

Figure 5.5 Comparison of tris(phosphine)borate (*left*) and anionic bis(phosphine)borate ligands used in this study (*right*).

Treatment of the previously reported $[Ph_2BP_2^{Ph}][ASN]$ with 1 equiv of $FeCl_2$ in THF yielded a white powder in ca. 90% yield after workup. This white powder is sparingly soluble in THF and acetone and is stable in solution at least up to 60 °C. The ^1H NMR spectrum in acetone-d_6 indicates the formation of a paramagnetic species, with broad resonances ranging from 120 to −5 ppm. There are two sharp resonances in the ^1H NMR spectrum at 2.39 and 3.78 ppm that integrate in a 1:1 ratio. This result, coupled with the solubility properties of the white powder, suggests that the product is the 'ate' complex, $[[Ph_2BP_2^{Ph}]FeCl_2][ASN]$ (**5.4**, Scheme 5.7). A reliable Evans method solution magnetic moment was not obtained due to the insolubility of **5.4**. Variable temperature solid-state SQUID magnetic data were obtained for **5.4** and the μ_{eff} versus temperature plot is shown in Figure 5.6. The data establish a $S = 2$ spin-state assignment, with a μ_{eff} value of 5.1 μ_B at 300 K. There is a drop in the magnetic moment in the range below 50 K is likely a consequence of zero-field splitting (ZFS) and was well-simulated using the JulX program.[52] Attempts to displace [ASN][Cl] by the addition of pyridine or MeCN were unsuccessful. THF solutions of **5.4** are stable to both excess pyridine and MeCN and heating these mixtures to 60 °C for 1 week resulted in no reaction. X-ray quality crystals were unable to be obtained, again due to the insolubility of the complex.

Conceptually related to the iron bis(phosphine)borate complexes presented in this and

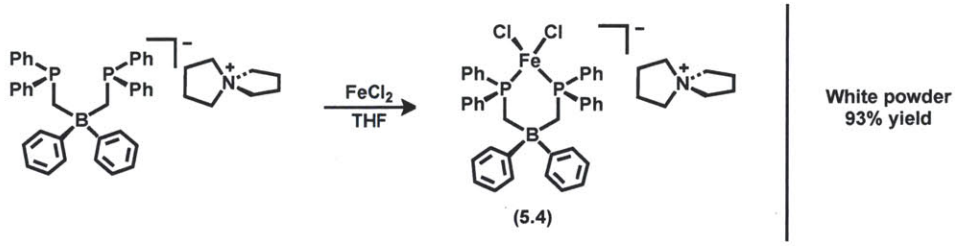

Scheme 5.7 Treatment of $[Ph_2BP_2^{Ph}][ASN]$ with $FeCl_2$ yields the 'ate' complex **5.4**.

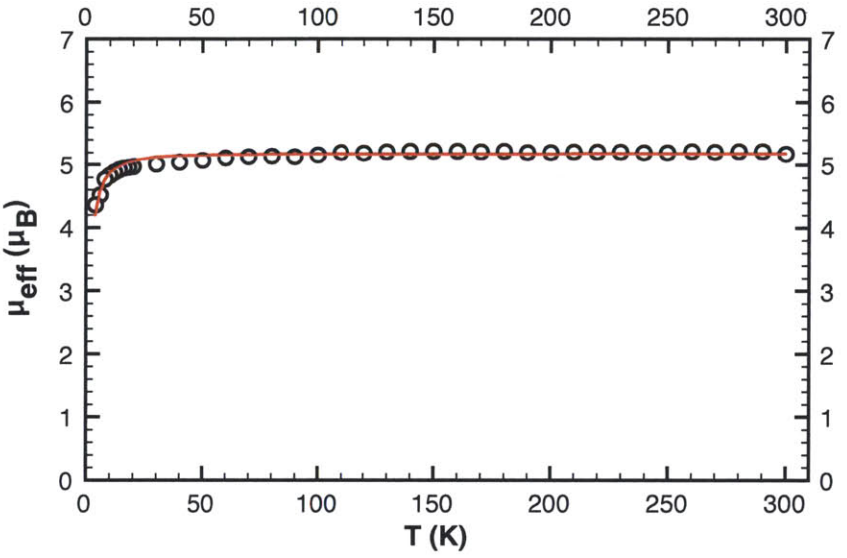

Figure 5.6 SQUID magnetometry data (0.5 T) and fit for **5.4**. JulX simulation parameters: g = 2.113, D = 7.033.

the following sections is the iron β-diketiminate chemistry reported by Holland. In exploring the preparation of iron(II) halide complexes, Holland found that simple modification of the β-diketiminate ligand had a significant effect on the identity of the resulting complex, yielding either $L^{Me}Fe(\mu-Cl)_2Li(THF)_2$ or $L^{tBu}FeCl$, depending on the bulkiness of the substituents on the β-diketiminate backbone (L^{Me} = 2,4-bis(2,6-diisopropylphenylimido)-pentyl; L^{tBu} = 2,2,6,6-tetramethyl-3,5-bis(2,6-diisopropylphenylimido)-hept-4-yl).[53] In an attempt to realize a similar effect and access a lower-coordinate species, we pursued the iron chemistry of the bulkier alkyl substituted bis(phosphine)borate, $[Ph_2BP_2^{tBu}]$. Treatment of $[Ph_2BP_2^{tBu}][Tl]$ with 1 equiv of $FeBr_2$ resulted in the formation of a dark orange

solution and a white precipitate (Scheme 5.8). After workup, an amber powder was isolated in ca. 60% yield. This species is paramagnetic, with ^{1}H NMR resonances ranging from 65 to -115 ppm. X-ray crystallographic analysis by Lu[54] identified the species as the dimeric $\{[Ph_2BP_2^{tBu}]FeBr\}_2$ complex (**5.5**, Figure 5.7). Complex **5.5** crystallizes in the triclinic space group $P\bar{1}$, with one molecule per asymmetric unit. The average Fe$-$P bond length of 2.4529(2) Å is typical of a pseudotetrahedral four-coordinate, iron(II) bis(phosphine) dibromide complex. The $Fe_2(\mu-Br)_2$ core is fairly symmetric, as reflected by the Fe$-$Br bond lengths of 2.5238(3) and 2.5395(3) Å. These bond lengths are similar to those of other structurally characterized, four-coordinate iron $(\mu-Br)_2$ complexes (2.45 – 2.57 Å).[55–58] The Fe$-$Fe distance is 3.5630 Å precluding a direct metal-metal interaction. The iron and phosphorus atoms are coplanar, with the two bromine atoms residing above and below the plane, resulting in a distorted tetrahedral geometry at each iron center.

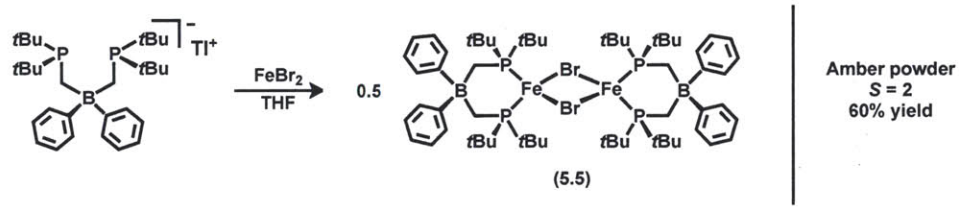

Scheme 5.8 Treatment of $[Ph_2BP_2^{tBu}][Tl]$ with $FeBr_2$ yields the dimeric $(\mu-Br)_2$ complex **5.5**.

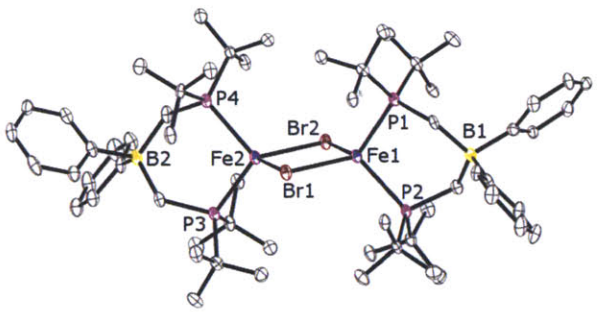

Selected Bond Lengths (Å) and Angles (°)

Fe1–P1 = 2.4438(3)
Fe1–P2 = 2.4577(3)
Fe2–P3 = 2.4516(3)
Fe2–P4 = 2.4585(3)
Fe1–Br1 = 2.5238(3)
Fe1–Br2 = 2.5395(3)
Fe2–Br1 = 2.5238(3)
Fe2–Br2 - 2.5290(3)
Br1–Fe1–Br2 = 90.31(3)
Br1–Fe2–Br2 = 90.64(3)
P1–Fe1–P2 = 100.81(3)
P3–Fe2–P4 = 99.18(3)

Figure 5.7 Solid-state structure of **5.5**. Thermal ellipsoids are drawn at 40% probability. Hydrogen atoms are omitted for clarity.

Notable is that although the use of $[Ph_2BP_2^{tBu}]$ did allow for the formation of a neutral species by salt metathesis, substitution of $FeBr_2$ with $FeCl_2$ does not form the expected analogue of **5.5**. Instead, $[[Ph_2BP_2^{tBu}]FeCl_2][Tl]$ was structurally characterized by Lu.[54] The

complex $[[Ph_2BP_2^{Ph}]FeCl_2][Tl]$ crystallizes in the monoclinic space group $P2_1/n$, with one molecule in the asymmetric unit (Figure 5.8). The iron center is in a pseudotetrahedral geometry, bound by the two phosphines of the bis(phosphine)borate and two chlorides. The Fe–P bond lengths of 2.4462(2) and 2.3552(2) Å are typical of other pseudotetrahedral four-coordinate, iron(II) bis(phosphine) dichloride complexes (2.41 – 2.55 Å). Notably, removal of the chloride ligand to generate TlCl does not occur, despite the well-known application of thallium(I) salts as potent halide abstraction reagents. Instead, the thallium counterion is bound to a chlorine atom, resulting in a Fe–(μ–Cl)–Tl interaction; this M–X–Tl (M = transition metal, X = Cl, F) structural motif is relatively rare. The Tl–Cl1 bond length of 2.9538(2) Å and the Tl···Cl2 distance of 3.2140(2) Å are in the range of those observed for other M–X–Tl complexes (2.39 – 3.63 Å).[59–71] The Fe–Cl distances (2.2860(2) and 2.2978(3) Å) are similar to other structurally characterized, mononuclear, 4-coordinate iron dichloride complexes containing a Cl–Fe–(μ–Cl)–M (M = Li, K) fragment.[53,72–77] Although an argument can be made for Fe–Cl–Tl being a preferred structural motif over Fe–Br–Tl based on the lattice energies of Fe–X and Tl–X (X = Cl or Br), it remains unclear as to why the two complexes adopt different overall configurations ('ate' vs dimeric).

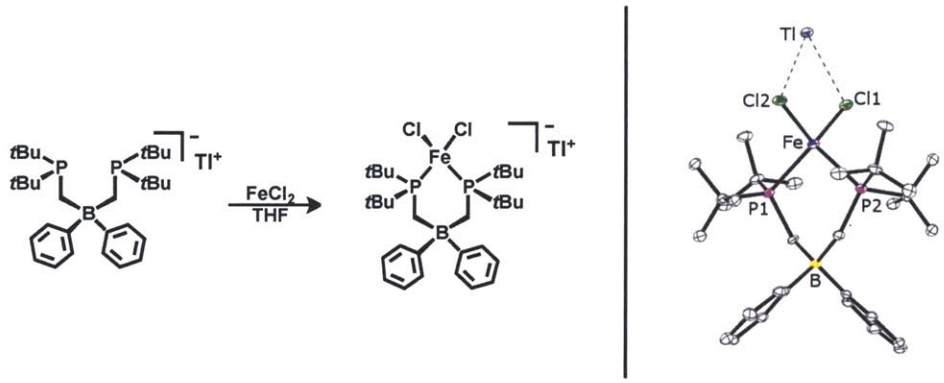

Figure 5.8 (*left*) Synthesis of $[[Ph_2BP_2^{Ph}]FeCl_2][Tl]$. (*right*) Solid-state structure of $[[Ph_2BP_2^{Ph}]FeCl_2][Tl]$. Thermal ellipsoids are drawn at 40% probability. Hydrogen atoms are omitted for clarity.

5.5 Preparation of Bis(phosphine)borate Anilido and Aryloxide Complexes

Attempts to reduce **5.4** with Na/Hg, $NaC_{10}H_8$ or KC_8 in the presence or absence of PMe_3, PPh_3 or PMe_2Ph resulted in the formation of a mixture of products, the majority of which were intractable black solids and free $MePh_2P$ via B–alkyl bond cleavage (vide infra). Gratifyingly, anilido and aryloxide complexes of $[Ph_2BP_2^{Ph}]Fe$ could be obtained by salt metathesis routes. Treatment of a THF slurry of **5.4** at −35 °C with LiNHAr (Ar = 2,6-diisopropylphenyl) resulted in a color change from white to dark orange over the period of 3 h. Analysis of the reaction mixture by ^1H NMR spectroscopy indicated the quantitative consumption of **5.4** and the formation of a new, paramagnetic species, as well as free H_2NAr. Crystallographic structure determination of the major product by Lu[54] established its identity as the bis(anilido) complex, $[[Ph_2BP_2^{Ph}]Fe(NHAr)_2][ASN]$ (**5.6**, ca. 50%, Scheme 5.9). Complex **5.6** is paramagnetic, with ^1H NMR signals ranging from 110 to −80 ppm. The Evans method solution magnetic moment measurement (μ_{eff} = 5.4 μ_B, CD_2Cl_2, 25 °C) is consistent with an S = 2 ground state. Complex **5.6** crystallizes in the monoclinic space group $C2/c$, with half a molecule in the asymmetric unit (Figure 5.9). The Fe–P distance of 2.4903(2) Å is similar to those of the related high-spin $[PhBP_3^{Ph}]Fe$ complexes described in previous sections of this chapter. The Fe–N distance of 1.9749(2) Å falls within the range of other structurally characterized, four-coordinate iron complexes containing a monodentate anilido ligand (1.88 – 2.03 Å).[22,78–83] The Fe–N–C angle of the anilido ligand is bent, at 136.91(3)°; the hydrogen atoms bound to nitrogen were located in the difference map and refined. A bent anilido ligand was also observed for the related $[PhBP_3^{Ph}]FeNH(p\text{-tol})$ complex, which exhibits an Fe–N–C angle of 127.4(2)°.[22] The addition of 0.5 equiv I_2 to a THF solution of **5.6** at room temperature did not result in the formation of [ASN][I] and $[Ph_2BP_2^{Ph}]Fe(NH(Ar))_2$, but rather no reaction.

Aryloxide complexes can be accessed by the same method; treatment of a THF slurry of **5.4** at −35 °C with one equiv of TlOAr (Ar = 2,6-diisopropylphenyl) afforded yellow $[[Ph_2BP_2^{Ph}]Fe(Cl)(OAr)][ASN]$ (**5.7**) in ca. 75% yield (Scheme 5.10, left). This species is

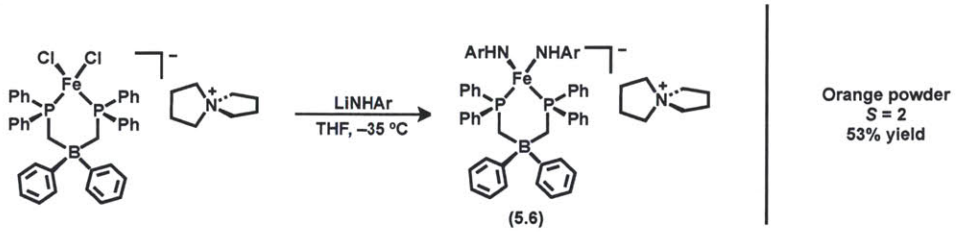

Scheme 5.9 Treatment of **5.4** with LiNHAr (Ar = 2,6-diisopropylphenyl) yields the bis(anilido) complex **5.6**.

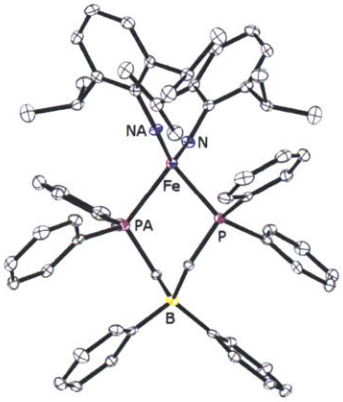

Selected Bond Lengths (Å) and Angles (°)
Fe–P = 2.4903(2)
Fe–N = 1.9749(2)
P–Fe–PA = 86.36 (3)
N–Fe–NA = 128.71(3)

Figure 5.9 Solid-state structure of **5.6**. Thermal ellipsoids are drawn at 40% probability. ASN counterion and hydrogen atoms are omitted for clarity.

paramagnetic, with ^{1}H NMR resonances ranging from 103 to −43 ppm; the Evans method solution magnetic moment of 5.1 μ_B is slightly higher than the spin-only value of 4.90 μ_B for four unpaired electrons, indicating an $S = 2$ ground state. The orange bis(aryloxide) species, [[$Ph_2BP_2^{Ph}$]Fe(OAr)$_2$][ASN] (**5.8**), was prepared in ca. 50% yield by treatment of a THF slurry of **5.4** at −35 °C with two equiv of TlOAr (Ar = 2,6-diisopropylphenyl, Scheme 5.10, right). As with **5.7**, this species is paramagnetic with ^{1}H NMR signals ranging from 97 to −41 ppm; the Evans method solution magnetic moment is 5.1 μ_B, consistent with an $S = 2$ ground state. Single crystals of **5.8** were not obtained, however its structure is likely similar to that of **5.6**.

Complex **5.7** crystallizes in the triclinic space group $P\bar{1}$ with one molecule per asymmetric unit. The iron center is again in a pseudotetrahedral geometry, ligated by the two phosphines of the bis(phosphine)borate ligand, one aryloxide and one chloride (Figure 5.10). Overall, the structural parameters of **5.7** are very similar to those of **5.6**, with an

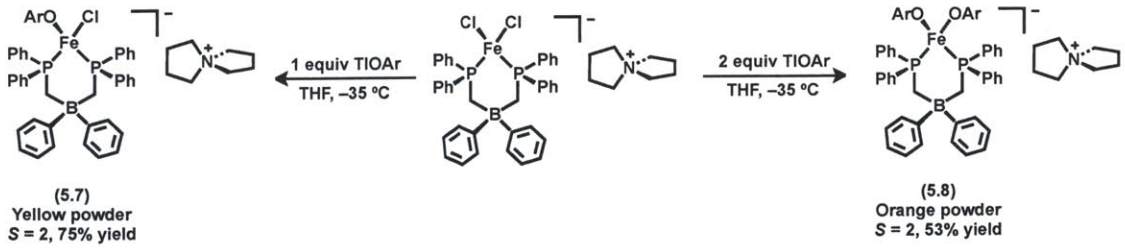

Scheme 5.10 Treatment of **5.4** with 1 or 2 equiv of TlOAr (Ar = 2,6-diisopropylphenyl) yields the mono and bis(aryloxide) complexes **5.7** (*left*) and **5.8** (*right*), respectively.

average Fe–P angle of 2.4438(3) Å and an P1–Fe–P2 angle of 91.62(3)°. The Fe–O distance of 1.8790(3) Å falls within the range of other iron aryloxide complexes (1.725 – 2.545 Å) and the Fe–Cl distance is similar to that observed for the non-thallium ligated chloride ligand in $[[Ph_2BP_2^{Ph}]FeCl_2][Tl]$. As with **5.6**, the aryloxide ligand is bent, with an Fe–O–C angle of 128.78(3)°. The closely related complex, $[PhBP_3^{mter}]Fe(p\text{-}(OH)OAr)$ (*m*ter = (3,5-diphenyl)phenyl, Ar = phenyl), exhibits an Fe–O–C angle similar to that of **5.7** (127.318(3)°).[84] Complex **5.7** provides the opportunity to access a species of the type $[Ph_2BP_2^{Ph}]FeX$ by treatment with the appropriate halide abstraction reagent. However, treatment of **5.7** with $TlPF_6$, $TlNO_3$, AgOTf or $AgPF_6$ yielded either no reaction or, in the case of the silver reagents, dechelation of $[Ph_2BP_2^{Ph}]$ from the iron center.

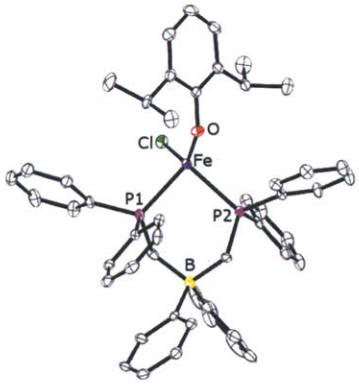

Selected Bond Lengths (Å) and Angles (°)
Fe–P1 = 2.4375(3)
Fe–P2 = 2.4500(3)
Fe–O = 1.8790(3)
Fe–Cl = 2.2698(3)
P1–Fe–P2 = 91.62(3)
O–Fe–Cl = 122.89(3)
Fe–O–C = 128.78(3)

Figure 5.10 Solid-state structure of **5.7**. Thermal ellipsoids are drawn at 40% probability. ASN counterion and hydrogen atoms are omitted for clarity.

5.6 Preparation of Bis(phosphine)borate Alkyl Complexes

In relation to the hydrogenation chemistry presented in the first two sections, the most interesting and pertinent complexes to pursue with the bis(phosphine)borate systems would be iron alkyl species. These complexes are expected to be more reactive than **5.1** by virtue of their lower electron count and decreased steric pressure relative to **5.1**. Treatment of a THF slurry of **5.4** at −35 °C with 2 equiv of BnMgCl resulted in the formation of a red-orange solution concomitant with a white precipitate. The dibenzyl complex $[[Ph_2BP_2^{Ph}]FeBn_2][ASN]$ (**5.9**) was isolated as an orange powder in ca. 60 % yield (Scheme 5.11). Like the other $[[Ph_2BP_2^{Ph}]FeX_2][ASN]$ complexes described in this chapter, **5.9** is a paramagnetic species, with ^1H NMR resonances ranging from 134 to −83 ppm. The Evans method solution magnetic moment measurement of 5.3 μ_B establishes that **5.9** is an $S = 2$ species.

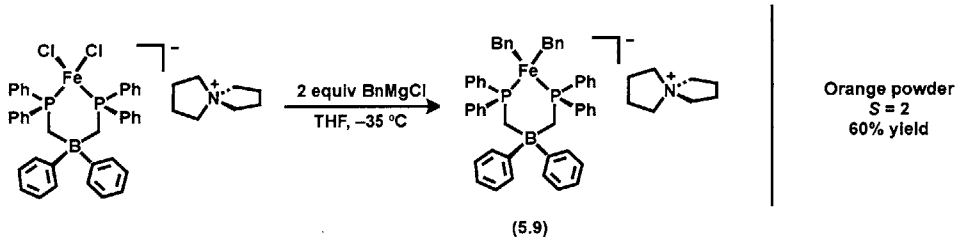

Scheme 5.11 Treatment of **5.4** with 2 equiv of BnMgCl yields the bis(benzyl) complex **5.9**.

Complex **5.9** crystallizes in the triclinic space group $P\bar{1}$, with one molecule per asymmetric unit (Figure 5.11). The iron center adopts a distorted tetrahedral geometry, with a C6−Fe−C20 angle of 111.06(3)° and a P1−Fe−P2 angle of 88.76(3)°. These values are very similar to those observed for the structurally characterized $Fe(CH_2C_6H_4Me)_2$(dippe) (dippe = 1,2-bis(diisopropylphosphino)ethane); for this complex, the C−Fe−C angle is 111.8° and the P−Fe−P angle is 83.30°.[33] The authors attribute the large C−Fe−C and compressed P−Fe−P angles to the steric bulk of the alkyl substituents and the chelating nature of the phosphine. The C−Fe−C and P−Fe−P planes of **5.9** are nearly perpendicular, with a dihedral angle of 85.28°, similar to that of $Fe(CH_2C_6H_4Me)_2$(dippe) (85.0°). The Fe−P distances of 2.4651(3) and 2.4659(3) Å are similar to the other $[[Ph_2BP_2^{Ph}]FeX_2]$-

[ASN] described in this chapter. The Fe−C distances of 2.1079(3) and 2.1833(3) Å are not significantly different from the average 2.103 Å reported for iron alkyl complexes containing sp^3-alkyl ligands.

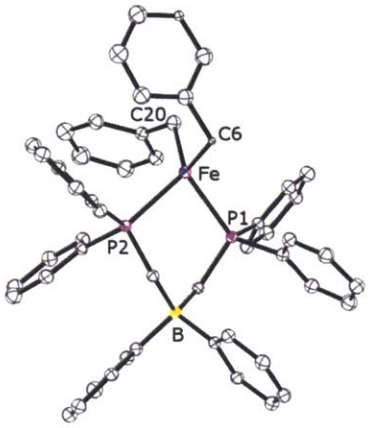

Selected Bond Lengths (Å) and Angles (°)
Fe–P1 = 2.4651(3)
Fe–P2 = 2.4659(3)
Fe–C6 = 2.1833(3)
Fe–C20 = 2.1079(3)
C6–Fe–C20 = 111.06(3)
P1–Fe–P2 = 88.76(3)

Figure 5.11 Solid-state structure of **5.9**. Thermal ellipsoids are drawn at 40% probability. ASN counterion and hydrogen atoms are omitted for clarity.

Encouraged by this result, we turned to the [$Ph_2BP_2^{tBu}$] ligand scaffold to isolate a three-coordinate iron alkyl complex. Treatment of **5.5** with two equiv of BnMgCl in OEt_2 at −35 °C resulted in an immediate color change from yellow to red and the formation of a white precipitate. After stirring for 30 min, a red powder was isolated in ca. 60% yield (Scheme 5.12). This species, assigned as the three-coordinate [$Ph_2BP_2^{tBu}$]FeBn complex (**5.10**), is a paramagnetic, $S = 2$ species (μ_{eff} = 5.0 μ_B, C_6D_6, 25 °C), with ^{1}H NMR resonances ranging from 65 to −115 ppm. An X-ray crystallographic study confirmed the assignment of **5.10** as the three-coordinate iron alkyl species. Complex **5.10** crystallizes in the monoclinic space group $P2_1/n$, with one molecule per asymmetric unit (Figure 5.12). The sum of the angles about the iron center is 359.86(3)°, indicating a planar geometry. As a consequence of the lower coordination number in **5.10**, the P−Fe−P angle expands to 101.54(3)°, as compared to 83.30(3)° for four-coordinate **5.9**. The P−Fe−C angles are inequivalent; the P1−Fe−C12 angle is 132.73(3)° and the P2−Fe−C12 angle is 125.59(3)°. This asymmetry can be attributed to the steric demands of the benzyl ligand and has been observed for other three- and four-coordinate iron alkyl complexes bearing bulky alkyl substituents.[21,27,31,33,38,39,85–90] For example, the three-coordinate alkyl complex reported

by Holland, $L^{Me}Fe(CH_2{}^iPr)$ (L^{Me} = 2,4-bis(2,6-diisopropylphenylimido)pentyl), displays N–Fe–C angles of 124.999(3)° and 140.720(3)°.[39] The Fe–C distance of 2.0429(3) Å for **5.10** is shorter than that of **5.9** (avg = 2.1456 Å), but is within the range of other three-coordinate iron alkyl complexes (1.94 – 2.71 Å).[37–39,89]

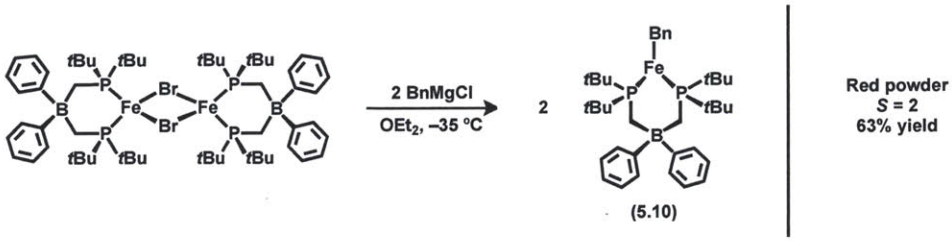

Scheme 5.12 Treatment of **5.5** with 2 equiv of BnMgCl yields the benzyl complex **5.10**.

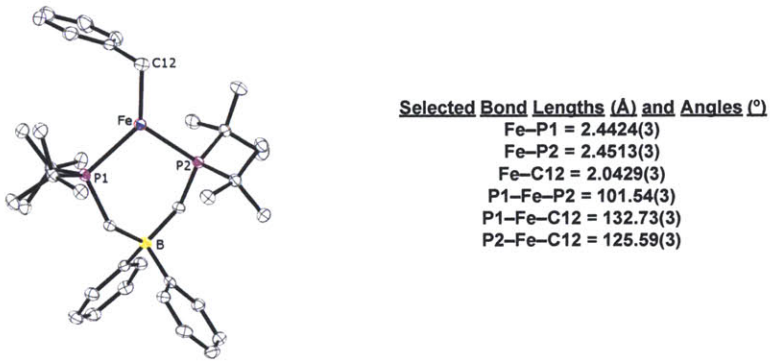

Figure 5.12 Solid-state structure of **5.10**. Thermal ellipsoids are drawn at 40% probability. Hydrogen atoms are omitted for clarity.

Treatment of benzene solutions of **5.9** and **5.10** with either 1 equiv or an excess of H_2 at room temperature in the presence or absence of phosphine additives (PMe_3, PMe_2Ph or PPh_3) resulted in an intractable mixture of products. The phosphines $PMePh_2$ and P^tBu_2Me were identified as major components of the reaction mixtures, formed by $B-C_{alkyl}$ bond cleavage of $[Ph_2BP_2^{Ph}]$ and $[Ph_2BP_2^{tBu}]$, respectively.

5.7 Pitfalls of the $[Ph_2BP_2^R]Fe$ Systems

Given the success in preparing a variety of $[Ph_2BP_2^R]Fe$ systems it is worth separately discussing the synthetic complications encountered during their preparation and subse-

quent chemistry. Although a promising starting point for the preparation of low-coordinate species, isolation of complexes of the type $[Ph_2BP^{tBu}_2]FeX$ has proven to be difficult as a result of the solubility of the desired products and their side-products in a range of solvents, including $O(SiMe_3)_2$ and $SiMe_4$. In addition to the solubility problem, a persistent and ill-defined decomposition pathway exists for these species, preventing isolation. For example, treatment of **5.5** with one equiv of LiNHAr (Ar = 2,6-diisopropylphenyl) results in a color change from amber to bright orange with concomitant formation of a white precipitate. A ^1H NMR spectrum of the crude reaction mixture indicates the formation of a new paramagnetic species, assumed to be the three-coordinate $[Ph_2BP^{tBu}_2]FeNHAr$ by comparison to the ^1H NMR spectrum of **5.10**. Also prominent in the spectrum is the presence of free NH_2Ar; upon standing in solution, the purported three-coordinate anilido species decays over a period of hours and the concentrations of free NH_2Ar and other unidentified products increase. In the crude ^{31}P NMR spectrum, both free $[Ph_2BP^{tBu}_2]$ and PMe^tBu_2 are present; accordingly, a dark solid presumed to be Fe^0 can be seen precipitating from solution. These observations are also true of the reaction between **5.5** and TlOAr (Ar = 2,6-diisopropylphenyl).

Reasoning that a sterically protected nitrogen center would give rise to a more stable three-coordinate amide complex, **5.5** was treated with two equiv of $LiN(p\text{-tol})_2$ in THF. Immediately upon addition, a dark purple solution formed with a white precipitate. A crude ^1H NMR spectrum indicated the clean formation of a new paramagnetic species. However, a partial X-ray crystallographic analysis suggests that the species is the dimeric iron imido complex, as shown in Figure 5.13 (left). Repeating the reaction in a non-coordinating solvent such as C_6H_6 gives the same product.

As discussed in the previous sections, further chemistry with the isolated $[Ph_2BP^R_2]Fe$ complexes is hampered by $B-C_{alkyl}$ bond cleavage to give free $PMeR_2$ as a major product in inconsistent quantities. For **5.4** in particular, treatment with various reductants (vide supra) results in the formation of $PMePh_2$ and Fe^0. A partial X-ray crystallographic analysis indicates that $[Ph_2BP^{Ph}_2]_2Fe$ is also produced (Figure 5.13, right).

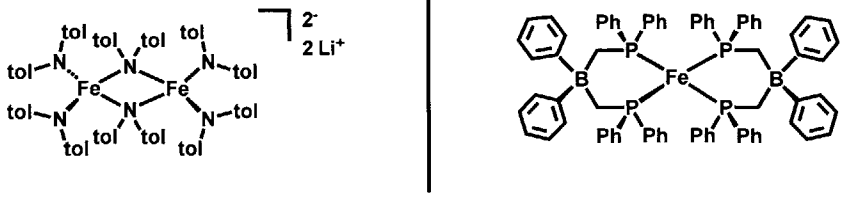

Figure 5.13 Preliminary X-ray analyses suggest that: (*left*) Treatment of **5.5** with LiN(*p*-tol)$_2$ results in dechelation of [$Ph_2BP_2^{tBu}$] and formation of an homoleptic iron amido species. (*right*) Reduction of **5.4** results in a mixture of products, one of which is the homoleptic bis(phosphine)borate complex.

5.8 Conclusions and Future Work

In this chapter, the preparation and characterization of an iron alkyl complex supported by the tris(phosphine)borate ligand [$PhBP_3^{Ph}$] was described. In contrast to the related [$PhBP_3^{iPr}$]FeMe complex, hydrogenation of [$PhBP_3^{Ph}$]FeMe in the presence of PMe_2Ph yields a transient dihydrogen hydride species, as evidenced by a short T_1 relaxation time of 32 ms. Complex [$PhBP_3^{Ph}$]FeMe is a very slow but competent hydrogenation catalyst, achieving a TOF of 3.3 h^{-1} for the conversion of 1-hexene to hexane. In an effort to access more robust and active catalysts, the coordination chemistry of iron bis(phosphine)borate complexes was explored. The less sterically hindered ligand, $[Ph_2BP_2^{Ph}]_2$, allowed for access of bis(alkyl), bis(anilido) and bis(aryloxide) 'ate' complexes; the bulkier ligand, [$Ph_2BP_2^{tBu}$], supported the formation of an unusual three-coordinate iron alkyl complex. Both ligand sets suffered from similar B$-C_{alkyl}$ bond cleavage decomposition pathways and both ligands could be easily displaced from iron under reducing conditions or by the introduction of a strongly coordinating ligand. While the identity of the intermediate hydride species in the tris(phosphine)borate system remains an interesting question, the lack of experimental methods for the characterization of paramagnetic hydride and dihydrogen complexes constitutes a major hurdle.

As mentioned before, ENDOR spectroscopy has been a useful tool in identifying the presence of Fe$-$H bonds in nitrogenase intermediates.[7] Recently, this technique has been used by the Schrock and Peters groups to characterize paramagnetic molybdenum hydride and iron dihydrogen complexes, respectively.[91,92] Treatment of [$HIPTN_3N$]Mo(N_2)

([HIPTN$_3$N] = ((HIPT)NCH$_2$CH$_2$)$_3$N^{3-}, HIPT = 3,5-(2,4,6-^{i}Pr$_3$C$_6$H$_2$)$_2$C$_6$H$_3$) with H_2 generates an unstable "[HIPTN$_3$N]Mo(H_2)" species that undergoes facile heterolytic cleavage to yield [[HIPTN$_3$N]Mo(H)]$^-$ and H^+ at low temperature, as identified by an EPR and $^{1/2}$H/^{14}N ENDOR studies.[91] The stable dihydrogen adduct [SiP$_3^{iPr}$]Fe(H_2) ([SiP$_3^{iPr}$] = (2-^{i}Pr$_2$PC$_6$H$_4$)$_3$Si$^-$), generated by addition of H_2 to [SiP$_3^{iPr}$]Fe(N_2), is a rare example of a well-characterized, open-shell metal complex that binds H_2. EPR and ENDOR data, as well as an X-ray structure analysis, support the assignment of this species as an iron(I) dihydrogen complex and not an iron(I) monohydride or an iron(III) dihydride species.[92] Thus, both EPR and ENDOR spectroscopic studies could provide further characterization of the intermediate hydride species generated upon addition of H_2 to [PhBP$_3^{Ph}$]FeMe.

5.9 Experimental Methods

5.9.1 General Considerations

All manipulations were carried out using standard Schlenk or glovebox techniques under a dinitrogen atmosphere. Unless otherwise noted, solvents were dried and deoxygenated by sparging with argon and passing through activated alumina in a solvent purification system from SG Waters USA, LLC (Nashua, NH). Non-halogenated solvents were tested with a standard purple solution of sodium benzophenone ketyl in tetrahydrofuran in order to confirm effective oxygen and moisture removal. Ethanol was stirred and distilled over calcium sulfate and stored over activated 3-Å molecular sieves. [PhBP$_3^{Ph}$]FeCl,[24] [Ph$_2$BP$_2^{Ph}$][ASN],[93] [Ph$_2$BP$_2^{tBu}$][Tl],[51] and TlOAr[94] (Ar = 2,6-diisopropylphenyl) were prepared according to literature methods. LiNHAr (Ar = 2,6-diisopropylphenyl) was prepared from 2,6-diisopropylaniline and *n*-butyllithium in *n*-pentane. 2,6-Diisopropylaniline was purchased from Aldrich and distilled prior to use. All other reagents were purchased from commercial suppliers and used without further purification. Elemental analyses were performed by Midwest Microlab, LLC (Indianapolis, IN) and Robertson Microlit Laboratories, Inc (Ledgewood, NJ). Deuterated solvents were purchased from Cambridge Isotope Laboratories, Inc., degassed, and dried over activated 3-Å molecular sieves prior to use.

5.9.2 Spectroscopic Measurements

Varian 300 and 500 MHz spectrometers were used to record ^{1}H, ^{31}P and ^{205}Tl NMR spectra at room temperature, unless otherwise noted. ^{1}H NMR chemical shifts were referenced to the residual solvent peaks. ^{31}P NMR chemical shifts were referenced to external 85% phosphoric acid (δ = 0 ppm). ^{205}Tl NMR chemical shifts were referenced to external $Tl(NO_3)$ (δ = 0 ppm). Solution magnetic moment measurements were determined by the method of Evans.[95,96] To determine the error in these measurements, an error analysis was performed and the error bars were established at 95% confidence using regression analysis. The values are reported to two significant figures and are understood to have an error of $\pm$ 0.1 μB. T_1 values were determined by fitting the pulse-recovery ^{1}H spectra at room temperature using the T_1 calculation protocols in Varian's VnmrJ software.

5.9.3 Electrochemistry

Electrochemical measurements were carried out in a glovebox under a dinitrogen atmosphere in a one-compartment cell using a CH Instruments 630-C Electrochemistry Analyzer with CHI Version 8.09 software package. A glassy carbon electrode and platinum wire were used as the working and auxiliary electrodes, respectively. The reference electrode was $Ag/AgNO_3$ in THF. Solutions of electrolyte (0.4 M $[^{n}Bu_4N][PF_6]$) and analyte were prepared in a glovebox. Experiments were conducted at room temperature. The ferrocene couple Fc/Fc^{+} was used as an external reference.

5.9.4 Magnetic Measurements

Magnetic susceptibility measurements of powdered samples were performed on a Quantum Design SQUID magnetometer at 0.5 T between 4 and 300 K for all samples. The samples were measured in gelatin capsules, and the diamagnetic contribution from the sample container was subtracted from the experimental data. Pascal's constants were used to subtract diamagnetic contributions, yielding paramagnetic susceptibilities. JulX was used for the simulation and analysis of magnetic susceptibility data.[52]

5.9.5 Preparation of [PhBP$^{Ph}_3$]FeMe (5.1)

A C_6H_6 slurry of Me_2Mg (199.2 mg, 3.69 mmol) was added to a solution of [PhBP$^{Ph}_3$]FeCl (286.7 mg, 0.37 mmol) in 10 mL of C_6H_6. After 2 h, the reaction mixture was filtered through Celite and the filtrate lyophilized. The resulting powder was extracted into toluene, filtered through Celite and the volatiles removed in vacuo to yield an amber solid (241.4 mg, 86%). X-ray quality crystals were grown by vapor diffusion of pentane into a concentrated C_6H_6 solution. ^{1}H NMR (300 MHz, C_6D_6) δ 47.43, 22.60, 20.76, 2.77, −12.79, −53.25, −53.25, −105.89. μ_{eff} (C_6D_6, Evans method, 25 °C): 5.2 μB. Anal. Calcd. for $C_{46}H_{44}BFeP_3$: C, 73.04; H, 5.86; N, 0. Found: C, 72.72; H, 5.89; N, 0.

5.9.6 In Situ Generation of [PhBP$^{Ph}_3$]Fe(PMe$_2$Ph)(H)(H$_2$) (5.2)

A J. Young capped NMR tube was charged with **5.1** (44.3 mg, 58.56 μmol), PMe_2Ph (8.4 μL, 58.80 μmol) and 0.5 mL THF-d_8. The tube sealed and inverted to ensure complete mixing. The solution was degassed by three freeze/pump/thaw cycles, and the NMR tube was pressurized with 1 atm of H_2. **5.1** was consumed after 10 min, as determined by ^{1}H NMR spectroscopy. ^{1}H NMR (500 MHz, THF-d_8) δ 7.75 – 7.63 (m, 4H), 7.53 – 7.35 (m, 14H), 7.21 – 7.13 (m, 3H), 7.03 – 6.86 (m, 18H), 1.53 (s, 6H), 0.83 (s, 6H), −9.95 (br s, 3H). ^{31}P$\{^1$H$\}$ NMR (202 MHz, THF-d_8) δ 61.6 (s, 3P), 32.9 (s, 1P).

5.9.7 Preparation of [PhBP$^{Ph}_3$]Fe(PMe$_2$Ph) (5.3)

Sodium (3.0 mg, 0.13 mmol) and mercury (489.2 mg) were stirred vigorously with THF (5 mL). A solution of [PhBP$^{Ph}_3$]FeCl (82.5 mg, 0.11 mmol) and PMe_2Ph (45.4 μL, 0.319 mmol) in THF (5 mL) was added and the reaction mixture stirred for 12 h at room temperature. The resulting dark brown mixture was decanted from the amalgam and the solvent removed in vacuo. The residue was extracted into C_6H_6 and filtered through Celite and lyophilized. The resulting brown powder was taken up in minimal benzene and pentane added to precipitate a dark yellow microcrystalline solid (60.6 mg, 65%). X-ray quality crystals were grown by vapor diffusion of pentane into a concentrated C_6H_6 solution. ^{1}H NMR (400 MHz, C_6D_6) δ 94.59 (br), 92.61 (br), 15.45, 13.77, 11.82, 8.71, 7.63, −1.23,

−5.60, −8.70. μ_{eff} (C_6D_6, Evans method, 25 °C): 4.1 μB. Anal. Calcd for $C_{53}H_{52}BFeP_4$: C, 72.38; H, 5.96. Found: C, 72.15; H, 5.88.

5.9.8 Preparation of [[$Ph_2BP_2^{Ph}$]$FeCl_2$][ASN] (5.4)

To a slurry of [$Ph_2BP_2^{Ph}$][ASN] (1.8707 g, 2.71 mmol) in THF (10 mL) was added a slurry of $FeCl_2$ (0.3514 g, 2.77 mmol) in THF (10 mL) and the reaction stirred 12 h at room temperature. The reaction mixture was filtered to collect the white precipitate and the solids were thoroughly washed with THF (3 x 5 mL) and CH_2Cl_2 (3 x 5 mL) Yield: 2.0555 g, 93%. ^{1}H NMR (300 MHz, d_6-acetone) δ 120.0, 15.16, 12.59, 8.19, 7.47, 3.78, 2.39, −4.16. μ_{eff} (SQUID): 5.1 μB. Anal. Cald. for $C_{46}H_{50}BCl_2FeNP_2$: C, 67.67; H, 6.17; N, 1.72. Found: C, 67.46; H, 6.37; N, 1.73.

5.9.9 Preparation of {[$Ph_2BP_2^{tBu}$]FeBr}$_2$ (5.5)

A THF slurry of $FeBr_2$ (84.2 mg, 0.39 mmol) was added to a THF solution (10 mL) of [$Ph_2BP_2^{tBu}$][Tl] (258.2 mg, 0.38 mmol) and stirred for 12 h at room temperature. The reaction mixture was filtered through Celite and the solvent removed in vacuo. The residue was extracted into hot C_6H_6, filtered through Celite and lyophilized to yield a dark yellow powder (174.9 mg, 75%). ^{1}H NMR (400 MHz, C_6D_6) δ 24.94, 14.26, 12.82, 8.65 (br), 1.56, 1.03, −5.59. Anal. Cald. for $C_{60}H_{100}B_2Br_2Fe_2P_4$: C, 58.19; H, 8.14. Elemental analysis results were consistently low in carbon and hydrogen. Found: C, 52.01; H, 7.23. Drying of the samples under vacuum at 60 °C and repeated measurements of independently prepared material gave similar results. Because we have crystal structure information on **5.5** and a clean ^{1}H NMR spectrum, we are confident of its identity and the deviations between the calculated and experimental values may arise from NMR silent salts that were unable to be washed away or from oxidation of the material, as **5.5** is quite air-sensitive.

5.9.10 Preparation of [[$Ph_2BP_2^{Ph}$]Fe(NH(Ar))$_2$][ASN] (5.6)

A solution of LiNHAr (Ar = 2,6-diisopropylphenyl) (46.5 mg, 0.25 mmol) in THF (5 mL) cooled to −35 °C was added dropwise to a slurry of **5.4** (103.0 mg, 0.13 mmol) in THF

(10 mL) cooled to −35 °C. The reaction mixture gradually turned dark orange and was stirred for 3 h at room temperature. The solvent was removed in vacuo and the residue was triturated with C_6H_6. The resulting orange solids were dissolved in a minimal amount of CH_2Cl_2 and filtered through Celite. Diffusion of OEt_2 into a concentrated CH_2Cl_2 solution at −35 °C yielded orange crystals, which were separated from the mother liquor, washed with cold OEt_2 and dried (0.0728 g, 53%). ^{1}H NMR (500 MHz, CD_2Cl_2) δ 109.73, 47.66, 15.64, 13.46, 7.21, 6.78, 6.48, 2.72, 1.91, −4.64, −79.70. μ_{eff} (CD_2Cl_2, Evans method, 25 °C): 5.4 μB. Anal. Calcd for $C_{70}H_{86}BFeN_3P_2$: C, 76.57; H, 7.89; N, 3.83. Found: C, 76.31; H, 7.97; N, 3.88.

5.9.11 Preparation of [[$Ph_2BP_2^{Ph}$]Fe(Cl)(OAr)][ASN] (5.7)

A slurry of TlOAr (Ar = 2,6-diisopropylphenyl) (46.8 mg, 0.12 mmol) in THF (5 mL) cooled to −35 °C was added dropwise to a slurry of **5.4** (100.0 mg, 0.12 mmol) in THF (10 mL) at −35 °C. The resulting bright yellow slurry was stirred for 6 h at room temperature. The reaction mixture was filtered through Celite and the solvent removed in vacuo. The residue was triturated with C_6H_6, dissolved in a minimal amount of THF and filtered. Diffusion of OEt_2 into a concentrated THF solution −35 °C yielded bright yellow crystals, which were separated from the mother liquor, washed with cold OEt_2 and dried (0.088 g, 75%). Crystals grown in this manner were suitable for X-ray diffraction studies. ^{1}H NMR (300 MHz, THF-d_8) δ 102.07, 55.83, 22.11, 14.40, 13.83, 10.62, 8.98, 8.12, 6.75, 3.98, 1.92, 0.88, −4.30, −6.14, −42.13. μ_{eff} (THF-d_8, Evans method, 25 °C): 5.1 μB. Anal. Calcd for $C_{58}H_{67}BClFeNOP_2$: C, 72.70; H, 7.05; N, 1.46. Found: C, 72.50; H, 7.23; N, 1.45.

5.9.12 Preparation of [[$Ph_2BP_2^{Ph}$]Fe($OAr)_2$][ASN] (5.8)

A slurry of TlOAr (Ar = 2,6-diisopropylphenyl) (97.3 mg, 0.25 mmol) in THF (5 mL) cooled to −35 °C was added dropwise to a slurry of **5.4** (103.6 mg, 0.13 mmol) in THF (10 mL) at −35 °C. The resulting orange slurry was stirred for 6 h at room temperature. The reaction mixture was filtered through Celite and the solvent removed in vacuo. The residue

was triturated with OEt_2, dissolved in a minimal amount of CH_2Cl_2 and filtered. Diffusion of pentane into a concentrated CH_2Cl_2 solution at −35 °C yielded orange crystals, which were separated from the mother liquor, washed with cold pentane and dried (73.4 g, 53%). Crystals grown in this manner were suitable for X-ray diffraction studies. ^{1}H NMR (300 MHz, CD_2Cl_2) δ 96.50, 48.60, 15.25, 7.45, 7.36, 7.03, 6.70, 5.15, 2.85, 1.99, 1.30, 1.16, 0.88, −4.83, −40.96. μ_{eff} (CD_2Cl_2, Evans method, 25 °C): 5.1 μB. Anal. Calcd for $C_{70}H_{84}BFeNO_2P_2$: C, 76.43; H, 7.70; N, 1.27. Found: C, 76.23; H, 7.62; N, 1.31.

5.9.13 Preparation of [$[Ph_2BP_2^{Ph}]Fe(Bn)_2$][ASN] (5.9)

To a 1,4-dioxane:OEt_2 (1:1, 10 mL) slurry of **5.4** (102.6 mg, 0.13 mmol) cooled to −35 °C was slowly added BnMgCl (125.7 μL, 2M in THF, 0.25 mmol). The reaction mixture gradually turned orange and was stirred for 1 h at room temperature. The mixture was filtered and the solvent was removed in vacuo. The resulting orange solids were dissolved in a minimal amount of THF and filtered through Celite. Diffusion of OEt_2 into a concentrated THF solution at −35 °C yielded red crystals, which were separated from the mother liquor, washed with cold OEt_2 and dried (0.0699 g, 60%). X-ray quality crystals were grown by diffusion of OEt_2 into a concentrated CH_2Cl_2 solution. ^{1}H NMR (500 MHz, CD_2Cl_2) δ 133.36, 35.92, 15.49, 11.64, 8.30, 7.40, 2.63, −5.45, −82.71. Anal. Calcd for $C_{60}H_{64}BFeNP_2 \cdot C_4H_8O_2$: C, 75.67; H, 7.14; N, 1.38. Found: C, 75.29; H, 6.71; N, 1.54.

5.9.14 Preparation of [$Ph_2BP_2^{tBu}$]FeBn (5.10)

To a solution of **5.5** (56.7 mg, 0.46 mmol) in OEt_2 (10 mL) cooled to −35 °C was slowly added BnMgCl (45.8 μL, 2M in THF, 0.92 mmol). A white precipitate formed immediately and the solution color changed from yellow to red. The reaction mixture was stirred for 30 min at room temperature and then filtered through Celite. Concentrating the solution and cooling to −35 °C yielded red microcrystalline material; the crystals were separated from the mother liquor, washed with cold OEt_2 and dried (36.3 mg, 63%). Crystals grown in this manner were suitable for X-ray diffraction studies. ^{1}H NMR (500 MHz, C_6D_6) δ 63.35, 49.91, 26.68, 22.62, 1.10, −5.35, −45.62, −48.35, −114.58. μ_{eff} (C_6D_6, Evans method,

25 °C): 5.0 μB. Anal. Calcd for $C_{37}H_{57}BFeP_2$: C, 70.49; H, 9.11. Found: C, 69.95; H, 8.76.

5.9.15 X-ray Crystallographic Details

Single crystals of **5.1** and **5.3** were obtained by vapor diffusion of pentane into a C_6H_6 solution, crystals of **5.7** were grown by vapor diffusion of OEt_2 into a concentrated THF solution at −35 °C, crystals of **5.9** were obtained by vapor diffusion of OEt_2 into a concentrated CH_2Cl_2 solution at −35 °C, crystals of **5.10** were grown by cooling a concentrated OEt_2 solution to −35 °C. Low-temperature single crystal X-ray diffraction studies were carried out at the MIT Crystallography Facility on a Bruker Kappa Apex II diffractometer with Mo Kα radiation (λ = 0.71073 Å). Crystals were coated with Paratone-N oil and mounted on in fiber loops. Structures were solved by direct or Patterson methods using SHELXS[97] and refined against F2 on all data by full-matrix least squares with SHELXL-97[98] using established refinement techniques.[99] All non-hydrogen atoms were refined anisotropically. All hydrogen atoms were included into the model at geometrically calculated positions and refined using a riding model. The isotropic displacement parameters of all calculated hydrogen atoms were fixed to 1.2 times the U values of the atoms they are linked to (1.5 times for methyl groups). Thermal ellipsoid diagrams were created using Olex2.[100] The structures of **5.3** and **5.7** contained voids with disordered solvent molecules. The program SQUEEZE[101] as implemented in Platon[102] was used to remove the contribution of the disordered solvent to the structure factors. The crystallographic details for **5.1**, **5.3**, **5.7** and **5.9 – 5.10** are summarized in Tables 5.2 and 5.3.

	5.1	**5.3**
Formula	$C_{46}H_{44}BFeP_3$	$C_{54.75}H_{54}BFeP_4$
Formula Weight	756.38	902.52
Temperature/K	100(2)	100(2)
Crystal syst.	Monoclinic	Monoclinic
Space group	*C2/c*	$P2_1/c$
Color	Amber	Yellow
a/Å	38.994(3)	16.1410(9)
b/Å	13.1738(8)	15.1963(8)
c/Å	16.3159(10)	20.4825(11)
α/°	90	90
β/°	109.762(2)	107.1400(10)
γ/°	90	90
V/^{3}	7887.9(9)	4800.9(5)
ρ (calc.)/(gcm^{-1})	1.274	1.249
Z	8	4
No. refl.	84906	105871
No. unique refl.	9785	13477
R_{int}	0.0711	0.0446
R_1 (all data)[a]	0.0595	0.0707
wR_2 (all data)[b]	0.1089	0.1763
R_1 [(I >2σ)]	0.0381	0.0514
wR_2 [(I >2σ)]	0.0922	0.1539
GOF[c]	1.076	1.075

Table 5.2 Crystallographic summary for **5.1** and **5.3**. [a]$R_1 = \Sigma||F_0 - |F_e||/\Sigma|F_0|$. [b]$wR_2 = (\Sigma[w(F_0^2 - F_e^2)^2]/\Sigma[w(F_0^2)^2])^{1/2}$. [c]$GOF = (\Sigma[w(F_0^2 - F_e^2)^2]/(n-p))^{1/2}$ where n is the number of data and p is the number of parameters refined.

	5.7	**5.9** · 3 CH_2Cl_2	**5.10**
Formula	$C_{64}H_{82}BClFeNO_{2.50}P_2$	$C_{63}H_{70}BCl_6FeNP_2$	$C_{37}H_{57}BFeP_2$
Formula Weight	1069.35	1182.50	630.43
Temperature/K	100(2)	100(2)	100(2)
Crystal syst.	Triclinic	Triclinic	Monoclinic
Space group	$P\bar{1}$	$P\bar{1}$	$P2_1/n$
Color	Orange	Orange	Red
a/Å	10.4895(5)	11.7741(5)	11.9437(9)
b/Å	13.7377(7)	15.7524(8)	18.9369(12)
c/Å	20.1245(10)	16.5039(7)	16.4215(12)
α/°	93.828(2)	102.8290(10)	90
β/°	94.6140(10)	93.0330(10)	108.143(2)
γ/°	97.3960(10)	95.8180(10)	90
V/^{3}	2857.8(2)	2960.2(2)	3529.5(4)
ρ (calc.)/(gcm^{-1})	1.243	1.327	1.186
Z	2	2	4
No. refl.	13581	56027	53847
No. unique refl.	11131	13035	7778
R_{int}	0.0464	0.0454	0.0664
R_1 (all data)[a]	0.0539	0.0875	0.0660
wR_2 (all data)[b]	0.1765	0.1930	0.1130
R_1 [(I >2σ)]	0.0444	0.0674	0.0418
wR_2 [(I >2σ)]	0.01591	0.1757	0.0997
GOF[c]	1.073	1.022	1.033

Table 5.3 Crystallographic summary for **5.7**, **5.9** and **5.10**. [a]$R_1 = \Sigma||F_0 - |F_e||/\Sigma|F_0|$. [b]$wR_2 = (\Sigma[w(F_0^2 - F_e^2)^2]/\Sigma[w(F_0^2)^2])^{1/2}$. [c]$GOF = (\Sigma[w(F_0^2 - F_e^2)^2]/(n-p))^{1/2}$ where n is the number of data and p is the number of parameters refined.

5.10 Bibliography

[1] McGrady, G. S.; Guilera, G. *Chem. Soc. Rev.* **2003**, *32*, 383–392.

[2] Howard, J. B.; Rees, D. C. *Chem. Rev.* **1996**, *96*, 2965–2982.

[3] Burgess, B. K.; Lowe, D. J. *Chem. Rev.* **1996**, *96*, 2983–3011.

[4] Eady, R. R. *Chem. Rev.* **1996**, *96*, 3013–3030.

[5] Thorneley, R. N. F.; Eady, R. R.; Lowe, D. J. *Nature* **1978**, *272*, 557–558.

[6] Leigh, G. J.; McMahon, C. N. *J. Organomet. Chem.* **1995**, *500*, 219–225.

[7] Igarashi, R. Y.; Laryukhin, M.; Dos Santos, P. C.; Lee, H.-I.; Dean, D. R.; Seefeldt, L. C.; Hoffman, B. M. *J. Am. Chem. Soc.* **2005**, *127*, 6231–6241.

[8] Fontecilla-Camps, J. C.; Volbeda, A.; Cavazza, C.; Nicolet, Y. *Chem. Rev.* **2007**, *107*, 4273–4303.

[9] Wright, J. A.; Turrell, P. J.; Pickett, C. J. *Organometallics* **2010**, *29*, 6146–6156.

[10] Nakazawa, H.; Itazaki, M. *Top. Organomet. Chem.* **2011**, *33*, 27–81.

[11] Junge, K.; Schröder, K.; Beller, M. *Chem. Commun.* **2011**, *47*, 4849–4859.

[12] Frankel, E. N.; Emken, E. A.; Peters, H. M.; Davison, V. L.; Butterfield, R. O. *J. Org. Chem.* **1964**, *29*, 3292–3297.

[13] Frankel, E. N.; Emken, E. A.; Davison, V. L. *J. Org. Chem.* **1965**, *30*, 2739–2745.

[14] Cais, M.; Maoz, N. *J. Chem. Soc. A* **1971**, *11*, 1811–1820.

[15] Schroeder, M. A.; Wrighton, M. S. *J. Am. Chem. Soc.* **1976**, *98*, 551–558.

[16] Bianchini, C.; Meli, A.; Peruzzini, M.; Frediani, P.; Bohanna, C.; Esteruelas, M. A.; Oro, L. A. *Organometallics* **1992**, *11*, 138–145.

[17] Chiang, K. P.; Scarborough, C. C.; Horitani, M.; Lees, N. S.; Ding, K.; Dugan, T. R.; Brennessel, W. W.; Bill, E.; Hoffman, B. M.; Holland, P. L. *Angew. Chem. Int. Ed.* **2012**, *51*, 3658–3662.

[18] Yu, Y.; Sadique, A. R.; Smith, J. M.; Dugan, T. R.; Cowley, R. E.; Brennessel, W. W.; Flaschenriem, C. J.; Bill, E.; Cundari, T. R.; Holland, P. L. *J. Am. Chem. Soc.* **2008**, *130*, 6624–6638.

[19] Bart, S. C.; Lobkovsky, E.; Chirik, P. J. *J. Am. Chem. Soc.* **2004**, *126*, 13794–13807.

[20] Bouwkamp, M. W.; Bowman, A. C.; Lobkovsky, E.; Chirik, P. J. *J. Am. Chem. Soc.* **2006**, *128*, 13340–13341.

[21] Daida, E. J.; Peters, J. C. *Inorg. Chem.* **2004**, *43*, 7474–7485.

[22] Brown, S. D.; Peters, J. C. *J. Am. Chem. Soc.* **2004**, *126*, 4538–4539.

[23] Betley, T. A.; Peters, J. C. *J. Am. Chem. Soc.* **2003**, *125*, 10782–10783.

[24] Brown, S. D.; Betley, T. A.; Peters, J. C. *J. Am. Chem. Soc.* **2003**, *125*, 322–323.

[25] Betley, T. A.; Peters, J. C. *Inorg. Chem.* **2003**, *42*, 5074–5084.

[26] Akita, M.; Shirasawa, N.; Hikichi, S.; Moro-oka, Y. *Chem. Commun.* **1998**, 973–974.

[27] Fernández, I.; Trovitch, R. J.; Lobkovsky, E.; Chirik, P. J. *Organometallics* **2008**, *27*, 109–118.

[28] Popescu, C. V.; Mock, M. T.; Stoian, S. A.; Dougherty, W. G.; Yap, G. P. A.; Riordan, C. G. *Inorg. Chem.* **2009**, *48*, 8317–8324.

[29] Kisko, J. L.; Hascall, T.; Parkin, G. *J. Am. Chem. Soc.* **1998**, *120*, 10561–10562.

[30] Bouwkamp, M. W.; Bart, S. C.; Hawrelak, E. J.; Trovitch, R. J.; Lobkovsky, E.; Chirik, P. J. *Chem. Commun.* **2005**, 3406–3408.

[31] Jové, F. A.; Pariya, C.; Scoblete, M.; Yap, G. P. A.; Theopold, K. H. *Chem. Eur. J.* **2011**, *17*, 1310–1318.

[32] Scott, J.; Gambarotta, S.; Korobkov, I.; Budzelaar, P. H. M. *Organometallics* **2005**, *24*, 6298–6300.

[33] Hermes, A. R.; Girolami, G. S. *Organometallics* **1987**, *6*, 763–768.

[34] Lee, H. K.; Luo, B.-S.; Mak, T. C. W.; Leung, W.-P. *J. Organomet. Chem.* **1995**, *489*, C71–C73.

[35] Leung, W.-P.; Lee, H. K.; Weng, L.-H.; Luo, B.-S.; Zhou, Z.-Y.; Mak, T. C. W. *Organometallics* **1996**, *15*, 1785–1792.

[36] Fryzuk, M. D.; Leznoff, D. B.; Ma, E. S. F.; Rettig, S. J.; Young, V. G., Jr *Organometallics* **1998**, *17*, 2313–2323.

[37] Sciarone, T. J. J.; Meetsma, A.; Hesssen, B.; Teuben, J. H. *Chem. Commun.* **2002**, 1580–1581.

[38] Smith, J. M.; Lachicotte, R. J.; Holland, P. L. *Organometallics* **2002**, *21*, 4808–4814.

[39] Vela, J.; Vaddadi, S.; Cundari, T. R.; Smith, J. M.; Gregory, E. A.; Lachicotte, R. J.; Flaschenriem, C. J.; Holland, P. L. *Organometallics* **2004**, *23*, 5226–5239.

[40] Bart, S. C.; Hawrelak, E. J.; Schmisseur, A. K.; Lobkovsky, E.; Chirik, P. J. *Organometallics* **2004**, *23*, 237–246.

[41] Bouwkamp, M. W.; Lobkovsky, E.; Chirik, P. J. *J. Am. Chem. Soc.* **2005**, *127*, 9660–9661.

[42] Brown, S. D. The chemistry of tris(phosphine)borate supported iron-nitrogen multiply-bonded linkages. Ph.D. thesis, California Institute of Technology, 2005.

[43] Morris, R. H. *Coord. Chem. Rev.* **2008**, *252*, 2381–2394.

[44] Crabtree, R. H.; Lavin, M.; Bonneviot, L. *J. Am. Chem. Soc.* **1986**, *108*, 4032–4037.

[45] Hamilton, D. G.; Crabtree, R. H. *J. Am. Chem. Soc.* **1988**, *110*, 4126–4133.

[46] Luo, X. L.; Crabtree, R. H. *Inorg. Chem.* **1990**, *29*, 2788–2791.

[47] Gusev, D. G.; Hübener, R.; Burger, P.; Orama, O.; Berke, H. *J. Am. Chem. Soc.* **1997**, *119*, 3716–3731.

[48] Thomas, J. C.; Peters, J. C. *J. Am. Chem. Soc.* **2003**, *125*, 8870–8888.

[49] Betley, T. A.; Peters, J. C. *Angew. Chem. Int. Ed.* **2003**, *42*, 2385–2389.

[50] Lu, C. C.; Peters, J. C. *J. Am. Chem. Soc.* **2002**, *124*, 5272–5273.

[51] Thomas, J. C.; Peters, J. C. *Inorg. Chem.* **2003**, *42*, 5055–5073.

[52] Bill, E. JulX. `http://ewww.mpi-muelheim.mpg.de/bac/logins/bill/julX_en.php`.

[53] Smith, J. M.; Lachicotte, R. J.; Holland, P. L. *Chem. Commun.* **2001**, 1542–1543.

[54] Connie C. Lu, while a graduate student in the Peters group at Caltech, carried out preliminary studies of iron bis(phosphine)borate complexes.

[55] Das, A. K.; Moatazedi, Z.; Mund, G.; Bennet, A. J.; Batchelor, R. J.; Leznoff, D. B. *Inorg. Chem.* **2007**, *46*, 366–368.

[56] Cowley, R. E.; Holland, P. L. *Inorg. Chem.* **2012**, *51*, 8352–8361.

[57] Fohlmeister, L.; Liu, S.; Schulten, C.; Moubaraki, B.; Stasch, A.; Cashion, J. D.; Murray, K. S.; Gagliardi, L.; Jones, C. *Angew. Chem. Int. Ed.* **2012**, *51*, 8294–8298.

[58] Moatazedi, Z.; Katz, M. J.; Leznoff, D. B. *Dalton Trans.* **2010**, *39*, 9889–9896.

[59] Vicente, J.; Shenoy, R. V.; Martínez-Viviente, E.; Jones, P. G. *Inorg. Chem.* **2011**, *50*, 7189–7194.

[60] Paredes, P.; Díez, J.; Gamasa, M. P. *Organometallics* **2008**, *27*, 2597–2607.

[61] Davis, K. B.; Harris, T. D.; Castellani, M. P.; Golen, J. A.; Rheingold, A. L. *Organometallics* **2007**, *26*, 4843–4845.

[62] Kunrath, F. A.; Casagrande, O. L.; Toupet, L.; Carpentier, J.-F. *Eur. J. Inorg. Chem.* **2004**, *2004*, 4803–4806.

[63] Drouin, S. D.; Foucault, H. M.; Yap, G. P. A.; Fogg, D. E. *Organometallics* **2004**, *23*, 2583–2590.

[64] Devic, T.; Batail, P.; Fourmigué, M.; Avarvari, N. *Inorg. Chem.* **2004**, *43*, 3136–3141.

[65] Szymczak, N. K.; Han, F.; Tyler, D. R. *Dalton Trans.* **2004**, 3941–3942.

[66] Becker, C.; Kieltsch, I.; Broggini, D.; Mezzetti, A. *Inorg. Chem.* **2003**, *42*, 8417–8429.

[67] Barthazy, P.; Togni, A.; Mezzetti, A. *Organometallics* **2001**, *20*, 3472–3477.

[68] Bianchini, C.; Masi, D.; Linn, K.; Mealli, C.; Peruzzini, M.; Zanobini, F. *Inorg. Chem.* **1992**, *31*, 4036–4037.

[69] Kahwa, I. A.; Miller, D.; Mitchel, M.; Fronczek, F. R.; Goodrich, R. G.; Williams, D. J.; O'Mahoney, C. A.; Slawin, A. M. Z.; Ley, S. V.; Groombridge, C. J. *Inorg. Chem.* **1992**, *31*, 3963–3970.

[70] Blake, A. J.; Christie, R. M.; Roberts, Y. V.; Sullivan, M. J.; Schröder, M.; Yellowlees, L. J. *J. Chem. Soc., Chem. Commun.* **1992**, 848–850.

[71] Ezomo, O. J.; Mingos, D. M. P.; Williams, I. D. *J. Chem. Soc., Chem. Commun.* **1987**, 924–925.

[72] Evans, D. J.; Hill, M. S.; Hitchcock, P. B. *Dalton Trans.* **2003**, 570–574.

[73] Masuda, J. D.; Stephan, D. W. *Can. J. Chem.* **2005**, *83*, 477–484.

[74] Sciarone, T. J. J.; Nijhuis, C. A.; Meetsma, A.; Hessen, B. *Dalton Trans.* **2006**, 4896–4904.

[75] Grubba, R.; Ponikiewski, L.; Tomorowicz, L.; Pikies, J. *Acta. Crystallogr. Sect. E.* **2010**, m707–m707.

[76] Rodriguez, M. M.; Bill, E.; Brennessel, W. W.; Holland, P. L. *Science* **2011**, *334*, 780–783.

[77] Zhang, J.; Gao, W.; Lang, X.; Wu, Q.; Zhang, L.; Mu, Y. *Dalton Trans.* **2012**, *41*, 9639–9645.

[78] Olmstead, M. M.; Power, P. P.; Shoner, S. C. *Inorg. Chem.* **1991**, *30*, 2547–2551.

[79] Stokes, S. L.; Davis, W. M.; Odom, A. L.; Cummins, C. C. *Organometallics* **1996**, *15*, 4521–4530.

[80] Eckert, N. A.; Smith, J. M.; Lachicotte, R. J.; Holland, P. L. *Inorg. Chem.* **2004**, *43*, 3306–3321.

[81] Buschhorn, D.; Pink, M.; Fan, H.; Caulton, K. G. *Inorg. Chem.* **2008**, *47*, 5129–5135.

[82] Wang, J.-H.; Chen, C.-H. *Inorg. Chem.* **2010**, *49*, 7644–7646.

[83] Betley, T. A.; Peters, J. C. *J. Am. Chem. Soc.* **2004**, *126*, 6252–6254.

[84] Saouma, C. T.; Lu, C. C.; Peters, J. C. *Inorg. Chem.* **2012**, *51*, 10043–10054.

[85] Sciarone, T. J. J.; Nijhuis, C. A.; Meetsma, A.; Hessen, B. *Organometallics* **2008**, *27*, 2058–2065.

[86] Vela, J.; Cirera, J.; Smith, J. M.; Lachicotte, R. J.; Flaschenriem, C. J.; Alvarez, S.; Holland, P. L. *Inorg. Chem.* **2007**, *46*, 60–71.

[87] Sciarone, T. J. J.; Meetsma, A.; Hessen, B. *Inorg. Chim. Acta* **2006**, *359*, 1815–1825.

[88] Cámpora, J.; Naz, A. M.; Palma, P.; Álvarez, E.; Reyes, M. L. *Organometallics* **2005**, *24*, 4878–4881.

[89] Vela, J.; Smith, J. M.; Lachicotte, R. J.; Holland, P. L. *Chem. Commun.* **2002**, 2886–2887.

[90] Shirasawa, N.; Nguyet, T. T.; Hikichi, S.; Moro-oka, Y.; Akita, M. *Organometallics* **2001**, *20*, 3582–3598.

[91] Kinney, R. A.; Hetterscheid, D. G. H.; Hanna, B. S.; Schrock, R. R.; Hoffman, B. M. *Inorg. Chem.* **2010**, *49*, 704–713.

[92] Lee, Y.; Kinney, R. A.; Hoffman, B. M.; Peters, J. C. *J. Am. Chem. Soc.* **2011**, *133*, 16366–16369.

[93] Thomas, J. C.; Peters, J. C. *J. Am. Chem. Soc.* **2001**, *123*, 5100–5101.

[94] Zechmann, C. A.; Boyle, T. J.; Pedrotty, D. M.; Alam, T. M.; Lang, D. P.; Scott, B. L. *Inorg. Chem.* **2001**, *40*, 2177–2184.

[95] Sur, S. K. *J. Magn. Reson.* **1989**, *82*, 169–173.

[96] Evans, D. F. *J. Chem. Soc.* **1959**, 2003–2005.

[97] Sheldrick, G. M. *Acta Cryst.* **1990**, *A46*, 467–473.

[98] Sheldrick, G. M. SHELXL-97: Program for Crystal Structure Refinement. University of Göttingen, Göttingen, Germany, 1997.

[99] Müller, P. *Crystallogr. Rev.* **2009**, *15*, 57–83.

[100] Dolomanov, O. V.; Bourhis, L. J.; Gildea, R. J.; Howard, J. A. K.; Puschmann, H. *J. Appl. Cryst.* **2009**, *42*, 339–341.

[101] van der Sluis, P.; Spek, A. L. *Acta Cryst.* **1990**, *A46*, 194–201.

[102] Spek, A. L. *Acta Cryst.* **2009**, *D65*, 148–155.